Title
Contact glow discharge electrolysis for liquid waste processing

Permalink
https://escholarship.org/uc/item/2q32r8jt

Author
Sharma, Neeraj

Publication Date
2014

Peer reviewed|Thesis/dissertation

UNIVERSITY OF CALIFORNIA, MERCED

Contact glow discharge electrolysis for liquid waste processing

A Dissertation submitted in partial satisfaction
of the requirements for the degree of

Doctor of Philosophy

in

Mechanical Engineering

by

Neeraj Sharma

Committee in Charge:

      Professor Gerardo Diaz, Advisor

      Professor Yanbao Ma

      Professor Michael F. Modest

2014

The Dissertation of Neeraj Sharma is approved, and it is acceptable
in quality and form for publication on microfilm and electronically:

Professor Yanbao Ma

Professor Michael F. Modest

Professor Gerardo Diaz, Advisor

University of California, Merced

2014

Contents

Nomenclature

A	aspect ratio
C_p	specific heat (J kg^{-1} K^{-1})
D	diffusion coefficient (m^2 s^{-1})
E_0	externally applied electric field (V m^{-1})
EDL	electric double layer
e	elementary charge (1.602 $\times$ 10^{-19}C)
Fr	Froude number
H	height of cylinder (m)
h	specific enthalpy (J kg^{-1})
h_{fg}	latent heat of vaporization (J kg^{-1})
$\underline{\underline{I}}$	unit tensor
$\overline{J}$	current density (A m^{-2})
j	normalized current density
k	thermal conductivity (W m^{-1} K^{-1})
k_b	Boltzmann constant (1.38 $\times$ 10^{-23}J K^{-1})
l	length of heating element (m)
M	molar mass (kg mol^{-1})
m	mass fraction
n	local number concentration (m^{-3})
n_0	bulk number concentration of ions in electrolyte solution (m^{-3})
Nu	Nusselt number
Pr	Prandtl number
p	pressure (Pa)
Pe	Péclet number
$\dot{q}$	volumetric heat generation (W m^{-3})
R	annulus gap width
Ra	Rayleigh number
r	radius (m)
Re	Reynolds number
S	volumetric particle generation rate (m^{-3} s^{-1})
Sc	Schmidt number
T	temperature (K)
t	time (s)
u	velocity in x-direction (m s^{-1})
v	velocity in y-direction (m s^{-1})
V	electric potential (V)
z	charge valence of ions
z_e, z_w	z coordinates

| A_r, B, F, G | non-dimensional parameters |
| K, Q_r, R, U | |

Greek Symbols

α	dimensionless applied electric field
α_r	reference thermal diffusivity ($\mathrm{m^2\ s^{-1}}$)
α_T	Townsend coefficient ($\mathrm{m^{-1}}$)
β	dimensionless number concentration
β_r	Thermal expansion coefficient ($\mathrm{K^{-1}}$)
Γ	particle flux ($\mathrm{m^{-2}\ s^{-1}}$)
ϵ	dielectric constant of the electrolyte
ϵ_0	permittivity of vacuum (8.85×10^{-12} C $\mathrm{V^{-1}\ m^{-1}}$)
η	molar concentration of ions in electrolyte ($\mathrm{mol\ m^{-3}}$)
θ	non-dimensional temperature
λ	electrical conductivity of the electrolyte solution ($\mathrm{\Omega^{-1}\ m^{-1}}$)
$\lambda^{\pm}$	equivalent ionic conductivity ($\mathrm{m^2\ \Omega^{-1}\ mol^{-1}}$)
μ	dynamic viscosity (Pa s)
ν	kinematic viscosity ($\mathrm{m^2\ s^{-1}}$)
ρ	density ($\mathrm{kg\ m^{-3}}$)
ρ_e	local net electrical charge density ($\mathrm{C\ m^{-3}}$)
$\underline{\underline{\tau}}$	stress tensor
ϕ	electric potential due to externally applied electric field (V)
φ	scalar field used in projection methods
ψ	electric potential due to electric double layer (V)
ω	vapor mass flux ($\mathrm{kg\ m^{-2}\ s^{-1}}$)
$\vec{\omega}$	vorticity ($\mathrm{s^{-1}}$)

Subscripts

a	air
e	heating element surface
$\underline{e}$	electron
f	fluid (liquid or air)
i	interface
$\underline{i}$	ion
in	inlet
l	liquid
0	ambient
r	reference
v	vapor

w	wall
x	component in X-direction
$\perp$	normal component of a vector
$\parallel$	tangential component of a vector

Superscripts

$+$	cations
$-$	anions

List of Figures

List of Tables

Glossary

Anode: The anode is the electrode at which electrons leave the cell and oxidation occurs.

Cathode: The cathode is the electrode at which electrons enter the cell and reduction occurs.

Cathode fall region: The region near cathode across which most of the potential drop happens.

Contact glow discharge electrolysis (CGDE): When the conditions of glow-discharge electrolysis are established with both electrodes being in contact with the electrolyte, the process is called contact glow-discharge electrolysis.

Electrode: An electrode is an electrical conductor used to make contact with a nonmetallic part of a circuit. An electrode in an electrochemical cell is referred to as either an anode or a cathode.

Electric Double Layer (EDL): A model of the interface between an electrode and the solution close to it. In this model a sheet of one type of electrical charge surrounds the surface of the electrode and a sheet of the opposite charge surrounds the first sheet in the solution.

Electrochemical cell: An electrochemical cell is a device capable of either generating electrical energy from chemical reactions or facilitating chemical reactions through the introduction of electrical energy.

Electrolytic cell: An electrolytic cell is an electrochemical cell that undergoes a redox reaction when electrical energy is applied. An electrolytic cell has three parts, an electrolyte and two electrodes (a cathode and an anode). The electrolyte is usually a solution of water or other solvents in which ions are dissolved.

Glow-discharge (GD): An electrical discharge that passes through a gas at low pressure and causes the gas to become luminous. The glow is produced by the decay of excited atoms and molecules.

Glow-discharge electrolysis (GDE): If an electric discharge is passed to a conducting solution (electrolyte) from an electrode placed in the gas space above the solution surface, chemical reactions can be brought about in

the liquid phase and the process is referred to as glow-discahrge electrolysis (GDE). The fundamental difference between glow-discharge electrolysis and glow-discharge is that the solution itself is one of the electrodes and the reactions of interest are those which occur within the liquid phase. Research has shown that the charge transfer is only a minor factor in GDE, and the chemical effects are produced by charged particles which are accelerated in the potential fall near the electrolyte surface and enter the liquid with relatively high energies and can dissociate or excite solvent molecules by collisions, in addition to entering into charge-transfer reactions, and the chemical effects are analogous to those produced by ionizing radiations [7].

Ion: An atom or group of atoms that has either lost one or more electrons, making it positively charged (a cation), or gained one or more electrons, making it negatively charged (an anion).

Normal electrolysis: The production of a chemical reaction by passing an electric current through an electrolyte is termed as normal electrolysis or just electrolysis. In electrolysis, positive ions migrate to the cathode and negative ions to the anode. The reactions occurring depend on electron transfer at the electrodes and are therefore redox reactions. At the anode, negative ions in solution may lose electrons to form neutral species. Alternatively, atoms of the electrode can lose electrons and go into solution as positive ions. In either case the reaction is an oxidation. At the cathode, positive ions in solution can gain electrons to form neutral species. Thus cathode reactions are reductions.

Polar solvents: Polar solvents are compounds such as water and liquid ammonia, which have dipole moments and consequently high dielectric constants. These solvents are capable of dissolving ionic compounds or covalent compounds that ionize.

Plasma: A collection of charged particles containing about equal numbers of positive ions and electrons and exhibiting some properties of a gas but differing from a gas in being a good conductor of electricity and in being affected by an electromagnetic field.

Radicals: An atom or group of atoms with an unpaired valence electron. Free radicals can be produced by photolysis or pyrolysis in which a bond is broken without forming ions. Because of their unpaired valence electron, most free radicals are extremely reactive.

Reverse-osmosis: A method of obtaining pure water from water containing a salt, as in desalination. Pure water and the salt water are separated by a semipermeable membrane and the pressure of the salt water is raised above the osmotic pressure, causing water from the brine to pass through the membrane into the pure water. This process requires a pressure of some 25 atmospheres, which makes it difficult to apply on a large scale.

Redox (reduction-oxidation): Originally, oxidation was simply regarded as a chemical reaction with oxygen. The reverse process (loss of oxygen) was called reduction. Reaction with hydrogen also came to be regarded as reduction. Later, a more general idea of oxidation and reduction was developed in which oxidation was loss of electrons and reduction was gain of electrons. This wider definition covered the original one.

Acknowledgments

Curriculum Vitæ
Neeraj Sharma

Education

2014	PhD. in Mechanical Engineering, University of California, Merced. Title: Contact glow discharge electrolysis for liquid waste processing. Supervisor: Prof. Gerardo Diaz.
2008	Masters in Aeronautics and Space Technology, Technical University Munich, Germany and Technical University Madrid, Spain.
2005	B. Tech in Mechanical Engineering, Indian Institute of Technology Delhi, India.

Abstract

Contact glow discharge electrolysis for liquid waste processing

Neeraj Sharma

Ph.D. in Mechanical Engineering

Professor Gerardo Diaz, Advisor

University of California, Merced

2014

With the growing scarcity of water resources and increasing demand in energy, research efforts in effective water treatment and liquid waste management have been expanding steadily. The ability of UV light present in various electric discharges to disinfect water makes the use of plasma based technologies an effective alternative to the traditional methods like reverse-osmosis, distillation, etc. The interaction of plasmas with liquids has been a subject of current research and the present thesis includes both experimental and theoretical work done to better understand the physics of contact glow discharge electrolysis applied to waste water treatment.

Other aspects of the interaction between electric fields and electrolytes have also been analyzed in this work. For instance, electric double layer theory has been used to model the interaction between electric field and liquid waste close to the solid surface incorporating joule heating and evaporation. The presence of the electric field results in a coupling of the momentum, energy, and mass transfer equations which are solved simultaneously with the Poisson-Boltzmann equation that describes the electric potential distribution. The results show that the rate of evaporation at the air-liquid interface is a strong function of the applied electric field and bulk ion-concentration.

Temperature patterns observed in electrolytic cell experiments has been explained using buoyancy-driven flow model. As the heating element does not extend along the entire axial length of the cylindrical tank, this configuration displays very particular vortex patterns inside the cell and divides the domain into two regions of different temperatures.

To model electrohydrodynamics accurately, boundary conditions for Navier-Stokes equations are revisited and a new formulation has been proposed to numerically solve the Navier-Stokes equations. The proposed formulation is particularly

suitable for transient problems including start-up problems. In addition, a novel projection scheme has been proposed which is coupled with Navier-Stokes algorithm to produce numerical solutions on non-staggered grids, which is 2nd order accurate in both space and time. The proposed projection scheme is also suitable for generating compatible initial data from given initial data at the start of any numerical simulation. The methodology developed can be adapted to study the dynamics of plasma based on a two-fluid formulation.

Chapter 1

Introduction

1.1 Background

Scarcity of water resources and increasing global demand for clean energy has provided the need for research and development in the area of sustainable and renewable energy application to waste water management. Use of electric discharges in water treatment is not new but the physics behind the interaction of electric discharges with liquid waste has not been fully understood. The present dissertation has made a contribution in the following areas:

1. Experimental study of contact glow discharge electrolysis under new operational range of voltage and current.

2. Experimental study of CGDE in the presence of liquid waste and biomass along with the study of the role of nonconducting medium (pebbles) in preventing the direct arcing under higher current conditions.

3. Experimental study of the application of CGDE in steam production from liquid waste.

4. Modeling the interaction between electric fields and fluid near the surface of nonconducting medium using the theory of electric double layer.

5. Modeling the buoyancy driven flow in the presence of an electrode using the weakly compressible flow equations and without making the Boussinesq approximation which is not valid under the conditions of higher driving temperature difference. This analysis can be coupled with the analysis done using electric double layer theory to simulate the interaction of electric field and fluid at the fluid-air interface.

6. Contact glow discharge present near the cathode is modeled using the DC plasma equations which can be extended to include the contributions from other plasma reactions and coupling it with the analysis done in the fluid for a complete modeling of CGDE.

7. A new fully explicit finite-difference scheme for solving transient Navier-Stokes equations on a nonstaggered grid has been proposed. To verify the accuracy of the scheme, it has been implemented using Sparse matrix structure in Matlab for a well known benchmark problem of driven cavity and the results are compared with the known benchmark results from the literature. So far similar schemes are known to give checkerboard oscillations. As modeling the fluid part is integral to modeling the plasma-fluid interactions which are inherently of transient nature, the new scheme can be applied to track the transient behavior more accurately.

The following subsections give a brief overview of the existing state of the art in the related areas.

1.1.1 Contact glow discharge electrolysis

Retracing the early history of electrochemical discharges, Wüthrich and Mandin [8] attributed the first description of electrochemical discharges to the work of French physicists Hippolyte Fizeau and Léon Foucault [9] published in 1844. The authors in [8] also mentioned the work of Jules Violle and Michel Chassagny [10] published in 1889 which described how normal electrolysis established in a cell with two platinum electrodes dipped in sulphuric acid gave rise to a new effect above a certain voltage in which the thinner electrode became surrounded by a gas film with electrochemical discharges taking place inside the film. In particular, the field of electrochemical discharges in aqueous solutions has been studied and expanded considerably since Kellogg [11] first reported similarities between anode effect in molten electrolysis and electrochemical discharges in aqueous solutions at high current density. Kellog concluded that when the electrode temperature reached the boiling point of the electrolyte, normal operation of the anode was found to cease and the cell entered a "transition period," which instantaneously changed to "aqueous anode-effect" when the voltage was raised beyond a critical value. Hickling and Newns [12] studied similar discharges in liquid-ammonia solution and noted the similarity of the chemical effects to those produced in glow discharge electrolysis generated by passing a discharge to the surface of the solution at reduced pressure [13–16]. They noted that, at low voltages, conventional electrolysis was established in the electrolytic cell but upon increasing the volt-

age beyond a threshold, conventional electrolysis broke down resulting in a sudden increase in voltage across the electrodes and a reduction in current through the cell with the anode surrounded by a greenish discharge. They named the process "contact glow discharge electrolysis" to differentiate it from the process in which one electrode is not directly in contact with the electrolyte. Hickling and Ingram [7] further studied contact glow discharge electrolysis to find out its characteristic features, chemical effects and the reason for the breakdown of conventional electrolysis. They concluded that such a breakdown can be expected whenever current density near the electrode with smaller area was high enough for joule heating to cause local vaporization of the solvent. More recently, Sengupta et al. [17] studied contact glow-discharge electrolysis and identified solvent vaporization near an electrode and the onset of hydrodynamic instabilities in solvent vaporization at the electrode as two prime factors for transition of normal electrolysis to CGDE. Gangal et al. [18] examined the applicability of Helmholtz-Taylor's boiling heat transfer theory to the breakdown of normal electrolysis and the transition to CGDE. They found that anolyte surface tension, the anode wire dimension, and the anode material affect the critical voltage necessary for the breakdown of normal electrolysis.

Since then contact glow discharge electrolysis has been used in various applications. Harada et al. [19] used it in synthesis of uracil and thymine. Under the name of "plasma electrolysis" it finds numerous applications in surface engineering, an extensive review of which has been presented by Yerokhin et al. [20]. Wüthrich et al. [21] studied physical principle and miniaturization of spark assisted chemical engraving. They observed that by adding surfactants to the electrolyte, the critical voltage reduces significantly. Gao et al. [22] studied the oxidative degradation of acridine orange under different mediums, pHs, and voltages using CGDE. More recently, plasma electrolysis has been used to generate hydrogen which has attracted a lot of attention [23–27] due to the importance of hydrogen as a fuel and the interest in reducing carbon emissions. Hu et al. [28] conducted a study on water treatment induced by plasma with CGDE and reported oxidative degradation of eight kinds of dyes in aqueous solution. Mandin et al. [29] presented the electrochemical engineering modeling of two-phase electrolysis properties at electrode vicinity.

Most of the research in CGDE has been carried out under relatively low values of current (1 A). The present research explores the CGDE under higher values of current (10-40 A). As a result of higher current densities present in the system, the chances of direct arching between the electrodes increase. To prevent the formation of arc between electrodes which may result in material failure, nonconducting material (pebbles) has been introduced between the electrodes which results in the

formation of the electric double layer around the surfaces of the nonconducting pebbles. In the present dissertation the effect of the electric double layer as well as the current and voltage characteristics at new operating conditions have been studied.

1.1.2   Liquid film evaporation in the presence of an electric field

In the present dissertation various aspects of contact glow discharge electrolysis are studied with the aim to better understand the interaction of electric discharges and liquid waste. A mathematical model is developed to understand the evaporation of liquid films in the presence of electric fields. Liquid-film evaporation and condensation have been extensively studied in the past due to the interesting transport phenomena involved and the many applications of these processes in a variety of areas that include renewable energy, chemical distillation, air conditioning, cooling towers, drying, desalination, liquid film evaporation, heat and mass exchangers, and desiccant systems, among others.

Mathematically, the process of falling film evaporation is similar to that of falling film condensation [30]. The heat transfer mechanism in liquid films occurs due to conduction and convection inside the film where phase change takes place at the air-liquid interface [31]. Chun and Seban [32] studied the process of heat transfer in evaporating liquid film on a heated vertical tube under nonnucleating conditions. Their purpose was to estimate the heat transfer coefficient. No temperature distribution inside the liquid film was presented in their study. The process of heat transfer to a liquid film draining off a vertical plate was studied numerically by Isenberg and Gutfinger [33]. The temperature distribution inside the liquid film was obtained under the assumption of creeping flow. The temperature distribution in the gas side was not calculated. The lack of experimental data prompted Chandra and Savery [34] to study heat and mass transfer over a vertical falling film under forced convection. The nonhomogeneous boundary conditions were specified by using measured temperature and concentration distributions along the gas-liquid interface. The problem of evaporation and heating with turbulent falling liquid films was studied by Seban and Faghri [35]. An appropriate turbulence model was examined and more experimental results were obtained with essentially the same apparatus used by Chun and Seban [32]. The evaporation of water into a laminar stream of dry air, humid air, and superheated steam was studied numerically by Chow and Chung [36]. The focus of their study was to investigate the physical reasons for the existence of the inversion temperature and to discuss the suitability of the one-third-rule for defining the reference

temperature and mass concentration. Their paper presented the mathematical formulation of the heat and mass transfer on the air side and at the liquid-air interface. Schröppel and Thiele [37] studied heat and mass transfer in laminar and turbulent boundary layer flows of gas over a vaporizing liquid film. The liquid film was considered stationary with a constant thickness. The heat and mass transfer effects on the liquid film were not presented. Yan et al. [38] experimentally studied the evaporative cooling of liquid film through interfacial heat and mass transfer in a vertical channel. The theoretical model for the same process was discussed in a separate paper by Yan and Lin [39]. The model was simplified by neglecting inertia in the momentum equation and the normal convection term in the heat equation for the liquid film flow. Making similar assumptions, Yan and Soong [40] numerically studied the convective heat and mass transfer along an inclined heated plate with film evaporation. Mezaache and Daguenet [41] studied film evaporation along an inclined plate for various inlet conditions using a two-dimensional boundary-layer model. Jabrallah et al. [42] studied convective heat and mass transfer involved in the evaporation of a falling liquid film in closed rectangular cavity with constant wall heat flux.

The effect of the application of an electric field to a fluid containing free ions, i.e. an electrolyte, has been studied by several authors. Rice and Whitehead [43] analyzed theoretically the effect of electrokinetic radius on the electrokinetic flow in a narrow cylindrical capillary tube under the Debye-Hückel condition. In order to see whether the theory could be reasonably extended to the higher values of surface potential, they proposed to obtain a numerical solution of the Poisson-Boltzmann equation for a cylindrical capillary and compare it with the approximate solution. Levine et al. [44] extended the theory developed in [43] to higher zeta-potential, that corresponds to the potential at the shear surface between the charged surface and the electrolyte solution [30]. They developed an analytical approximation to the solution of the Poisson-Boltzmann equation within a capillary tube. It is known that some materials immersed in an electrolyte solution develop a surface charge. Helmholtz proposed in the nineteenth century that this surface charge is balanced by a layer of oppositely charged ions that is known as the electric double layer (*EDL*). The effect of the electric double layer near the solid-liquid interface and the flow induced electrokinetic field on the pressure-driven flow through a rectangular microchannel were analyzed by Yang et al. [45]. Both the velocity and the temperature fields for various conditions were determined for steady-state fully-developed laminar flows. It was shown that for aqueous solutions of low ionic concentration and a solid surface of high zeta potential, the liquid flow and heat transfer in rectangular microchannels are significantly influenced by the presence of the electric double layer. The characteristics of electroosmotic flow

(EOF) in rectangular microchannels were investigated numerically by Arulanandam and Li [46]. The results demonstrated the significance of geometry effects, ionic concentration, and zeta potential on EOF. The energy equation was not included but it was indicated that for the conditions analyzed, the thermal effects were negligible. Hsu et al. [47] studied the electrokinetic flow through an elliptical microchannel under the basis of three boundary conditions: constant surface potential, constant surface charge density, and charge regulated surface. Jamaati et al. [48] considered the effect of slip at the walls for pressure-driven electrokinetic flows in planar microchannels. Their study indicated that liquid slip at the walls could increase the induced voltage significantly. A mathematical model was developed to study the electrokinetic effects on pressure-driven liquid flow in a parallel slit by Chen et al. [49]. The model included the general Nernst-Planck equation to describe anion and cation distribution, the Poisson equation to determine the electrical potential profile, and the modified Navier-Stokes equation to determine the velocity flow field. The results showed that the presence of the EDL in the developing flow decreases the fluid velocities. It was also shown that in the developing regime the electrical potential and the electrical net charge density predicted by using the Nernst-Planck equation and the Boltzmann distributions were very different.

In the literature related to liquid-film evaporation, heat transfer to the fluid is generally specified at the boundary, in terms of either wall temperature or heat flux, or as a volumetric heat generation term. In the present work, the heat source results from an externally applied electric field which also has an effect on the fluid velocity distribution. The effect of the application of an electric field on the rate of evaporation and temperature distribution in an electrolyte film in contact with moist air is the focus of mathematical model presented.

The inclusion of nonconducting medium in the system analyzed in the present dissertation prompted the study of electric double layer in the context of CGDE.

1.1.3 Buoyancy driven flows with partially immersed electrode

The literature related to the mathematical modeling of buoyancy driven flow in the presence of partially immersed electrode acting as a heating element was also surveyed. This phenomenon occurs in electrolytic cells used to process liquid waste.

Natural convection heat transfer and fluid flows have been studied in various configurations by many researchers with applications ranging from passive cooling of electronics to heat transfer in nuclear fuel rods. Bazylak et al. [50] studied nat-

ural convection in an enclosure with distributed heat sources. Their heat sources were located at the bottom wall and they found that spacing equal to that of source length provided the most effective heat transfer. Convective heat transfer from four in-line simulated electronic chips in a vertical rectangular channel using water as the working fluid was studied experimentally in [51]. They analyzed the effect of heat fluxes, flow rates and geometrical parameters such as chip number and developed empirical correlations using Nusselt, Reynolds and Grashof numbers, based on channel hydraulic diameter. Chadwick et al. [52] studied both experimentally and theoretically the natural convection from two-dimensional discrete heat sources in a rectangular enclosure and found that the location of heat source near the bottom of the enclosure maximizes the heat transfer in high Grashof number range. Buoyancy convection in the presence of mutually orthogonal heat generating baffles has been studied in [53] in a square cavity with walls subjected to an isothermal temperature or outward heat flux. The problem was formulated and solved in terms of vorticity-stream function for various configurations of the baffles. Keyhani et al. [54] performed an experimental study of natural convection with discrete heat sources in an ethyl-glycol filled vertical cavity. With the help of heat transfer data and flow visualization, they found that stratification was the primary factor influencing the temperature of heated sections. Effective boundary conditions at the open side of two and three dimensional open-ended structures was studied in [55, 56]. Convective heat transfer in vertical or inclined annular enclosures with either constant heat flux at the inner wall or constant temperature at inner wall have been studied both experimentally and theoretically by various authors [57–63]. Reddy and Narasimham [64] performed a numerical study of conjugate natural convection in a vertical annulus with centrally located vertical heat generating rod as the driving source using pressure-correction algorithm with the problem formulated in primitive form. Their study has applications in spent nuclear casks and electrical and electronics equipment where temperature distribution in the central vertical rod is of interest.

More recently, the numerical study of natural convection in a vertical annulus with localized heat source was done in [65]. Their study focused on the effect of size and location of a single isoflux heat source on the buoyancy induced convection in a cylindrical annulus. They found that the rate of heat transfer is an increasing function of radii ratio of the annulus. They also determined that the placement of the heater near the center of the cylinder avoided hot spots and yielded maximum heat transfer.

Most of the studies found in literature related to convection in vertical annulus with either discrete or continuous heating source or constant wall temperature employ the Boussinesq approximation which limits the driving temperature dif-

ferences to relatively low values. A recent notable exception to this approach being [66], in which the authors have studied non-Boussinesq conjugate natural convection in a vertical annulus with axial heat generating rod which extends along the entire length of the outer cylinder.

The present study is aimed at formulating the steady-state natural convection in a partial annulus in the general framework of weakly compressible flow without applying Boussinesq approximation. The Rayleigh number still limits the applicability of a laminar flow model. The configuration studied in the present dissertation has the inner cylindrical heating element extended only partially into the outer cylinder. This configuration finds applications in heating of fluids using partially immersed heating elements. Convection in a electrolytic cell with a partially immersed electrode can also be represented by the present configuration with the additional electro-chemical processes affecting the heat transfer and fluid flow.

1.2   Motivation and outline of dissertation

This dissertation presents experimental and theoretical research based on experiments of contact glow discharge electrolysis of liquid waste conducted at the Sustainable Plasma Gasification Lab at UC Merced.

The experimental setup consisted of an electrolytic cell used for the generation of steam from liquid waste. Another set of experiments was conducted in a smaller scale electrolytic cell to study other aspects such as the contact glow discharge electrolysis in the presence of biomass.

The experimental research included in this dissertation pertains to understanding of plasma-liquid interaction and the process of generation of steam from liquid waste using contact glow discharge electrolysis in an electrolytic cell. To better understand the underlying physics, a mathematical model of evaporating liquid film in the presence of applied electric field was developed. A temperature stratification was observed in the electrolytic cell which motivated the development of mathematical model of buoyancy driven flow in the presence of partially immersed heating element to explain such temperature distribution without making Boussinesq assumption.

Further, glow discharge present near the cathode was modeled using plasma equations. As water vapor is the most abundant species present in the glow discharge region in experiments carried out in the present dissertation, the methodology was applied to run a simulation with water vapor filling the region between the electrodes. Results are shown to be extremely sensitive to the electric field boundary conditions.

With the aim to better understand the interaction (confined to a very thin layer near solid boundaries and free surfaces) between electric field and charges present in the liquid waste in the form of ions and include them as a part of boundary conditions, we revisited Navier-Stokes equations and the accompanying boundary conditions. A survey of pertinent literature made us aware of the issues related to the boundary conditions of Navier-Stokes equation. A need to delve deeper into the modeling aspect of Navier-Stokes equations and corresponding boundary conditions became apparent. As a result, a new formulation is presented to solve transient Navier-Stokes equations on nonstaggered grids. A computer code has been developed using the sparse matrix structure in Matlab for implementing the new formulation and the results are compared against the well established benchmark problem of driven cavity.

Chapter 2

Experimental: CGDE applied to liquid waste

This chapter includes various experiments performed to better understand the interaction between contact glow discharge electrolysis and liquid waste. First the experimental setup is described in detail followed by experimental procedure. Various current and voltage characteristics along with relevant explanation are described in results and discussion. Finally we describe another set of focused experiments carried out to quantify the amount of steam generated and the efficiency of CGDE in generating steam. Work presented in this chapter has been published [67–69].

2.1 Experimental Setup

Experiments were performed at the Sustainable Plasma Gasification Lab at UC Merced. The equipment used corresponded to the patented HiTemper™ electrolytic cell from Foret Plasma labs [1]. A preliminary set of tests aiming to measure electrolyte temperature distribution were conducted in an electrolytic cell with an anode composed of a stainless steel container of 270 mm in diameter and 260 mm in height, as shown in Fig. 2.1. The cathode is a graphite electrode with a diameter of 8 mm that is positioned along the central axis of the container. The effect of electrolyte concentration is analyzed by testing $NaHCO_3$ solutions with concentrations of 1% and 2% by weight in distilled water, and NaCl solutions with a concentration of 1%.

Power was provided by an ESP-150 power supply manufactured by ESAB with a control console developed by Foret Plasma Labs [1]. The unit has a current range between 0 and 150 Amperes and a maximum voltage of 380 Volts. A potentiometer
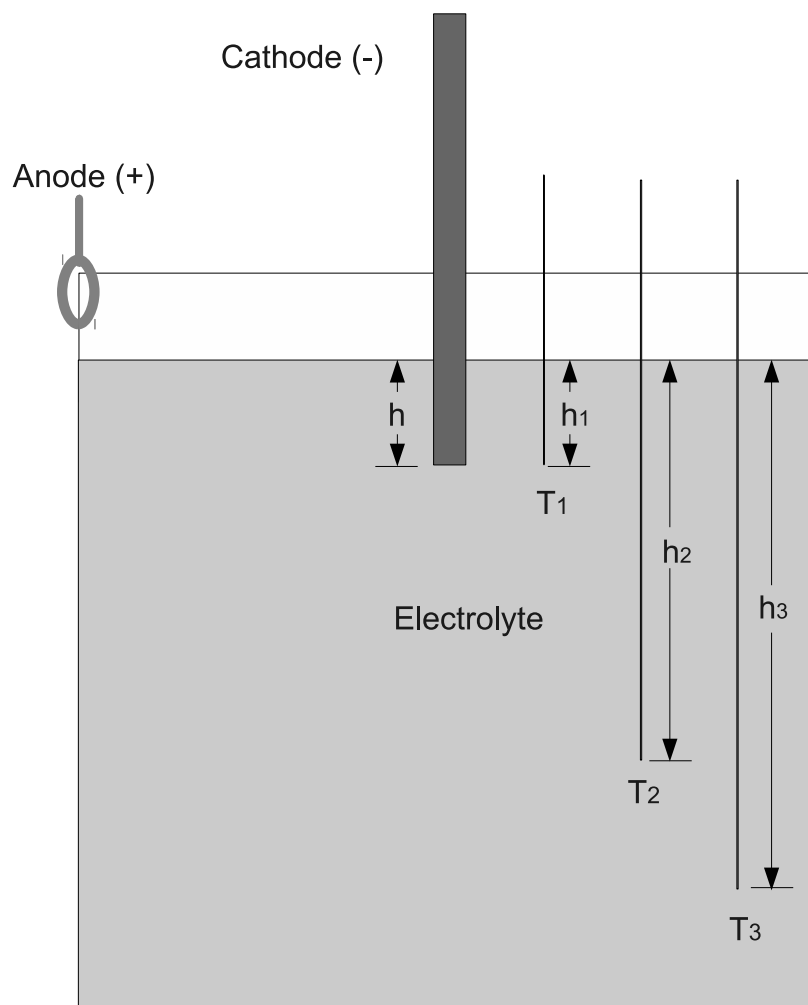
Figure 2.1: Stainless steel electrolytic cell utilized for the first set of experiments. T_1, T_2, and T_3 correspond to temperature measurements taken at depths of h_1, h_2, and h_3, respectively.

knob on the power supply panel is used to set the current level during tests. Three thermistors equally spaced along the radius of the container were placed at various depths from the surface of the electrolyte to measure the temperature variation with respect to depth and radial distance. The temperature scale of the thermistors covers a range between -40°C and 230°C with a resolution of 0.1°C. Figure 2.1 shows the location of the thermistors where $h_1 = 20$ mm, $h_2 = 100$ mm, and $h_3 = 150$ mm. The cathode was submerged at a depth $h = h_1$. Table 2.1 gives the values of various parameters used in the experiment. A National Instruments™ data acquisition system was used along with NI LabVIEW™ to record current, voltage, and temperatures with measurements taken every two seconds. Current values were measured with a Veris direct current sensor model H970HCA with a maximum current range of 200 A and $\pm 3\%$ of accuracy at full scale. Voltages were read directly from a remote control connecting pin on the power supply.

Table 2.1: Values of various dimensions and parameters in experimental setup.

Parameter	Unit	Values
Diameter of electrolytic cell	mm	270
Height of electrolytic cell	mm	260
Height of electrolyte surface	mm	140
Depth of cathode submerged in electrolyte	mm	20
Concentration of $NaHCO_3$ electrolyte	% by weight	1 and 2
Concentration of NaCl electrolyte	% by weight	1

2.2 Experimental Procedure

The electrolytic cell was filled with electrolyte solution until the electrode was submerged to a depth $h = 20$ mm, as seen in Fig. 2.1. The potentiometer knob at the power supply panel was set to a low position that remained fixed throughout the experiment. Higher potentiometer settings in this configuration resulted in high power densities at the cathode surface generating excessive water splash and free-surface motion producing a variable wetting of the cathode and thermistors during tests. Therefore, power was kept at moderate levels to ensure uniform wetting of electrode and thermistors. The potentiometer limits the amount of current flowing between the electrodes but the power supply allows variation of voltages and currents depending on the physical parameters affecting the process. At the start of each experiment the electrolyte solution, $NaHCO_3$ or NaCl in distilled

water, was near room temperature and the cell operated in conventional electrolysis mode, also called, normal or conventional electrolysis. The temperature of the electrolyte solution increased due to Joule heating resulting in a higher rate of evaporation that lowered the liquid level in the cell, thereby, decreasing the submerged length of the cathode and further increasing electric current density near the cathode. At a critical value of current density and when the solution temperature near the cathode approached its boiling point, the operating mode in the cell transitioned from normal electrolysis to contact glow discharge mode generating a visible glow and enhancing the volumetric heat generation rate near the cathode, substantially increasing steam production.

2.3 Electrochemical Reactions

Once flow of current is established due to the presence of an electric field, the overall reaction for the electrochemical process in a solution of $NaHCO_3$ in water becomes [70, 71]:

$$4\,NaHCO_3 + 2\,H_2O \longrightarrow 2\,H_2 + O_2 + 4\,CO_2 + 4\,NaOH \qquad (2.1)$$
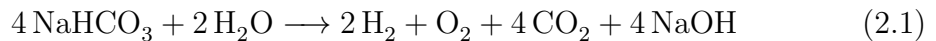
Some of the most common reactions between electrons and neutral water molecules in plasma are listed in Table 2.2.

Table 2.2: Reactions between electrons and neutral water molecules in plasma [4].

Type of reaction	Reaction	Threshold (eV)
Ionization	$H_2O + e \longrightarrow H_2O^+ + 2\,e$	13.0
Ionization	$H_2O + e \longrightarrow OH^+ + H + 2\,e$	15.0
Ionization	$H_2O + e \longrightarrow O^+ + H_2 + 2\,e$	22.5
Ionization	$H_2O + e \longrightarrow O + H_2^+ + 2\,e$	29.0
Ionization	$H_2O + e \longrightarrow OH + H^+ + 2\,e$	19.0

When an electric field is applied to a solution of NaCl in water, current flow is established and the following reactions occur at the anode: $Cl^-(aq) \longrightarrow Cl + e^-$ and $Cl + Cl \longrightarrow Cl_2(g)$, which releases chlorine gas. The reactions at the cathode are $H^+(aq) + e^- \longrightarrow H$ and $H + H \longrightarrow H_2(g)$.

Also, the formation of other species such as H_2O_2 and hydroxyl radicals is well documented in the literature but was not the subject of study in this work.

2.4 Results and Discussion

With the electrolyte solution near room temperature, the electrolytic cell operates in normal electrolysis mode. The potentiometer on the power supply panel was set to 1/8 of its full scale and remained fixed during the entire duration of the test. As the experiment progresses, the temperature of the electrolyte increases as a result of Joule heating. Values of electrical conductivities of different electrolyte solutions before and after the test were measured using Thermo Scientific portable multiparameter meter. These values are given in Table 2.3.

Table 2.3: Values of electrical conductivities of different electrolyte solutions before and after the test.

Electrolyte	Concentration	Initial electrical conductivity[a] $(k\Omega^{-1}cm^{-1})$	Final electrical conductivity[a] $(k\Omega^{-1}cm^{-1})$
NaCl	1 %	17.66	19.56
$NaHCO_3$	1 %	8.53	9.72
$NaHCO_3$	2 %	15.66	17.3

[a] @ 25°C approx.

The electrical conductivity of the electrolyte increases with temperature and it causes the current passing between the electrodes to augment during the first minutes of the test. Figure 2.2 shows the variation of the current with respect to time for $NaHCO_3$ solutions of 1% (solid line) and 2% (dashed line), and a NaCl solution of 1% (dash-dotted line) on a mass basis. Increasing the salt concentration in the electrolyte solution has the expected effect of incrementing the flow of current due to the higher electrical conductivity. For a particular concentration of a salt, transition from normal electrolysis to contact glow discharge electrolysis is marked by sudden drop in current which results in abrupt change in the slope of the plots. Once the process transitions to contact glow discharge electrolysis, the transient and oscillatory nature of the vapor film results in current fluctuations appearing in the plot. The results for NaCl display the same trend as $NaHCO_3$ but current values are larger due to the higher electrical conductivity of NaCl compared to $NaHCO_3$. Figure 2.3 shows the variation of voltage with respect to time for the same three cases where, at the beginning of the test, voltages decrease smoothly to a stable value. The decrease in voltage is due to the nature of power supply which tries to maintain the total power supplied within a certain range.
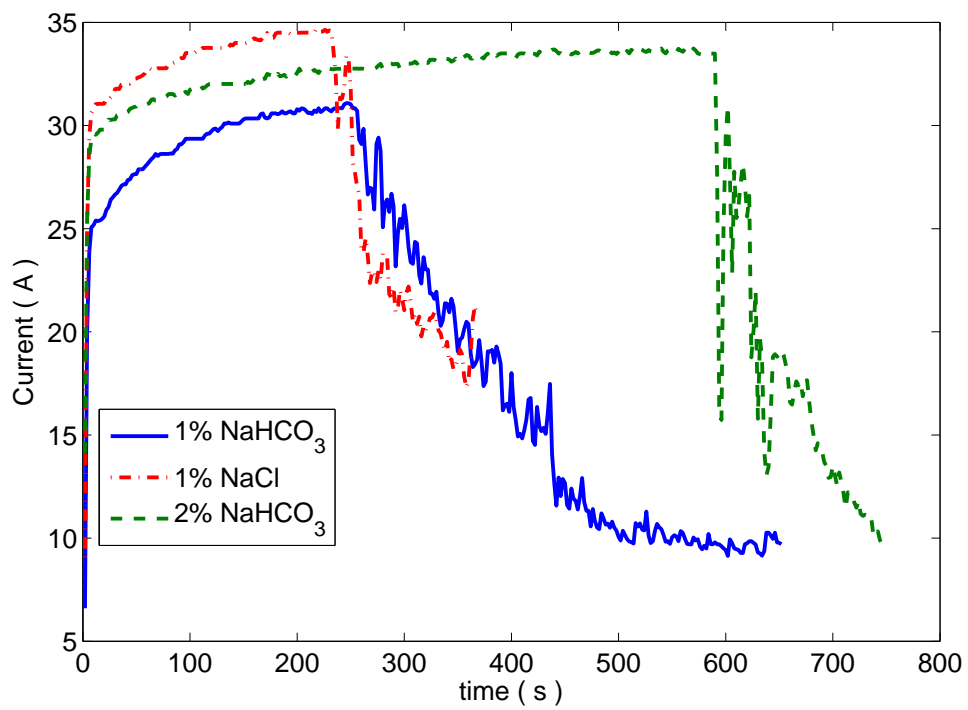
Figure 2.2: Variation of current with time for $NaHCO_3$ concentrations of 1% and 2%, and NaCl concentration of 1% in distilled water.
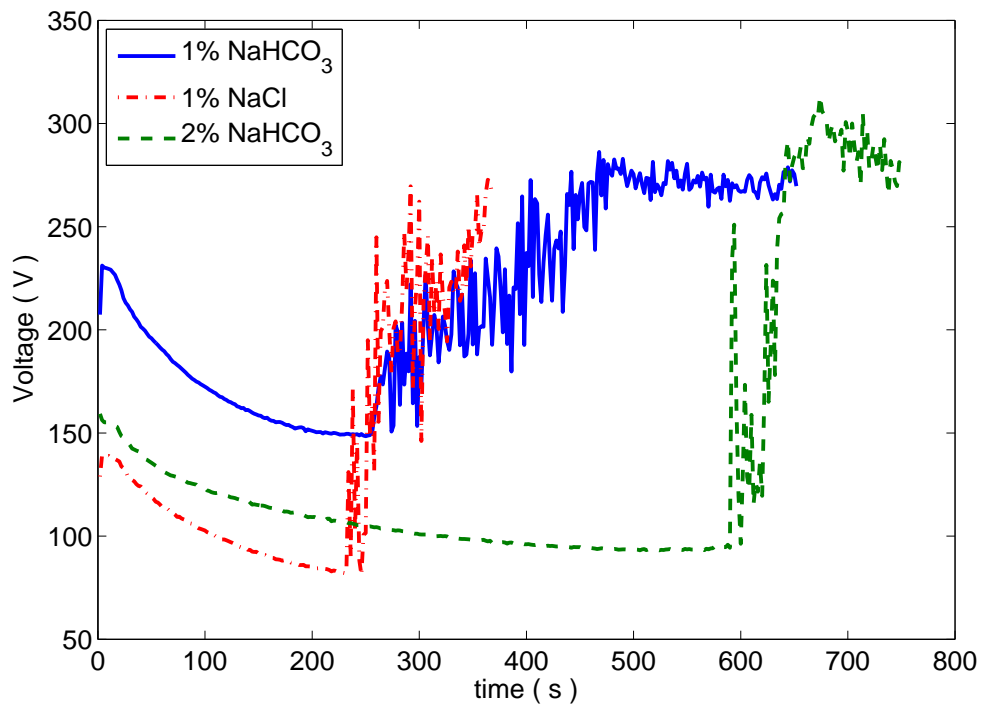
Figure 2.3: Variation of voltage with time for $NaHCO_3$ concentrations of 1% and 2%, and NaCl concentration of 1% in distilled water.

As the temperature of the electrolyte increases due to Joule heating, enhanced evaporation rates occur and the level of liquid inside the cell decreases resulting in higher current density near the cathode. When the electrolyte temperature near the cathode approaches its boiling point, vapor bubbles start to coalesce and form a continuous vapor layer around the cathode resulting in an overall increase in the electrical resistance between the electrodes. Vapor is generated which is composed of a mixture of water vapor and a small fraction of non-condensable gases that are generated due to electrolysis. Since the resistance of the vapor layer is substantially higher than the resistance of the electrolyte, most of the voltage drop occurs across this vapor film resulting in very high electrical field across the film. This high electrical field ionizes the vapor layer stimulating the transition from normal electrolysis to contact glow discharge electrolysis. This transition is accompanied by an increase in voltage where large fluctuations are seen as voltage augments until it stabilizes at a value between 250 V and 300 V, as seen in Fig. 2.3, where the temperature of the solution near the free surface has reached a stable value near its boiling point. A simultaneous decrease in current is observed in Fig. 2.2 during the transition. From the test data, it is observed that transition to CGDE occurs at 250 seconds, 590 seconds, and 230 seconds, for 1% and 2% of $NaHCO_3$, and 1% of $NaCl$, respectively. Therefore, increasing the concentration of $NaHCO_3$ from 1% to 2% delayed transition to CGDE. However, the $NaCl$ solution with a concentration of 1% was slightly faster in transitioning to glow discharge despite the larger electrical conductivity of 1% solution of $NaCl$ compared to a 2% solution of $NaHCO_3$.

These results are explained by observing the temperature variation over time in the electrolytic cell. Figure 2.4 shows the measured temperatures, for a solution of 1% of $NaHCO_3$, recorded at three different depths and radial locations, as depicted in Fig. 2.1. The temperature probe near the free surface of the electrolyte shows a higher rate of temperature increase with temperature stabilizing at a value around 90°C at 400 seconds. The probe submerged at 100 mm shows a much lower rate of temperature increase reaching 50°C after 600 seconds. Finally, temperature measurements at a depth of 150 mm show that the solution remains near ambient conditions for the entire duration of the test. Thus, a very strong temperature gradient occurs inside the electrolytic cell which varies from a temperature near the boiling point close to the free surface of the electrolyte solution to a temperature near ambient conditions at the bottom of the container. The measurements also show that transition to CGDE occurred once the free surface of the electrolyte solution had reached a value close to its boiling point. The voltage, seen in Fig. 2.3, remained relatively stable once the temperature of the surface of the electrolyte
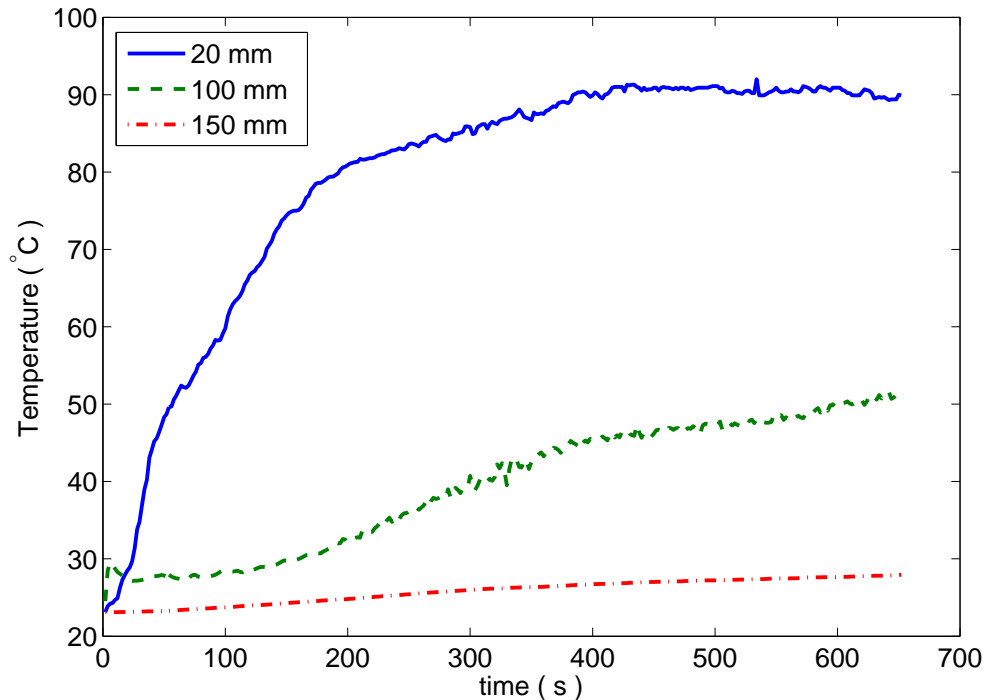
Figure 2.4: Variation of temperature in the electrolytic cell at three different depths from the surface of the electrolyte (1% NaHCO$_3$).

had reached a stable value near 90°C and the electrolytic cell operated in glow discharge mode.

A strong gradient is also observed in Fig. 2.5 for a 2% solution of NaHCO$_3$ in distilled water where the temperature at depths of 20 mm and 100 mm reached 88°C and 85°C, respectively, after 700 seconds. The rate of temperature increase at a depth of 150 mm is substantially lower and the temperature remained below 40°C during the first 700 seconds of the test. These results show that two very distinctive temperature zones are observed in the solution. The results for 1% of NaCl in distilled water are shown in Fig. 2.6, where the temperature measured by the probe submerged near the free surface of the liquid solution rose quickly, reaching 90°C after only 250 seconds. On the other hand, the remaining two temperatures, i.e. depths of 100 mm and 150 mm, stayed near ambient temperature during the entire duration of the test. Thus, the region of cold temperature is much larger than in previous tests with NaHCO$_3$ and the electrolyte solution approached the boiling point only inside a small layer near the free surface.
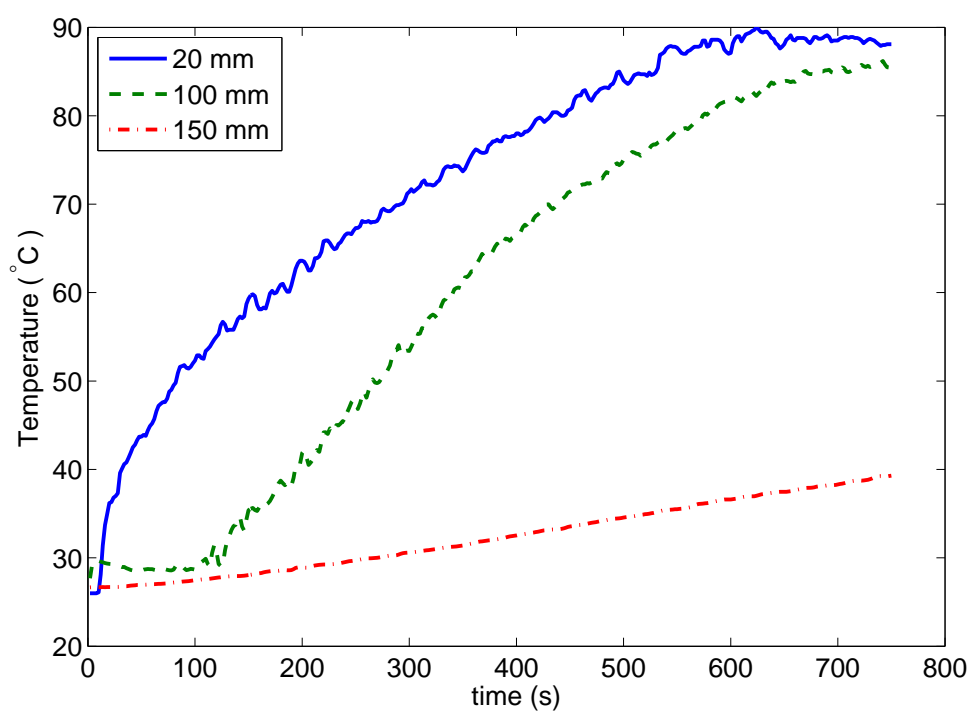
Figure 2.5: Variation of temperature in the electrolytic cell at three different depths from the surface of the electrolyte (2% NaHCO$_3$).
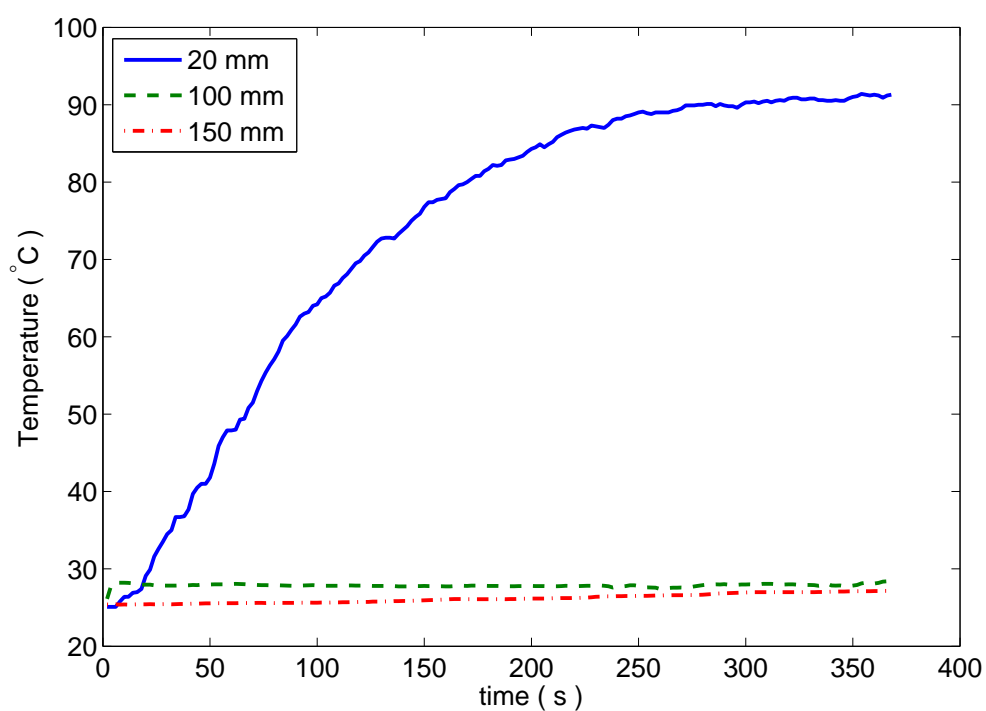
Figure 2.6: Variation of temperature in the electrolytic cell at three different depths from the surface of the electrolyte (1% NaCl).

This two-temperature pattern is formed by two distinct vortices inside the cell that preclude fluid particles in separate vortices to mix and exchange energy by convection. The vortices are formed by a combination of natural convection and the effect of rising vapor bubbles along the wall of the hot cathode.

2.4.1 Steam Generation

A second type of the experiment was performed with the purpose of quantifying the rate of steam generation under contact glow-discharge electrolysis. The basic principles of operation remained the same as described in Section 2.2 but instead of a small-scale electrolytic cell with an open top, a HiTemper™ enclosed steam generator as shown in Fig. 2.7 by Foret Plasma Labs was used [1].

The reactor consists of a cathode made of a 50.8 mm diameter stainless-steel cylindrical screen in coaxial configuration with a stainless-steel screen with 203.2 mm of diameter and 700 mm in length that acts as the anode. The entire assembly is enclosed by a stainless steel reactor that has an inlet at the bottom to allow pumping of electrolyte solution into the reactor, and an outlet at the top for releasing the steam and the small fraction of non-condensable gases generated. Samples taken at the outlet of the reactor showed that non-condensable gases accounted for only 1% to 2% of the mass of the sample with the rest of the product gases being steam. Measurements of the composition of the small fraction of non-condensable gases generated with a 1% solution of $NaHCO_3$ showed 45% of H_2, 33% of CO_2, and 12% of O_2 with smaller fractions of other components also found. The space in between the two stainless steel screens can be filled with electrolyte solution or with a non-conductive media such as gravel, ceramic spheres, rocks, etc., that minimizes the possibility of arcing between the two electrodes. In such configuration, the electrolyte solution occupies the space left by the voids created by the non-conductive material. For the test results obtained in this paper, commercially available gravel was used as the non-conductive material between the screens. Tests were conducted following the same procedure as described in Section 2.2, in which the reactor starts operating in normal electrolysis mode and then it transitions to CGDE. Figures 2.8(a) and 2.8(b) show these two operating modes for a solution of 1% $NaHCO_3$ in distilled water and for stainless-steel cylindrical screen with a diameter of 50.8 mm used as cathode. Due to the larger volume of the reactor, the power supply potentiometer was fixed at half of its full scale.

Figure 2.10 shows the variation of voltage with respect to time for the two configurations tested, i.e. with and without gravel in between the two stainless-steel screens. The variation of voltage and current showed a similar trend as in tests
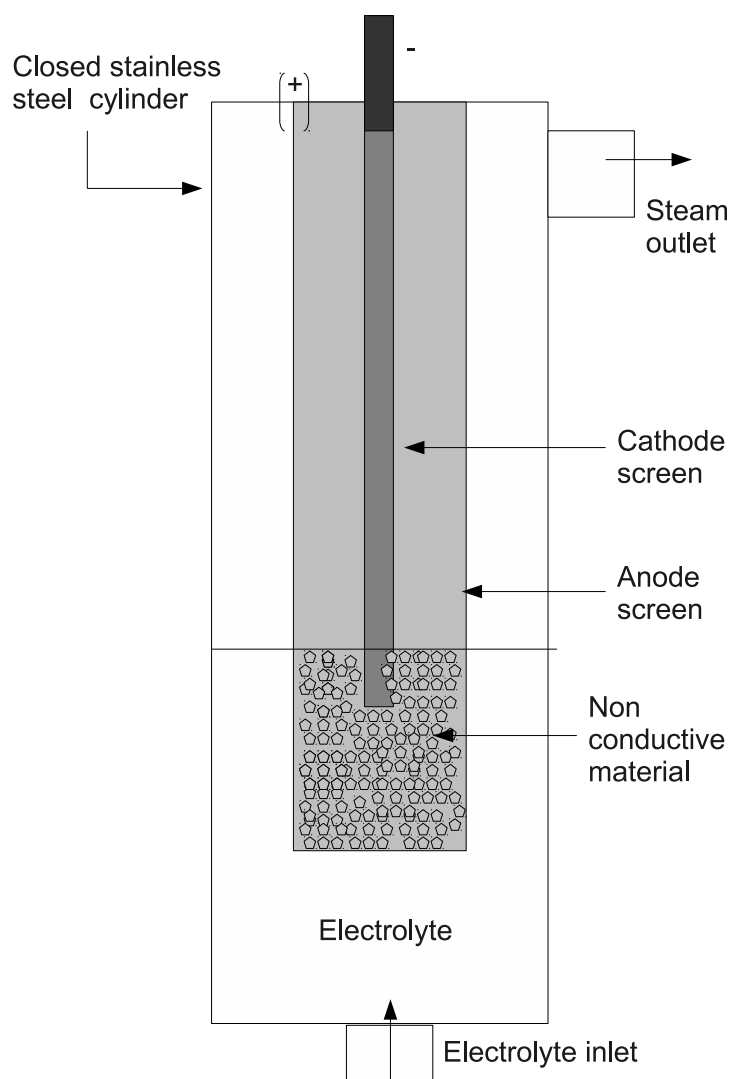
Figure 2.7: Schematic of the HiTemper™ (electrolytic cell) used to generate steam [1].
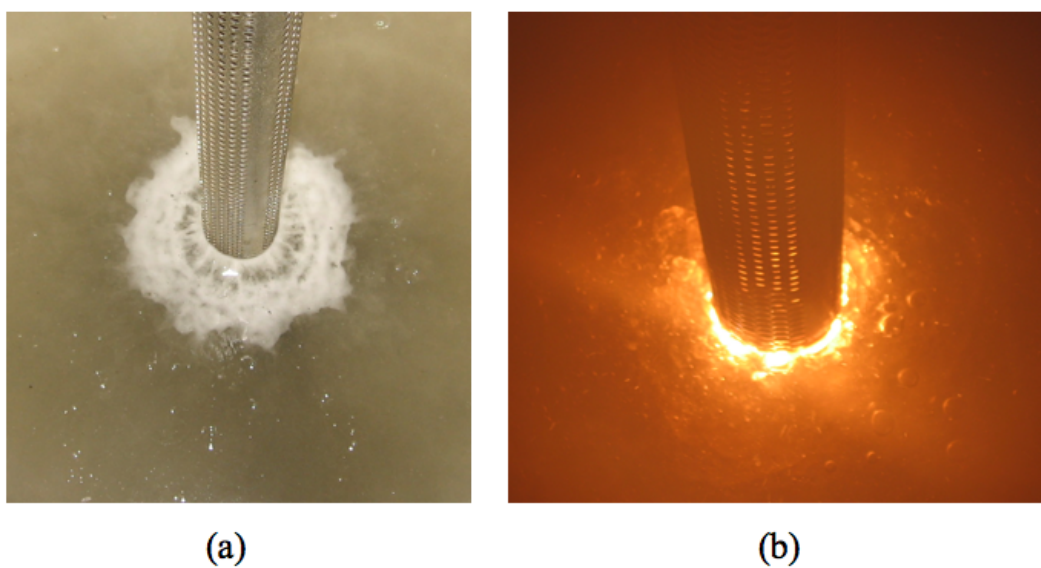
Figure 2.8: Operating modes with stainless steel cathode in 1% solution of NaHCO$_3$. (a) Normal electrolysis, (b) Contact glow discharge electrolysis.

described in Section 2.4, showing a smooth decay of voltage at the beginning of the test from 150 V to 100 V, followed by an increase in voltage when transition to CGDE occurred. The higher potentiometer position resulted in a voltage around 350 V during CGDE operating conditions. The initial reduction in voltage during normal electrolysis occurs because of the increased electrical conductivity of the solution due to Joule-heating related temperature increase. During transition to CGDE, the enclosed nature of the reactor allows for a very smooth increase in voltage as opposed to the tests run with the open electrolytic cell. The presence of the non-conductive material reduces fluctuations on the electrolyte free-surface and thus, smoothes the transition from normal electrolysis to CGDE. Figure 2.11 shows the corresponding variation in current with respect to time for the two configurations. Current increased sharply to 125 A at the very beginning of the test and remained relatively constant during normal electrolysis operating mode. As the voltage started to increase, current decreased at a very low rate until transition to CGDE occurred where a sudden reduction in current from 125 A to 30 A was observed.

The current value was used as a control parameter to monitor the level of liquid inside the reactor. To justify the use of current as a control parameter, a separate experiment was conducted with a small electrolytic cell of stainless steel cylinder as anode and a tungsten cathode of 3.5 mm diameter and 178 mm length. In the beginning of the experiment the level of electrolyte (1% $NaHCO_3$) was below the lower tip of the tungsten cathode. After the voltage was supplied across the electrodes, a constant flow of electrolyte was continuously fed into the cell and level of electrolyte was monitored using a Solinist Levelogger Model No. 3001 sensor. Current through the cell was measured with a current sensor as mentioned in Section 2.1. Figure 2.9 shows the variation of current through the cell with change in the submerged length of the electrode under CGDE operating conditions. For the submerged length between 5 to 50 mm, the variation of current with submerged cathode length behaves linearly. This justifies the use of current as a control parameter for the level of electrolyte in the reactor.

Thus, in the steam generator, which is a closed system, the value of current is used as an indicator for the level of electrolyte. The steam reactor is connected to a separate electrolyte storage tank from which electrolyte can be pumped into the reactor by operating an electric pump. In the present experiment, the electric pump was operated manually to pump the electrolyte into the reactor. However, due to the linear relation between current and liquid level, automatic control could be easily implemented for industrial operation.

After transition to CGDE occurred inside the steam generator, a low value of current was maintained to avoid any possibility of arcing between the electrodes.
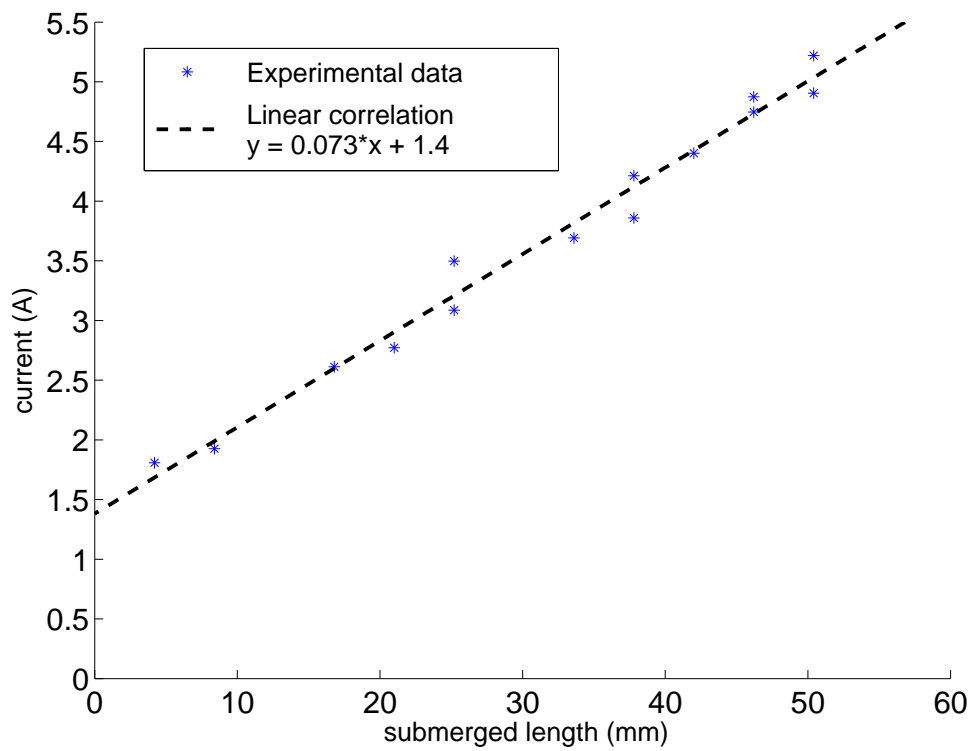
Figure 2.9: Variation of current with length of submerged electrode.

As the current dropped below 30 A, electrolyte solution from a storage tank was pumped inside the reactor increasing the area of the cathode submerged in the solution which augmented the value of the current measured between the electrodes. As steam was produced in CGDE mode, the electrolyte level inside the reactor as well as the current started to decrease. Once current reached 30 A, more electrolyte solution was pumped to the reactor and the cycle was repeated. This explains the sawtooth behavior seen in Figs. 2.10 and 2.11. This procedure ensured a continuous operation of the cell in glow-discharge mode for an extended period of time. If a substantial amount of electrolyte solution was added to the reactor, the process transitioned back to normal electrolysis due to the lower current density at the cathode and also, due to the reduction in temperature of the solution since the makeup solution entered the reactor near ambient conditions. Figures 2.10 and 2.11 also show that transition to CGDE was slower in the configuration without gravel. The volume of fluid inside the reactor with gravel was smaller and as the electrolyte as well as the non-conductive material in the space between the two screens increased their temperatures, the smaller volume of solution approached its boiling temperature faster than in the case without gravel.

To estimate the amount of steam generated in contact glow discharge electrolysis, a test was run for an extended period of time (600 secs) keeping the current and voltage values constant at 30 A and 360 V. Steam was generated at a rate of 12.7 kg/hr in the configuration with gravel and at 10.6 kg/hr in the configuration without gravel. Considering the power consumption during the experiment for each of the two configurations, the estimated efficiency of steam generation was 80% with gravel and 67% without gravel, approximately. Clearly, contact glow-discharge electrolysis constitutes a viable way of generating steam continuously, especially in configuration with gravel that compares well with the generation of steam using boilers which tend to show efficiencies between 65% and 85% [72] .

2.5   Conclusions

Experimental measurements of the transition from normal electrolysis to contact glow discharge electrolysis were performed. The transition was found to occur when the electrolyte solution approached its boiling point and when a critical current density, determined by the area of the cathode in contact with the electrolyte, was reached. Transition to CGDE was accompanied by a substantial increment in voltage and a reduction in current due to substantial increase in overall resistance between the two electrodes due to the formation of a vapor film around the cathode. Such observations have been reported in literature but this dissertation uses this phenomenon for the purpose of quantifying its potential utilization for gener-
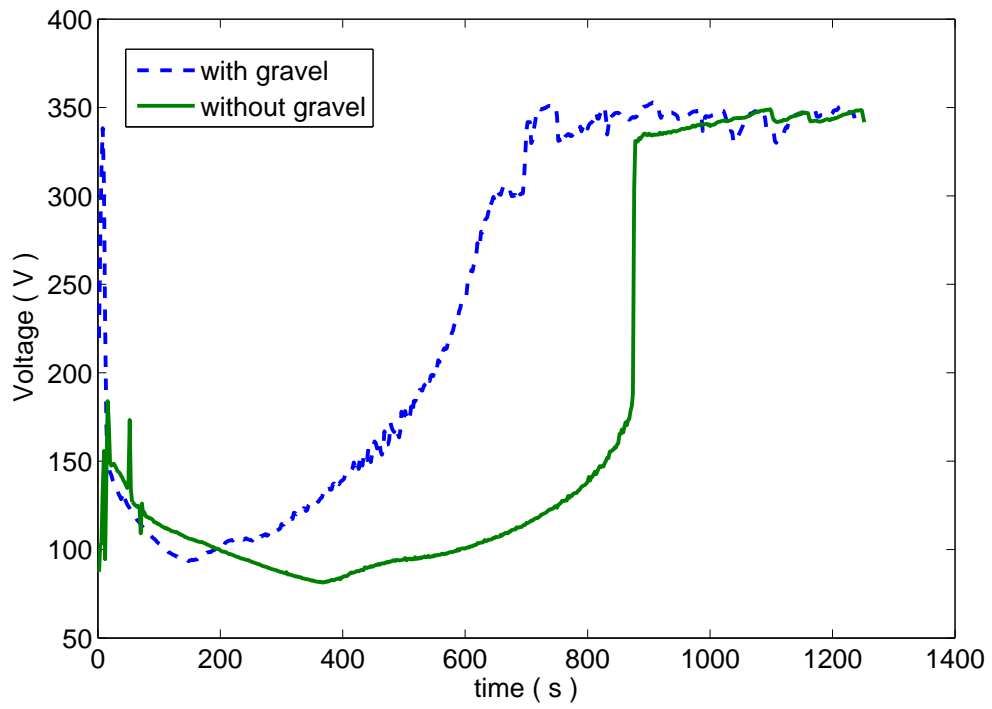
Figure 2.10: Variation of voltage with time during steam generation using glow discharge electrolysis for two different operational conditions, with gravel and without gravel.
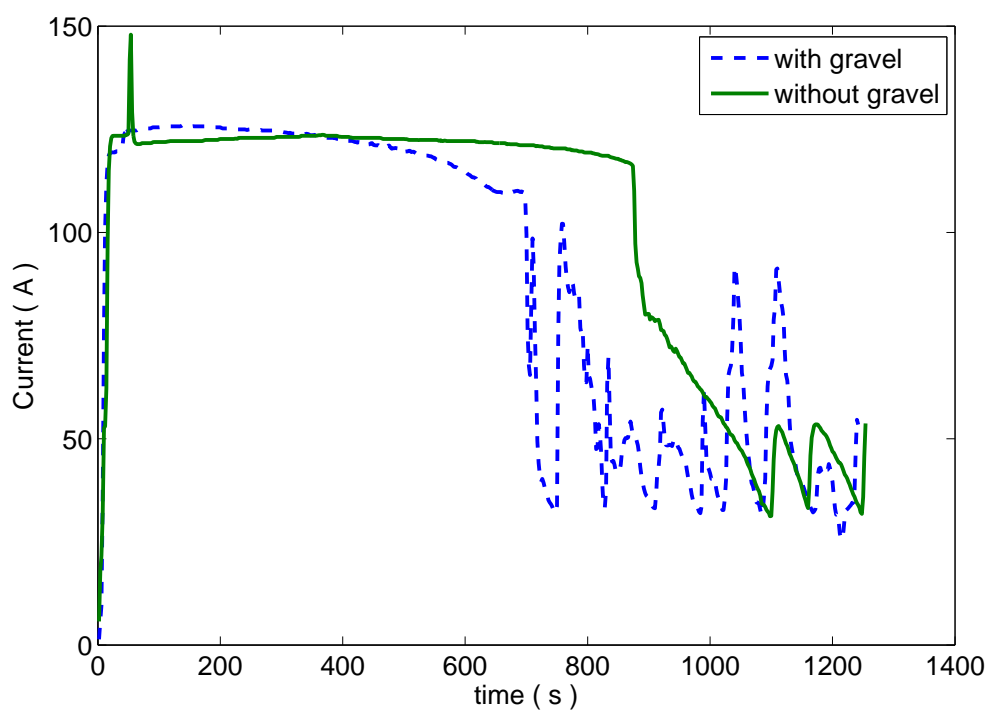
Figure 2.11: Variation of current with time during steam generation using glow discharge electrolysis for two different operational conditions, with gravel and without gravel.

ating steam. This method can be used to generate steam from a variety of liquid wastes. The formation of a two-temperature distribution pattern in the cell is also described and attributed to the formation of counter-rotating vortices within the electrolyte inside the cell. Contact glow discharge electrolysis can be used to efficiently generate steam in continuous mode with steam generation efficiencies of the order of 80%.

Chapter 3

Modeling: evaporation in the presence of applied electric field

The experiment described in the previous chapter provided a rich source of transport phenomena that have not been fully understood. The current chapter provides a theoretical analysis of some of these effects. To better understand the interaction of electric field and liquid waste we apply the theory of electric double layer to model the evaporation of liquid film in the presence of an applied electric field. Because of the presence of salts and minerals, liquid waste acts as electrolyte with considerable presence of free ions. When a nonconducting material is added to the liquid waste to prevent direct arcing, these ions come in contact with the solid surface around the nonconducting material and form what is known as electric double layer. The effect of an externally applied electric field and bulk ion concentration on the evaporation rate of an electrolyte film in contact with a wall is studied numerically. A mathematical model for steady state condition is developed to couple momentum, energy, and mass conservation equations together with the Poisson-Boltzmann equation that describes charge distribution in the liquid film. The model also describes the interaction with humid air flowing above the electrolyte film. The results show nonuniform volumetric heat generation due to Joule heating that induces a temperature variation along the film length and in the direction away from the wall. Work presented in this chapter has been published [67, 73].

3.1   Mathematical Formulation

Most surfaces acquire a surface charge upon coming into contact with a polar medium. Some of the charging mechanisms are ionization, ion dissolution, and
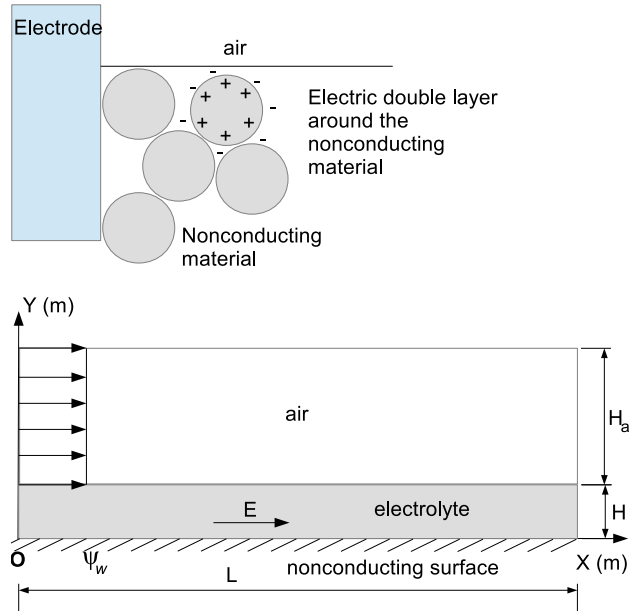
Figure 3.1: Schematic at the top shows a typical surface charge around the non-conducting medium and the electric double layer surrounding it. Schematic at the bottom shows a 2D model for this electric double layer and an adjacent portion of the fluid and air under the simplification of negligible curvatures compared to the thickness of the double layer with $L = 0.005$ m, $H_l = 0.0001$ m, $H_a = 0.0004$ m and ψ_w = -0.075 V.

ion adsorption. The surface charge in an electrolyte solution influences the distribution of nearby ions in the solution. As a result of this electric interaction, ions of opposite charge (counter-ions) are attracted towards the surface while ions of same charge (co-ions) are repelled from the surface. This process of attraction and repulsion combined with the motion of ions leads to the formation of an electric double layer [30]. An externally applied electric field acts upon the charge distribution in the electric double layer and induces momentum transport and joule heating, as shown in Fig. 3.1.

The hydrodynamics and Joule heating due to externally applied electric field are formulated following the description in [74].

3.1.1   Poisson-Boltzmann equation

According to the theory of electrostatics, the electrical potential distribution, $\psi(x,y)$, is governed by the Poisson equation,

$$\nabla \cdot (\varepsilon \, \nabla \psi) = -\frac{\rho_e}{\varepsilon_0} \tag{3.1}$$

where ρ_e is the local charge density, ε_0 is the permittivity of free space ($8.85 \times 10^{-12} \mathrm{C/V\,m}$), ε is the real dielectric constant of the electrolyte which is considered to be a function of temperature, as described in [74].

$$\varepsilon(T) = a \exp\left(-\frac{T}{b}\right) \tag{3.2}$$

where $a = 305.7$, $b = 219K$, and T is temperature in K. In the case of a symmetric electrolyte with co-ions and counter-ions having the same charge valence, its ionic concentration distribution for both anions and cations is assumed to follow the Boltzmann distribution,

$$n^+ = n_0 \exp\left(-\frac{ze\psi}{k_b T}\right), n^- = n_0 \exp\left(\frac{ze\psi}{k_b T}\right) \tag{3.3}$$

where k_b is the Boltzmann constant, e is the fundamental charge, and z is the charge valence of the ions. Once the concentration distributions of cations and anions are known, the local charge density can be calculated as:

$$\rho_e(x,y) = ze\left(n^+ - n^-\right) = -2zen_0 \sinh\left(\frac{ze\psi}{k_b T}\right) \tag{3.4}$$

The Poisson-Boltzmann equation is obtained from Eqs. (3.1) and (3.4) as:

$$\nabla \cdot (\varepsilon \, \nabla \psi) = \frac{2zen_0}{\varepsilon_0} \sinh\left(\frac{ze\psi}{k_b T}\right) \tag{3.5}$$

The distribution of the externally applied electric potential is governed by the Laplace equation,

$$\nabla \cdot (\lambda \, \nabla \phi) = 0 \tag{3.6}$$

where λ is the electrical conductivity of the electrolyte defined below as given in [74]:

$$\lambda(T) = \lambda^+(T)\,\eta^+ + \lambda^-(T)\,\eta^- \tag{3.7}$$

$$\lambda^+(T) = \lambda_0^+ + 0.025\lambda_0^+(T - 298) \tag{3.8}$$

$$\lambda^-(T) = \lambda_0^- + 0.025\lambda_0^-(T - 298) \tag{3.9}$$

where $\lambda^+(T)$ and $\lambda^-(T)$ are ionic conductivities of cations and anions of the electrolyte at temperature T. The terms λ_0^+ and λ_0^- are ionic conductivities of cations and anions of the electrolyte at 298 K and η^+ and η^- are the molar concentrations of cations and anions of the electrolyte, respectively.

3.1.2   Conservation equations in liquid film

In the presence of an applied electric field parallel to the surface, the flow of an electrolyte solution is influenced by the interaction between net charge density in the *EDL* and the applied electric field, and is governed by steady state, incompressible Navier-Stokes equations with an added term to include the effect of electric force. Thus, under the assumption of laminar flow, the governing equations take the following form:

Continuity equation

$$\nabla \cdot \vec{u}_l = 0 \tag{3.10}$$

Momentum equations

The Navier-Stokes equation including the effect of the electric field becomes:

$$\rho_l \, \vec{u}_l \cdot \nabla \vec{u}_l = -\nabla p_l + \nabla \cdot (\mu_l \, \nabla \vec{u}_l) + \rho_e \vec{E} \tag{3.11}$$

where $\vec{E} = -\nabla \phi$ is the strength of the local applied electric field, and μ_l is the temperature dependent viscosity of the electrolyte solution.

Energy equation

The energy equation neglecting viscous dissipation and taking into account Joule heating effect can be expressed as:

$$\rho_l \, C_{p,l} \, (\vec{u}_l \cdot \nabla T_l) = \nabla \cdot (k_l \, \nabla T_l) + \dot{q} \tag{3.12}$$

where k_l is the temperature-dependent thermal conductivity of the electrolyte solution, $\dot{q}$ is the volumetric Joule heating, which consists of two parts: one due to the local applied electric field imposed on the conductive solution $(E\lambda)$, and the other due to the net charge density moving with the flow $(u_l \, \rho_e)$. According to Ohm's law, Joule heating can be expressed as:

$$\dot{q} = \frac{(u_l \, \rho_e + E\lambda)^2}{\lambda} \tag{3.13}$$

3.1.3   Conservation equations on air side

The evaporation of liquid film adds vapor to the air flowing above the film. The heat and mass transfer on the air side and at the interface can be formulated using conservation of momentum, energy, mass, and concentration [41].

Continuity equation

$$\nabla \cdot \vec{u}_a = 0 \tag{3.14}$$

Momentum equations

$$\rho_a \, \vec{u}_a \cdot \nabla \vec{u}_a = -\nabla p_a + \nabla \cdot (\mu_a \, \nabla \vec{u}_a) \tag{3.15}$$

where μ_a is the temperature dependent viscosity, ρ_a is the density, u_a is the velocity, and p_a is the pressure of the air. It is to be observed that no electric field is applied on the air side.

Energy equation

$$\rho_a \, C_{p,a} \left(\vec{u}_a \cdot \nabla T_a \right) = \nabla \cdot (k_a \, \nabla T_a) + \rho_a D_a \left(C_{p,v} - C_{p,a} \right) \frac{\partial m_v}{\partial y} \frac{\partial T_a}{\partial y} \tag{3.16}$$

where C_p is the specific heat at constant pressure, T is the temperature, k_a is the thermal conductivity, D is the diffusion coefficient, and m is the mass fraction. Subscript a and v are for air and vapor respectively. the last term represents energy transport by mass diffusion under the assumption $dh = C_p dT$. Temperature dependent values of μ_l, μ_a, k_l, and k_a are taken from [75] corresponding to water and air.

At steady state, the vapor mass fraction in air is given by,

$$\vec{u}_a \cdot \nabla m_v = D_a \nabla^2 m_v \tag{3.17}$$

3.1.4 Boundary conditions

Table 3.1: Boundary conditions

	Dimensional	Nondimensional
Inlet	$T_l = T_a = T_{in}$	$\bar{T}_l = \bar{T}_a = T_{in}/T_r$
$(x = 0)$	$p_l = 0$	$\bar{p}_l = 0$
	$u_a = 2\,u_r$	$\bar{u}_a = 2$
	$m_v = m_{v,in}$	$m_v = m_{v,in}$
	$\phi = E_0\,L,\ \frac{\partial \psi}{\partial x} = 0$	$\bar{\phi} = 1,\ \frac{\partial \bar{\psi}}{\partial \bar{x}} = 0$
Wall	$u = v = 0$	$\bar{u} = \bar{v} = 0$
$(y = 0)$	$-\left(k\frac{\partial T}{\partial y}\right)_w = 0$	$-\left(\bar{k}\frac{\partial \bar{T}}{\partial \bar{y}}\right)_w = 0$
	$\psi = \psi_w,\ \frac{\partial \phi}{\partial y} = 0$	$\bar{\psi} = \psi_w/\psi_r,\ \frac{\partial \bar{\phi}}{\partial \bar{y}} = 0$
Interface	$u_{l,i} = u_{a,i},\ v_{l,i} = v_{a,i} = 0$	$\bar{u}_{l,i} = \bar{u}_{a,i},\ \bar{v}_{l,i} = \bar{v}_{a,i} = 0$
$(y = H_l)$	$p_{l,i} = p_{a,i},\ T_{l,i} = T_{a,i}$	$\bar{p}_{l,i} = R\,\bar{p}_{a,i},\ \bar{T}_{l,i} = \bar{T}_{a,i}$
	$\left(\mu\frac{\partial u}{\partial y}\right)_{l,i} = \left(\mu\frac{\partial u}{\partial y}\right)_{a,i}$	$\left(\bar{\mu}\frac{\partial \bar{u}}{\partial \bar{y}}\right)_{l,i} = U\left(\bar{\mu}\frac{\partial \bar{u}}{\partial \bar{y}}\right)_{a,i}$
	$-\left(k\frac{\partial T}{\partial y}\right)_{l,i} = -\left(k\frac{\partial T}{\partial y}\right)_{a,i}$	$-\left(\bar{k}\frac{\partial \bar{T}}{\partial \bar{y}}\right)_{l,i} = -K\left(\bar{k}\frac{\partial \bar{T}}{\partial \bar{y}}\right)_{a,i}$
	$+\,(\omega h_{fg})_i$	$+\,(\bar{\omega})_i\,Q_r$
	$\frac{\partial \phi}{\partial y} = 0,\ \frac{\partial \psi}{\partial y} = 0$	$\frac{\partial \bar{\phi}}{\partial \bar{y}} = 0,\ \frac{\partial \bar{\psi}}{\partial \bar{y}} = 0$
	$m_v = m_{v,i}$	$m_v = m_{v,i}$
Top	zero shear stress	
$(y = H_l + H_a)$	$\frac{\partial T}{\partial y} = 0,\ \frac{\partial m_v}{\partial y} = 0$	$\frac{\partial \bar{T}}{\partial \bar{y}} = 0,\ \frac{\partial m_v}{\partial \bar{y}} = 0$
Outlet	$p_l = p_a = 0$	$\bar{p}_l = \bar{p}_a = 0$
$(x = L)$	$\frac{\partial T}{\partial x} = 0,\ \frac{\partial m_v}{\partial x} = 0$	$\frac{\partial \bar{T}}{\partial \bar{x}} = 0,\ \frac{\partial m_v}{\partial \bar{x}} = 0$
	$\phi = 0,\ \frac{\partial \psi}{\partial x} = 0$	$\bar{\phi} = 0,\ \frac{\partial \bar{\psi}}{\partial \bar{x}} = 0$

The boundary conditions described in Table 3.1 along with the parameters defined in Table 3.2 were utilized to solve the set of governing equations. It is assumed that only convective fluxes are present at the outlet for heat and mass transfer. In addition, the interfacial vapor mass flux ω_i is given by:

$$\omega_i = -\left(\frac{\rho_a D_a}{1 - m_v}\frac{\partial m_v}{\partial y}\right)_i \tag{3.18}$$

where the subscript i denotes evaluation at the interface.

Assuming the air-vapor mixture to be an ideal gas and the interface to be in thermodynamic equilibrium, the vapor mass fraction can be written as:

Table 3.2: Values of various parameters used in the simulation.

Parameter	Unit	Values
$C_{p,l}$	J kg^{-1} K^{-1}	4181.3
$C_{p,a}$	J kg^{-1} K^{-1}	1012
$C_{p,v}$	J kg^{-1} K^{-1}	1864
D_a	m^2 s^{-1}	2.56×10^{-5}
E_r	V m^{-1}	30
h_{fg}	J kg^{-1}	2.26×10^{6}
$k_{l,r}$	W m^{-1} K^{-1}	0.6
$k_{a,r}$	W m^{-1} K^{-1}	0.025
M_a	kg mol^{-1}	18×10^{-3}
M_v	kg mol^{-1}	29×10^{-3}
$m_{v,in}$		0.22
n_r	m^{-3}	6.022×10^{23}
T_{in}	K	300
λ_0^+	m^2 S mol^{-1}	[a]50.08×10^{-4}
λ_0^-	m^2 S mol^{-1}	[a]76.31×10^{-4}
$\mu_{l,r}$	Pa s	7.98×10^{-4}
$\mu_{a,r}$	Pa s	1.98×10^{-5}
ρ_l	kg m^{-3}	1000
ρ_a	kg m^{-3}	1.204
ψ_w	V	[a]-0.075
ϵ_r		78.4
z		1

a : Tang el al. [76]

$$m_{v,i} = \frac{M_v p_{v,i}}{M_a \left(p_\infty - p_{v,i}\right) + M_v p_{v,i}} \tag{3.19}$$

where $p_{v,i}$ is the partial pressure of the saturated vapor at the gas-liquid interface. For the case of water vapor, the partial pressure is given by Bertrand's equation [77] :

$$\log_{10}\left(p_{v,i}\right) = 17.443 - \frac{2795}{T_i} - 3.868 \log_{10}\left(T_i\right) \tag{3.20}$$

where $p_{v,i}$ is in *atm* and T_i is in *K*.

3.1.5 Nondimensional equations

The above set of equations are nondimensionalized using the following dimensionless variables and parameters:

$$\bar{x} = x/H_l, \qquad \bar{y} = y/H_l, \qquad \bar{T}_f = T_f/T_r, \qquad \theta = (T - T_{in})/T_{in},$$

$$\bar{\psi} = \psi/\psi_r, \qquad \bar{\phi} = \phi/\phi_r, \qquad \vec{\bar{u}}_f = \vec{u}_f/u_r, \qquad \bar{p}_f = p_f/p_{f,r}, \qquad \vec{\bar{E}} = -\nabla\bar{\phi},$$

$$\bar{\lambda} = \lambda/\lambda_r, \qquad \bar{k}_f = k_f/k_{f,r}, \qquad \bar{\mu}_f = \mu_f/\mu_{f,r}, \qquad \bar{\omega} = \omega/\omega_r, \qquad \bar{\epsilon} = \epsilon/\epsilon_r,$$

$$(3.21)$$

$$Re_f = \frac{\rho_f u_r H_l}{\mu_{f,r}}, \qquad Pr_f = \frac{\mu_{f,r} C_{p,f}}{k_{f,r}}, \qquad G = \frac{D_a(C_{p,v} - C_{p,a})}{H_l u_r C_{p,a}},$$

$$A_r = \frac{\rho_{e,r} u_r H_l}{\phi_r \lambda_r}, \qquad B = \frac{2\beta n_r ze\phi_r}{\rho_l u_r^2}, \qquad F = H_l\sqrt{\frac{2\beta n_r z^2 e^2}{\epsilon_r \epsilon_0 k_b T_r}}, \qquad \alpha = E_0/E_r,$$

$$Q_r = \frac{\omega_r h_{fg} H_l}{\phi_r^2 \lambda_r}, \qquad K = \frac{k_{a,r}}{k_{l,r}}, \qquad R = \frac{\rho_a}{\rho_l}, \qquad U = \frac{\mu_{a,r}}{\mu_{l,r}}, \qquad \beta = n_0/n_r.$$

where,

$$T_r = \frac{\phi_r^2 \lambda_r}{k_{l,r}}, \qquad u_r = \frac{\epsilon_r \epsilon_0 |\psi_w| \alpha E_r}{\mu_{l,r}}, \qquad \psi_r = \frac{k_b T_r}{ze}, \qquad \rho_{e,r} = 2\beta n_r ze.$$

$$\lambda_r = \lambda_0^+ \eta_+ + \lambda_0^- \eta_-, \qquad \phi_r = \alpha E_r L, \qquad p_{f,r} = \rho_f u_r^2, \qquad \omega_r = \frac{\rho_a D_a}{H_l}$$

The governing equations in nondimensional form using the above set of variables and parameters are given below.

Electric potential:

$$\nabla \cdot \left(\bar{\epsilon}\,\nabla\bar{\psi}\right) = F^2 \sinh\left(\bar{\psi}/\bar{T}\right) \qquad (3.22)$$

$$\nabla \cdot \left(\bar{\lambda}\,\nabla\bar{\phi}\right) = 0 \qquad (3.23)$$

Liquid film:

$$\nabla \cdot \vec{\bar{u}}_l = 0 \tag{3.24}$$

$$\vec{\bar{u}}_l \cdot \nabla \, \vec{\bar{u}}_l = -\nabla \bar{p}_l + \frac{1}{Re_l} \left[\nabla \cdot \left(\bar{\mu}_l \, \nabla \vec{\bar{u}}_l \right) \right] - B \, \vec{\bar{E}} \, \sinh \left(\bar{\psi} / \bar{T}_l \right) \tag{3.25}$$

$$\vec{\bar{u}}_l \cdot \nabla \bar{T}_l = \frac{1}{Re_l \, Pr_l} \left[\nabla \cdot \left(\bar{k}_l \, \nabla \bar{T}_l \right) \right] + \frac{1}{Re_l \, Pr_l} \frac{\left(A_r \bar{\rho}_e \bar{u}_l + \bar{E} \bar{\lambda} \right)^2}{\bar{\lambda}} \tag{3.26}$$

Air film:

$$\nabla \cdot \vec{\bar{u}}_a = 0 \tag{3.27}$$

$$\vec{\bar{u}}_a \cdot \nabla \, \vec{\bar{u}}_a = -\nabla \bar{p}_a + \frac{1}{Re_a} \left[\nabla \cdot \left(\bar{\mu}_a \, \nabla \vec{\bar{u}}_a \right) \right] \tag{3.28}$$

$$\vec{\bar{u}}_a \cdot \nabla \bar{T}_a = \frac{1}{Re_a \, Pr_a} \left[\nabla \cdot \left(\bar{k}_a \, \nabla \bar{T}_a \right) \right] + G \frac{\partial m_v}{\partial \bar{y}} \frac{\partial \bar{T}_a}{\partial \bar{y}} \tag{3.29}$$

$$\vec{\bar{u}}_a \cdot \nabla m_v = \frac{1}{Sc \, Re_a} \nabla^2 m_v \tag{3.30}$$

$$\bar{\omega}_i = -\frac{1}{1 - m_v} \frac{\partial m_v}{\partial \bar{y}} \tag{3.31}$$

3.2   Results and discussion

The Poisson-Boltzmann equation together with the coupled momentum, energy, and mass transfer equations along with the specified boundary conditions were implemented and solved in 2D using the commercial finite element software COMSOL Multiphysics 3.5 [78]. A total of 18000 (300×60) and 6000 (300×20) quadrilateral elements in the liquid film and air, respectively, were used in the simulations. A nonuniform grid along the thickness of the liquid film was used so as to capture the boundary layer interaction between electric field and fluid. The solver UMFPACK, which solves general systems of the form $Ax = b$ using the nonsymmetric-pattern multifrontal method and direct LU factorization of the sparse matrix A, was used for the simulations. COMSOL Multiphysics estimates the error of the solution during each iteration. The convergence criterion is $\rho |M^{-1}(b - Ax)| < tol |M^{-1}b|$, where ρ is a factor in error estimate (default is 400), tol is the relative tolerance specified at 10^{-6}, and $M = LU$ with L and U being the LU factors computed by the solver. Once the error estimate is small enough

as determined by the convergence criteria, the software terminates the computations and returns a solution [78]. Grid independence was verified by refining the grid until no significant difference was observed in the results. Also, to verify the validity of results from the software, the normalized velocity profile in an electroosmotic flow in a capillary under the effect of externally applied electric field was compared to the analytical results of the Rice-Whitehead solution discussed in [2]. Even though the case chosen for comparison is that of internal flow as opposed to external flow, the main purpose of such a comparison is to establish that the software is able to handle the complex interaction between externally applied electric field, electric double layer, and the resulting hydrodynamics. The flows in both cases are driven by an externally applied electric field, which acts on the electric charge distribution established inside the electric double layer. The comparison of the results shows excellent agreement between the analytical and numerical solutions, as shown in Fig. 3.2, where "κ" is the inverse of Debye length, "a" is the radius of a single long and uniform capillary containing the electrolyte.

In the present work, the electric field acts on the charge distribution in the electric double layer along with the ions present in the region outside the double layer. The motion of the charges due to the presence of the electric field gives rise to an electric current that causes the temperature in the liquid film to increase due to the Joule heating effect. Since the surface potential has a negative value, the charge distribution in the double layer is predominantly positive. The length of the domain analyzed is $L = 0.005$ m, the initial thickness of the liquid film $H_l = 0.0001$ m, and the height of the air section is $H_a = 0.0004$ m, with a surface potential $\psi_w = $ -0.075 V. The dimensions and parameters are taken to be approximately the same as in reference [76].

A uniform velocity profile is imposed at the air inlet and no velocity profile is imposed at the inlet of the electrolyte film. The flow in the liquid film is driven by the applied electric field, which varies along the length of the film according to Eq. (3.23). This electric field acts on the charge distribution inside the electric double layer resulting in the velocity profile depicted in Fig. 3.3, where α and β represent dimensionless electric field and dimensionless number concentration, respectively. As the net charge distribution is confined within the electric double layer, the interaction between electrostatics and hydrodynamics are resolved by means of using a fine mesh near the wall surface. Representative values for the Reynolds number, inside the electric double layer and in the air adjacent to the interface, are $Re_l = 2.5 \times 10^{-4}$ and $Re_a = 3 \times 10^{-5}$, respectively. The Prandtl numbers for liquid and air are $Pr_l = 5.6$ and $Pr_a = 0.8$, respectively. The small values of the Reynolds number indicate the extremely small thickness of the electric double layer formed adjacent to the wall.
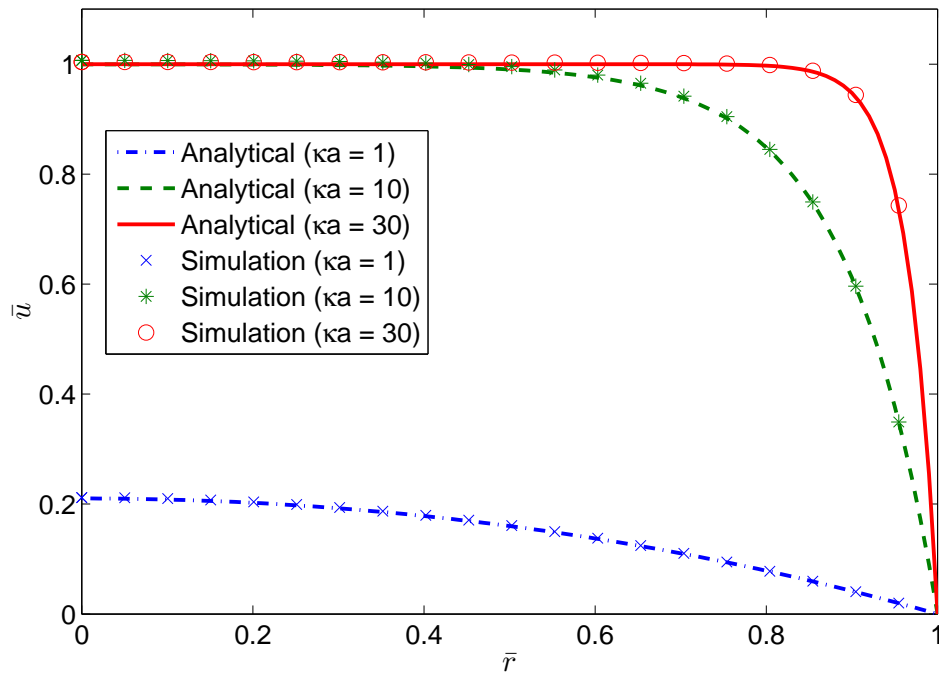
Figure 3.2: Validation of results from COMSOL simulation against analytical results for the normalized velocity profile from the Rice-Whitehead solution discussed in reference [2]. κ is the inverse of Debye length and a is the radius of a single long and uniform capillary containing an electrolyte.
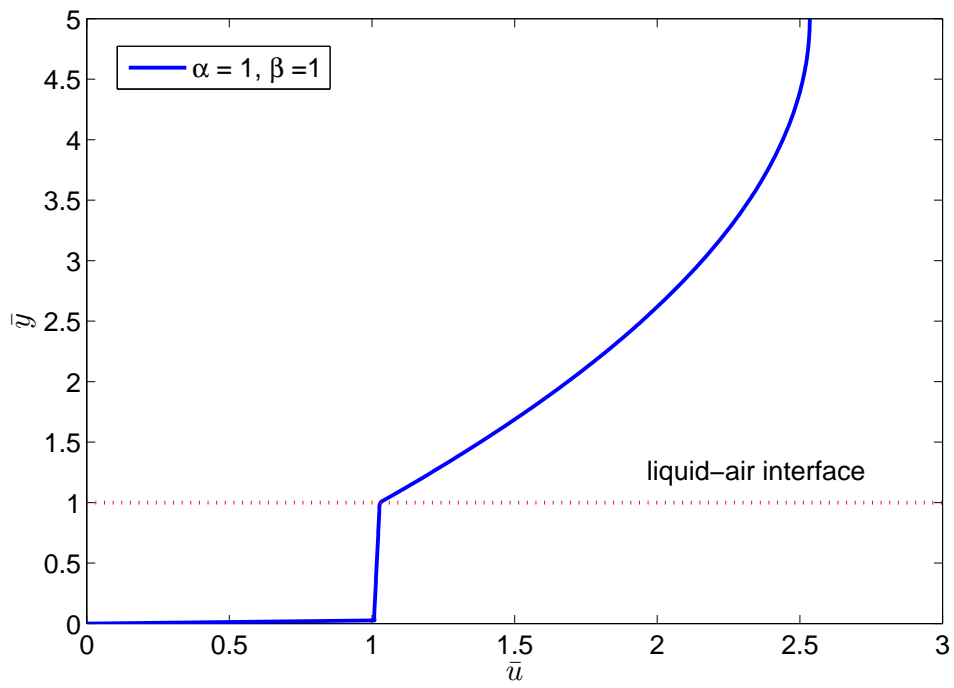
Figure 3.3: Velocity profiles in liquid film and humid air domains at location $\bar{x} = 30$.
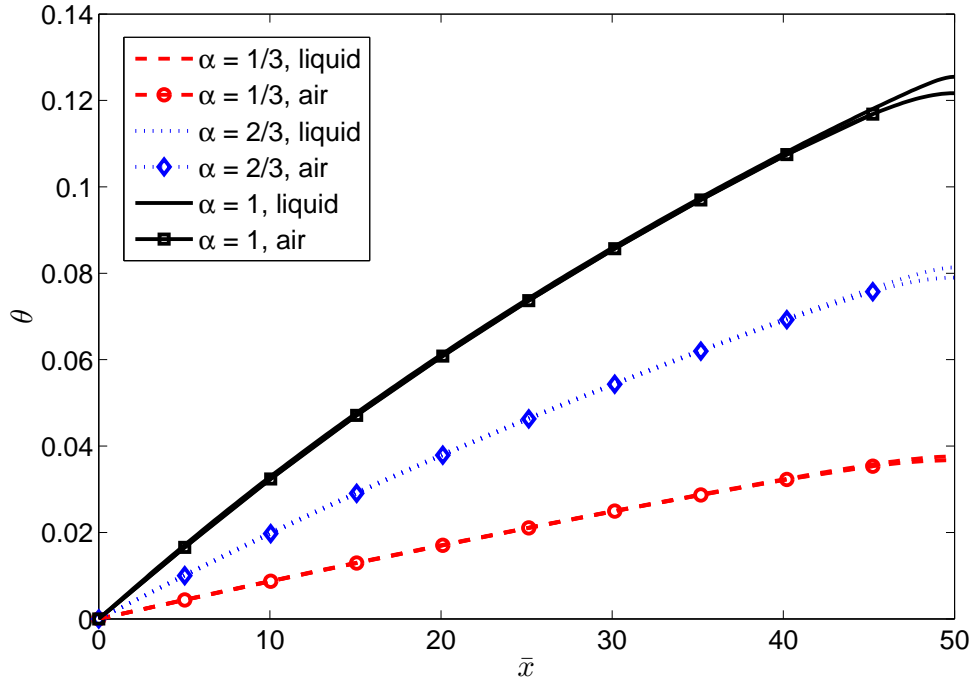
Figure 3.4: Temperature variation in liquid film and air along the length of the domain at $\bar{y} = 0.5$ and $\bar{y} = 3$, respectively. Results are obtained for $\beta = 5$ and different values of dimensionless applied electric field, α.

In order to show the effect of the applied electric field on the temperature distribution, Fig. 3.4 depicts the temperature distribution in the liquid film and humid air along the length of the domain at locations $\bar{y} = 0.5$ and $\bar{y} = 3$ from the wall. The applied electric field plays a role in both, the momentum as well as the energy conservation equations as described by Eqs. (3.25) and (3.26), respectively. Volumetric heat generation increases with increase in the applied electric field resulting in higher temperatures in both liquid and air. The nondimensional outlet temperature, θ, of the liquid film increased by 0.038, 0.081, and 0.125 when nondimensional external electric fields, α, of 1/3, 2/3, and 1 were applied, respectively. As a result of the volumetric heat generation, the rate of evaporation along the liquid film length also augments. This can be observed by analyzing the vapor mass fraction of the air near the liquid-air interface.

The variation of the vapor mass fraction along the length of the liquid film at $\bar{y} = 3$ is shown in Fig. 3.5. At a constant dimensionless number concentration, $\beta = 5$, the increase in nondimensional applied electric field, α, from 1/3 to 2/3
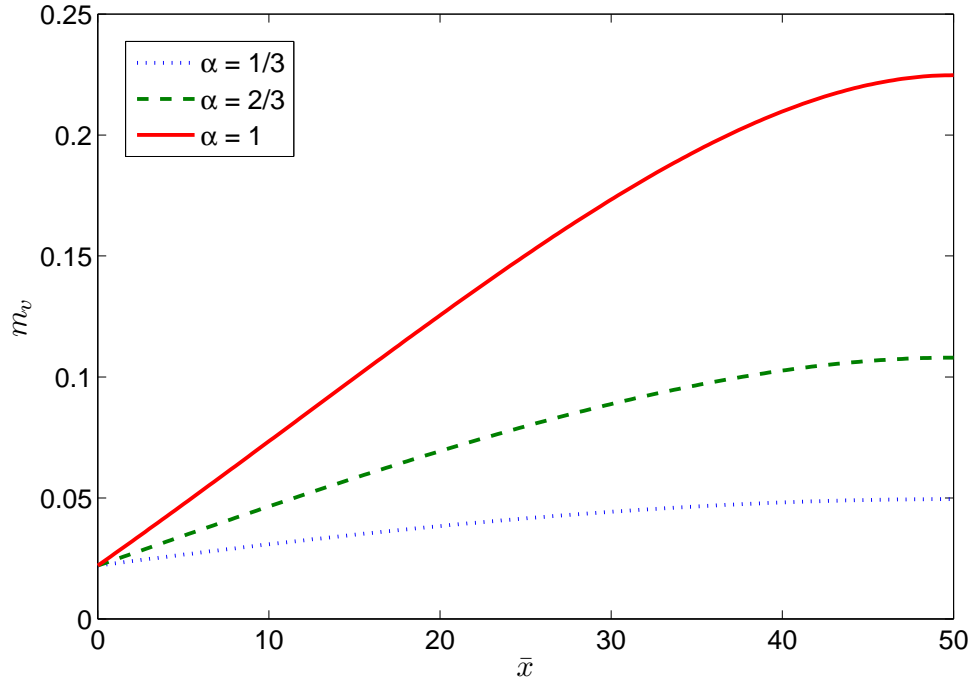
Figure 3.5: Vapor mass fraction in air along the length of the domain at $\bar{y} = 3$ for $\beta = 5$ and different values of dimensionless applied electric field, α.

raised the vapor mass fraction from 0.049 kg$_v$/kg$_a$ to 0.12 kg$_v$/kg$_a$. An increase of α to a value of 1 increased the vapor mass fraction to 0.224 kg$_v$/kg$_a$. It is observed that mass flow rate of liquid is much larger than the mass liquid that evaporates, so the changes in the thickness of the liquid film were neglected in this analysis.

The effect of bulk ion concentration on the temperature along the length of the electrolyte-film and air domains at constant external electric field ($\alpha = 1$) is shown in Fig. 3.6. The bulk ion concentration, β, affects charge density in the electric double layer as well as the electrical conductivity of the electrolyte as described by Eqs. (3.4) and (3.7). β plays a minor role in the hydrodynamics of the liquid film since the effect relates only to the electric double layer, as described by Eq. (3.25). However, β has a substantial role in Joule heating through Eq. (3.26) since it affects the entire domain of the electrolyte. As the bulk ion concentration increases, volumetric Joule heating increases, resulting in an increase in the rate of evaporation as shown in Fig. 3.7.

The presence of the electric double layer near the wall surface causes more Joule heating near the wall, thus, raising its temperature. On the other hand,
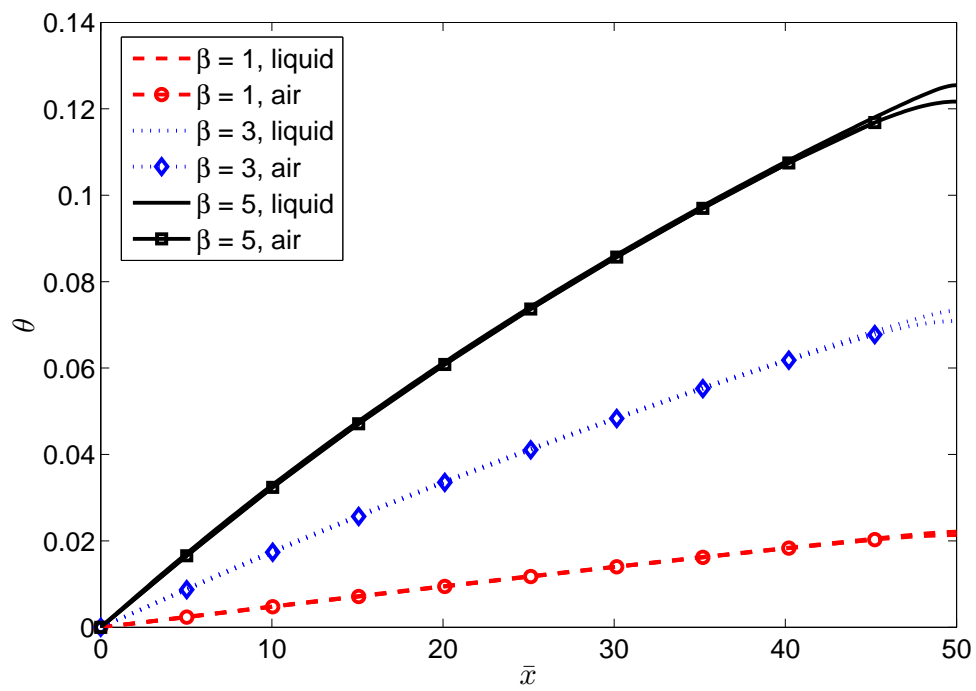
Figure 3.6: Temperature variations in liquid film and air along the length of the domain at $\bar{y} = 0.5$ and $\bar{y} = 3$, respectively. Results are obtained for $\alpha = 1$ and different values of dimensionless number concentration, β.
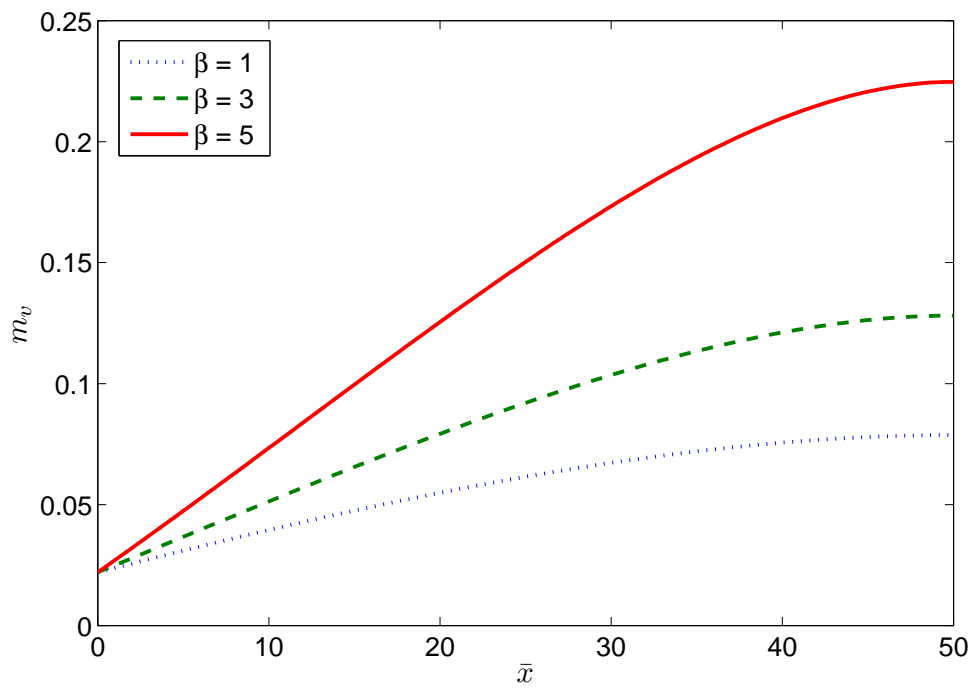
Figure 3.7: Vapor mass fraction in air along the length of the film at $\bar{y} = 3$ for $\alpha = 1$ and dimensionless number concentration, β.
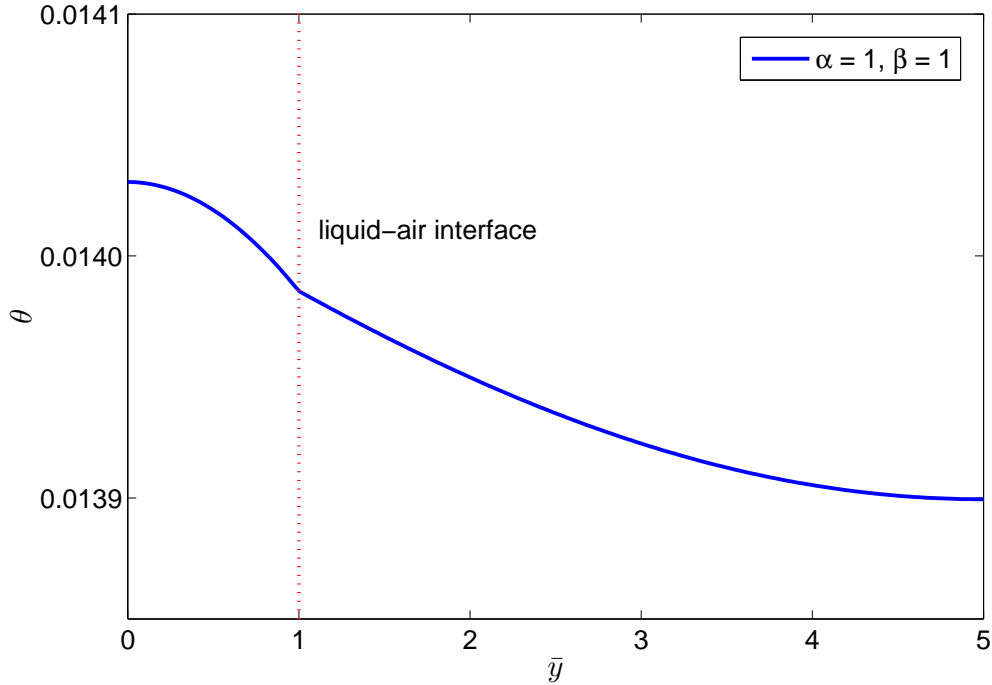
Figure 3.8: Temperature variation in liquid film and humid air across the thickness of the domain at $\bar{x} = 30$.

evaporation occurring at the liquid free surface decreases the film temperature at the air-liquid interface causing a temperature gradient along the thickness of the film. The temperature distribution across the liquid film and humid air is shown in Fig. 3.8 for values of $\alpha = 1$ and $\beta = 1$ at an arbitrary location $\bar{x} = 30$. The decrease in temperature in the direction towards the liquid-air interface results in the decrease in the electric conductivity of the electrolyte and causes a slight reduction in the rate of Joule heating across the film thickness. Therefore, a nonuniform volumetric heat generation distribution is obtained.

3.3 Conclusions

Evaporation of an electrolyte film in the presence of an externally applied electric field is studied. The only source of heat generation is the volumetric Joule heating due to the presence of the applied electric field. Also, the flow is solely driven by the interaction of applied electric field with charge distribution in elec-

tric double layer. The presence of the electric field results in a coupling of the momentum, energy, and mass transfer equations that are solved simultaneously with the Poisson-Boltzmann equation that describes the electric potential distribution. The results show that the rate of evaporation at the air-liquid interface is a strong function of the applied electric field and bulk ion concentration.

Chapter 4

Modeling: buoyancy driven flow with partially immersed electrode

The CGDE experiment performed in Chapter 3 showed distinctive temperature patterns formed inside the electrolytic cell. This chapter provides a mathematical model of the thermal effects that generate such temperature distributions. As a first approximation, no interaction of liquid and electric field has been included. Temperature distribution under the effect of buoyancy-driven flow in a cylindrical tank with an electrode acting as a partially immersed heating element is presented numerically for steady-state conditions. As the heating element does not extend along the entire axial length of the cylindrical tank, this configuration displays very particular vortex patterns inside the cell and divides the domain into two regions of different temperatures. Heat transfer rates at the heating element and the inner wall of the cylindrical tank are indicated by calculating the Nusselt number along these surfaces. With the increase in aspect-ratio, Nusselt number at the surface of the heating element increases while the Nusselt number at the inner surface of the cylindrical tank decreases. Analysis is done in dimensionless form considering temperature-dependent properties in a general framework of weakly compressible flow without applying the Boussinesq approximation.

4.1 Mathematical Formulation

The governing equations for buoyancy-driven flow include mass, momentum, and energy conservation with temperature dependent density, viscosity, thermal conductivity, and specific heat. In most of the literature equations are simplified by invoking Boussinesq approximation, which is valid only for small variations of density with respect to temperature ($\Delta\rho/\rho \ll 1$). In many situations this con-

dition does not apply. In the present study steady-state laminar fluid flow and heat transfer is modeled without Boussinesq approximation and using equations for weakly compressible fluid flow at low Mach number. A schematic of the con-
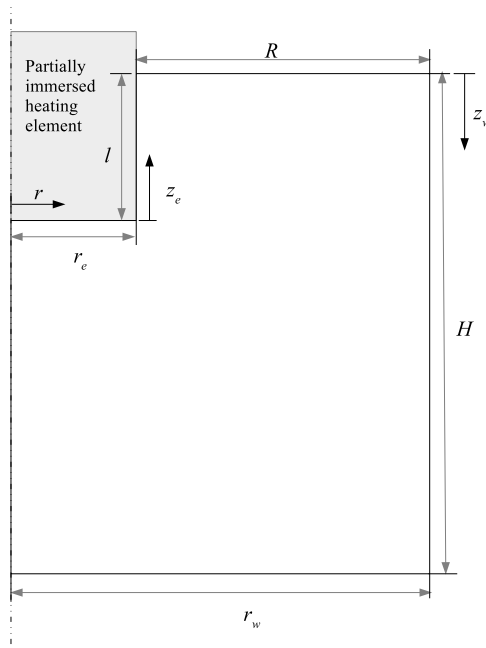
Figure 4.1: Schematic of cylindrical container with partially immersed heating element.

figuration is presented in Fig. 4.1, where r_w corresponds to the radius of the outer cylinder, r_e the radius of the heating element, l is the submerged depth of the heating element, H is the height of the outer cylinder, and R is the difference between the radius of the heating element and the cylindrical tank. As the boundary layers develop at the electrode and the cylinder walls in opposite directions, for convenience we have defined two z coordinates. One, z_e, is measured from the submerged tip of the electrode and the other, z_w, is measured from the top of the outer cylinder wall.

The governing equations for weakly compressible fluid [79] are written in nondimensional form as follows:

$$\bar{\rho}\left(\vec{\bar{u}} \cdot \bar{\nabla}\vec{\bar{u}}\right) = \bar{\nabla} \cdot \left[-\bar{p}\underline{\underline{I}} + \frac{\bar{\mu}A}{Re}\left(\bar{\nabla}\vec{\bar{u}} + \left(\bar{\nabla}\vec{\bar{u}}\right)^T\right) - \frac{2\bar{\mu}A}{3Re}\left(\bar{\nabla} \cdot \vec{\bar{u}}\right)\underline{\underline{I}}\right] + \frac{\bar{\rho}}{Fr}\vec{\bar{g}} \quad (4.1)$$

$$\bar{\nabla} \cdot \left(\bar{\rho}\vec{\bar{u}}\right) = 0 \quad (4.2)$$

$$\bar{\rho}\bar{C}_p\left(\vec{\bar{u}} \cdot \bar{\nabla}\bar{T}\right) + \frac{1}{Pe}\bar{\nabla} \cdot \left(-\bar{k}\bar{\nabla}\bar{T}\right) = 0 \quad (4.3)$$

The above set of nondimensional equations are obtained using the following dimensionless variables and parameters:

$$\bar{\rho} = \rho/\rho_r, \qquad \bar{C}_p = C_p/C_{p,r}, \qquad \bar{k} = k/k_r, \qquad \vec{\bar{u}} = \vec{u}/u_r, \qquad \vec{\bar{g}} = \vec{g}/g \quad (4.4)$$
$$\bar{\nabla}\cdot = L_r\nabla\cdot, \qquad \bar{\mu} = \mu/\mu_r, \qquad \bar{p} = (p - p_0)/p_r, \qquad \bar{T} = (T - T_0)/T_r$$

$$Ra = \frac{g\beta_r T_r L_r^3}{\nu_r \alpha_r}, \qquad Re = \frac{\rho_r u_r R}{\mu_r}, \qquad Fr = \frac{u_r}{\sqrt{gL_r}}, \qquad Pe = \frac{\rho_r C_{p,r} u_r L_r}{k_r}, \quad (4.5)$$

$$Pr = \frac{\mu_r C_{p,r}}{k_r}, \qquad A = \frac{R}{l}$$

where,

$$R = r_w - r_e, \qquad L_r = l, \qquad p_r = \rho_r u_r^2, \qquad T_r = T_e - T_0, \quad (4.6)$$
$$u_r = \sqrt{g\beta_r T_r L_r}/\sqrt{Pr}, \qquad \rho_r = \rho\left(T_0\right), \qquad \mu_r = \mu\left(T_0\right), \qquad \nu_r = \mu_r/\rho_r,$$
$$C_{p,r} = C_p\left(T_0\right), \qquad k_r = k\left(T_0\right), \qquad \alpha_r = k_r/\left(\rho_r C_{p,r}\right)$$

It is noted that the length scale used to nondimensionalize the governing equations is the submerged length of the heating element. Choice of this length scale becomes apparent under the limit of very large partial annulus gap (R) for which the problem reduces to that of natural convection around a heated vertical cylinder. Also, the representative Reynolds number is calculated using R as the length scale, which is the natural choice for defining Reynolds number for flow inside an annulus. The reference velocity is defined so as to achieve nondimensional velocities of the order of unity.

4.2   Results and Discussion

The numerical simulation of the steady-state heat transfer and buoyancy-driven laminar flow in a cylinder with partially submerged heating element described by Eqs. 4.1 to 4.3 was performed using the commercial software COMSOL

3.5a, which is used as a PDE solver. Estimation of thermal and outer boundary layer thicknesses, as explained in [80], were taken into account in generating meshes so as to resolve the boundary layers appropriately. Mesh independence has been verified by comparing simulation results for a sequence of cases with decreasing mesh sizes until mesh independence was achieved. A combination of triangular elements for the bulk and quadrilateral elements for the boundary layer were used for all cases analyzed. Simulations were carried out for different values of Rayleigh number, Ra, and inner-cylinder aspect ratio, $A = R/l$. Values of parameters used in the simulations are given in Table 4.1 and boundary conditions are described in Table 4.2.

Table 4.1: Values of various parameters used in simulations with water as the fluid.

Parameter	Unit	Values
$C_{p,r}$	J kg^{-1} K^{-1}	4180
g	m s^{-2}	9.81
k_r	W m^{-1} K^{-1}	0.6
β_r	K^{-1}	2.76×10^{-4}
μ_r	Pa s	8.55×10^{-4}
ρ_r	kg m^{-3}	997
T_0	K	300

Table 4.2: Boundary Conditions

Boundary	Thermal	Fluids
axis	axisymmetric	axisymmetric
electrode surface	$\bar{T} = 1$	wall, no-slip
cylinder wall	$\hat{n} \cdot \left(-\bar{k}\bar{\nabla}\bar{T} \right) = \text{Nu}\ \bar{T}$	wall, no-slip
top	$\hat{n} \cdot \left(-\bar{k}\bar{\nabla}\bar{T} \right) = \text{Nu}\ \bar{T}$	wall, slip
bottom	insulation	wall, no-slip

Figures 4.2(a) and 4.2(b) show the results of the simulations in terms of streamlines and temperature distribution for two different Rayleigh numbers. It is observed that for a low value of Rayleigh number ($Ra = 0.14 \times 10^5$), the flow pattern shown in Fig. 4.2(a) is markedly different with only one vortex formed within the

entire domain as opposed to the multiple vortices that are formed for a higher Rayleigh number ($Ra = 84.2 \times 10^5$), as shown in Fig. 4.2(b). It is observed that the temperature distribution is also quite different between the two cases, with high temperatures being mainly located near the surface of the heating element (inner cylinder) for $Ra = 0.14 \times 10^5$ in contrast to the two-zone temperature distribution seen for $Ra = 84.2 \times 10^5$, where a relatively uniform temperature profile is seen in the upper section of the domain (in between the two cylinders) that is located on top of a much cooler region at the bottom of the tank.

A typical variation of vertical velocity along the radial direction at half depth of the heating element, at $\bar{z}_e = 0.5$, is shown in Fig. 4.3 for $Ra = 10.5 \times 10^5$ and $A = 4$. The plot shows the formation of two boundary layers, one at the surface of heating element and the other at the surface of the outer cylinder. Velocities inside the boundary layer near the heating element are nearly five times higher because of the stronger buoyancy effects in that region.

Figure 4.4 shows a typical variation of temperature in the radial direction at two different vertical locations, i.e. $\bar{z}_w = 0.5$ and $\bar{z}_w = 3.0$, for a case of multiple vortex formation with $Ra = 10.5 \times 10^5$ and $A = 4$, where the dotted line denotes the location of the surface of the heating element. Again, z_e is measured from the submerged tip of the electrode and z_w is measured from the top of the cylindrical wall. The figure shows a clear thermal stratification with higher temperatures in the region adjacent to the submerged heating element. Similar thermal stratification patterns have also been reported in a experimental study performed by the authors [69] for the case where the heating element is replaced by an electrode inside an electrolytic cell. It is seen that the temperature profiles at both vertical locations remain relatively uniform for most of the domain but it varies inside the boundary layers. The local Nusselt numbers at the surface of heating element and on the internal wall of outer cylinder have been defined as,

$$Nu_e = -\frac{1}{|\Delta\bar{T}|_{max}} \left(\frac{\partial\bar{T}}{\partial\bar{r}}\right)_e \tag{4.7}$$

$$Nu_w = -\frac{\bar{H}}{|\Delta\bar{T}|_{max}} \left(\frac{\partial\bar{T}}{\partial\bar{r}}\right)_w \tag{4.8}$$

where, $|\Delta\bar{T}|_{max}$ is the maximum driving temperature difference (defined as $|\bar{T}_e - \bar{T}_w|_{\bar{z}_w=0}$) as suggested for thermally stratified fluid reservoirs in [80].
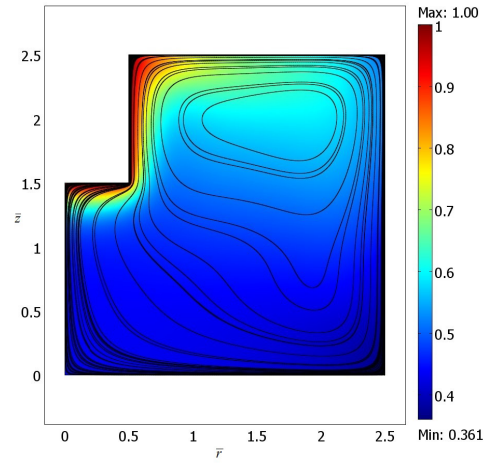
(a) $Ra = 0.14 \times 10^5$
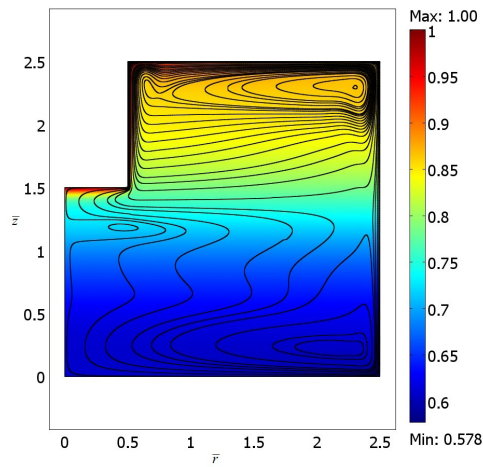
(b) $Ra = 84.2 \times 10^5$

Figure 4.2: Temperature distribution and streamlines for flow with different Rayleigh numbers and same aspect ratio ($A = 2$). (a) $Ra = 0.14 \times 10^5$, (b) $Ra = 84.2 \times 10^5$.
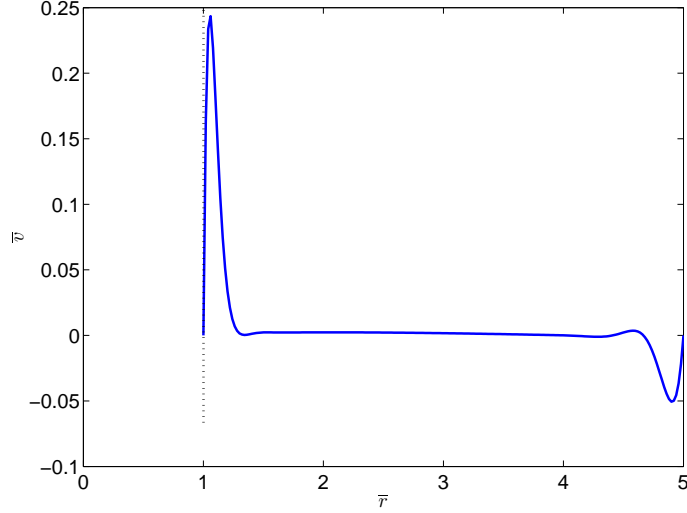
Figure 4.3: Variation of vertical velocity with respect to radial direction at a location where $\bar{z}_e = 0.5$ for $Ra = 10.5 \times 10^5$ and $A = 4$. Dotted line indicates the location of the bottom tip of the heating element.

Average Nusselt numbers at the two surfaces are defined as,

$$\overline{Nu}_e = -\frac{1}{|\Delta \bar{T}|_{max}} \int_0^1 \left(\frac{\partial \bar{T}}{\partial \bar{r}} \right)_e d\bar{z}_e \qquad (4.9)$$

$$\overline{Nu}_w = -\frac{1}{|\Delta \bar{T}|_{max}} \int_0^{\bar{H}} \left(\frac{\partial \bar{T}}{\partial \bar{r}} \right)_w d\bar{z}_w \qquad (4.10)$$

Figure 4.5 shows the variation of local Nusselt number at the surface of the heating element with respect to the distance from the lower end, $\bar{z}_e$, as the boundary layer develops along this surface with velocities in the upward direction. As the fluid rises, it absorbs the thermal energy from the heating element and its temperature rises. This in turn decreases the gradient of the temperature in the radial direction and, thus, lowers the magnitude of the Nusselt number. Nu_e decreases from a value around 15 at the tip of the heating element to a value near 3 at the free surface of the liquid. As expected, the Nusselt number increases with the increase in Rayleigh number. Figure 4.6 shows the variation of the local Nusselt number at the outer cylinder surface with respect to the distance from the top, $\bar{z}_w$, as the boundary layer develops from top to bottom and for a heating element with an aspect ratio $A = 4$. Due to the thermal stratification and formation of two vortices, the Nusselt number is, in general, higher at the upper part
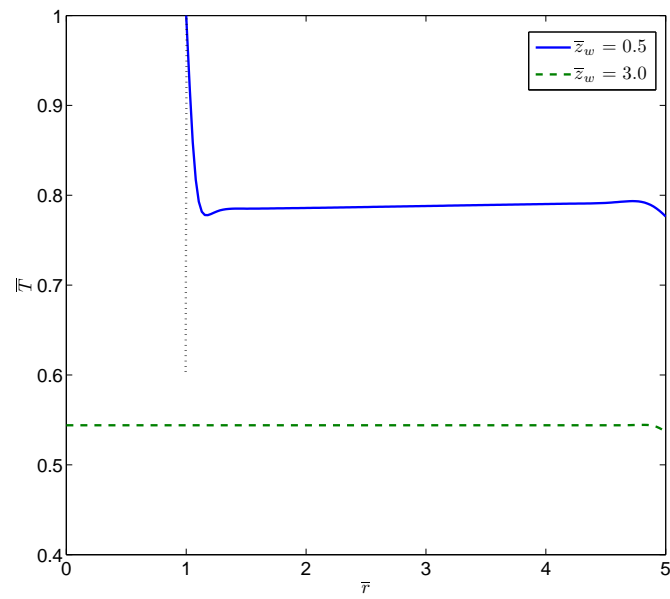
Figure 4.4: Variation of temperature with respect to radial direction at depths of $\bar{z}_w = 0.5$ and $\bar{z}_w = 3$ for $Ra = 10.5 \times 10^5$ and $A = 4$. Dotted line indicates the location of the cylindrical surface of the heating element.
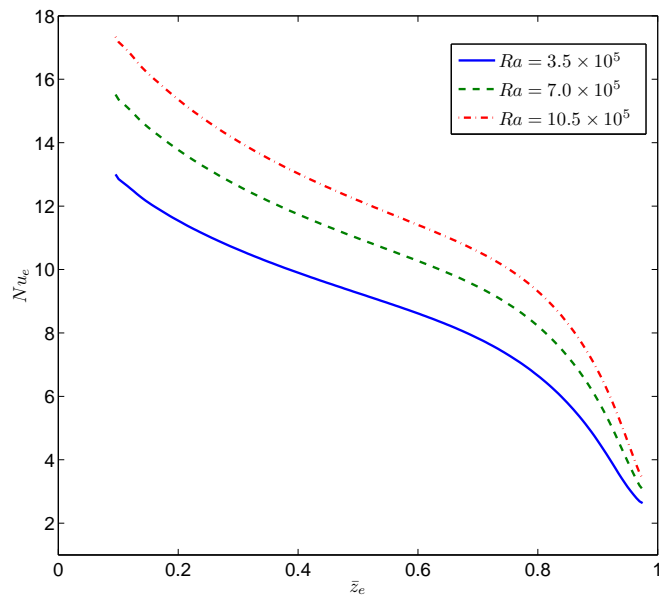
Figure 4.5: Variation of local Nusselt number along the vertical surface of the immersed heating element for different Rayleigh numbers for $A = 4$.

of the cylinder compared to the lower section. Fluid that was in contact with the heating element flows radially near the free surface of the domain and gets into contact with the upper section of the outer cylinder wall. Most of the heat trans-
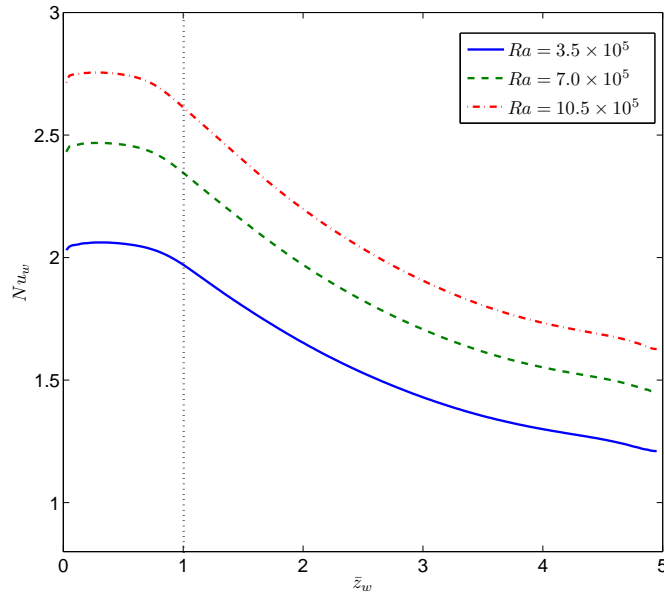
Figure 4.6: Variation of local Nusselt number along the surface of cylindrical tank for different Rayleigh numbers and $A = 4$. Dotted line indicates the location of the bottom tip of the heating element.

fer occurs due to the presence of the vortex located between the heated element and the tank wall, therefore, increasing the value of Nu_w in the section of the tank wall in close proximity to this vortex. The rest of the fluid domain remains at a lower temperature and does not play a significant role in transferring heat from the heating element to the tank wall, so Nu_w decreases considerably near the bottom of the tank. The vertical dotted line in the figure shows the position of the tip of the submerged heating element. It is clear that the submerged length determines the interface of thermal stratification. It is also seen that the Nusselt number increases with increasing Rayleigh number. The effect of Rayleigh number on average Nusselt number at the heating element and outer cylinder wall for different aspect ratios is presented in Figs. 4.7 and 4.8, respectively. An increase in aspect ratio indicates an increase in the difference between the radii of the heating element and cylindrical tank for a fixed height of the heating element. For a higher value of aspect ratio (A=4), the heating element is able to dissipate
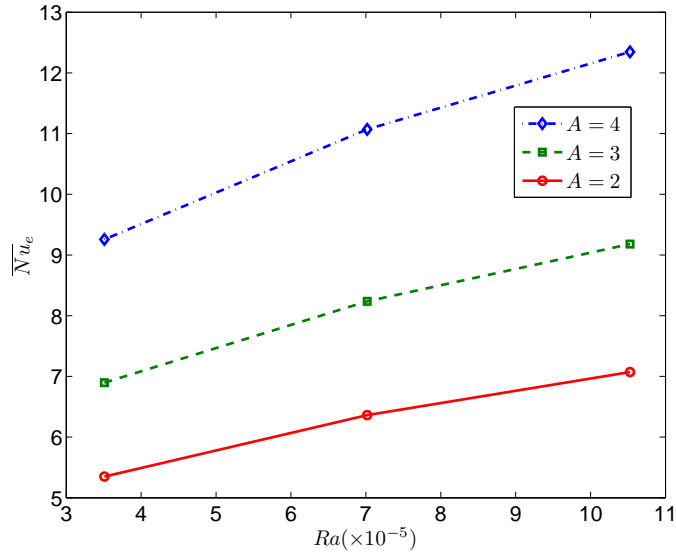
Figure 4.7: Variation of average Nusselt number along the vertical surface of immersed heating element with respect to Rayleigh number for different aspect ratios.

thermal energy more effectively when compared to a lower value aspect ratio, i.e. A=3 and A=2, because the vortex located in between the heating element and tank wall contains a larger volume of fluid so its bulk temperature tends to be lower than for smaller aspect ratios, therefore increasing the potential of heat transfer at the heating-element surface.

The trend is reversed for average Nusselt number at the tank wall, as seen in Fig. 4.8, where $\overline{Nu_w}$ decreases with the increase in aspect ratio. The effect of Rayleigh number is more pronounced at the tank wall where a positive slope is obtained as Ra increased, as opposed to a flat profile seen at the surface of the heating element, especially for low aspect ratios.

4.3 Conclusions

Buoyancy-driven flow in a cylindrical tank with a partially immersed heating element has been formulated in nondimensional form and solved numerically without Boussinesq approximation. Thermal stratification of flow inside the domain is reported and explained. The results indicate that partial immersion of a heating element results in a much higher temperature near the free surface of the fluid,
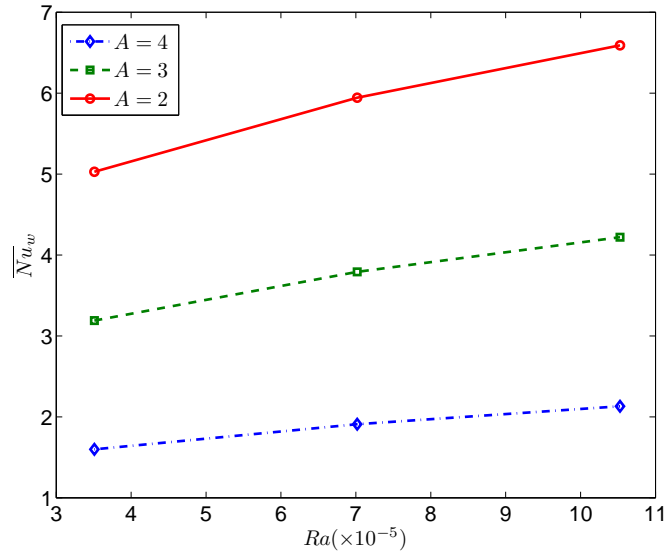
Figure 4.8: Variation of average Nusselt number along the wall of the cylindrical tank with respect to Rayleigh number for different aspect ratios.

and much lower temperatures near the bottom of the tank. The pattern occurs due to the formation of vortices that appear inside the domain that depend on the value of the Rayleigh number and aspect ratio. Results are shown in terms of local and average Nusselt numbers at the surface of the heating element and cylindrical tank wall for different values of aspect ratio and Rayleigh numbers.

Chapter 5

Modeling: glow discharge in vapor film

5.1 Introduction

The process of contact glow discharge electrolysis is initiated by the high electric field that exists near the cathode as a result of a vapor film formed around the cathode [68]. After the formation of a thin film of vapor around the electrode, the entire voltage drop takes place within this thin film because of substantially higher electrical resistivity of the film compared to the rest of the system which results in breakdown of vapor into glow discharge mode. Gas discharges have been extensively studied by many researchers, both experimentally and theoretically. Initial interest in modeling such discharges was restricted to gases at low pressure; more recently the interest in atmospheric pressure discharges has been growing. Even though the chemical kinetics and the level of ionization are very different for low pressure and high pressure discharges, the underlying physics is similar and researchers have been able to modify and extend the models developed for low pressure discharges to atmospheric pressure.

We start by surveying the existing models for low pressure discharges with the aim to eventually extend the model to atmospheric pressure contact glow discharge electrolysis with respect to parameters like variation of electric field, level of ionization, and electron and ion densities in the glow discharge region next to the cathode.

Ward [5] modified the Townsend's basic ionization equations for cold-cathode gas discharge between parallel plates to account for space-charge effect. The author concluded that, at lower values of current density, the electric field was

nearly linear with distance, but for higher current density the electric field was large at the cathode.

Most of the early authors assumed a linear variation of the electric field in the cathode fall region (region near cathode across which most of the potential drop happens). Neuringer [81] performed an analytic investigation of the cathode fall region without explicitly assuming a linear variation of the electric field. But in the analysis the effect of ratio of ion to electric drift velocity in the discharge equations was neglected. Davies and Evans [82] further extended the work of Neuringer to provide an analytic relationship between the electric field and the electron current density within the entire discharge gap. In a review paper [83] Davies first presented methods to model electrical discharges in a gaseous dielectric assuming all charged particles to be at equilibrium with ionization and transport coefficients. As this assumption is not valid near the electrodes, the author presented possible models for ionization growth in nonequilibrium regions, such as the cathode-fall region.

5.2 Physical model

As explained in Chapter 2, glow discharge takes place in a thin liquid film surrounding the electrode. Figure (5.1) shows the schematic of the vapor film formed around the electrode. On one side the film is bounded by the electrode, which acts as a heat source as well as a current source. On the other side the film is bounded by liquid waste which acts as a source for continuous generation of vapor.
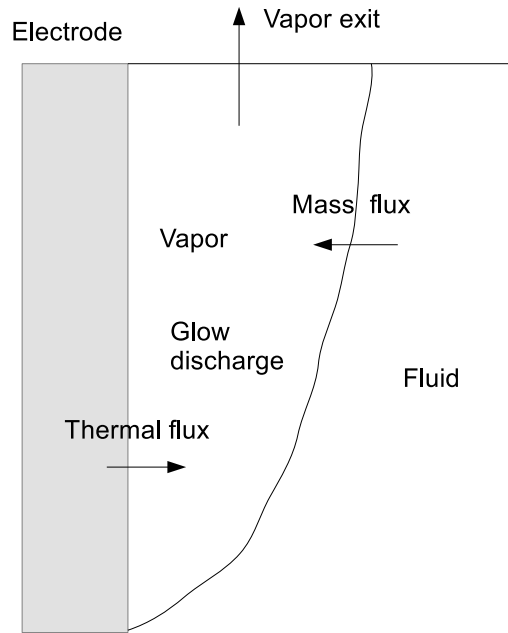
Figure 5.1: Schematic of vapor film formed around the electrode in glow discharge mode.

The thickness of the vapor film depends upon the dynamic balance between the pressure exerted by the fluid and the pressure generated inside the film due to continuous formation of vapor. The thickness of the gap governs the intensity of electric field generated inside the vapor film, because the potential difference between the electrode and the vapor-fluid interface is almost equal to that of applied voltage. This is because of the fact that resistivity of vapor is much higher than that of fluid and so most of the potential drop happens across the vapor gap. Even though the gap width does not attain a steady-state value because of the transient nature of forces and its value depends upon the vertical location on the electrode, as a preliminary approximation we have considered a one-dimensional gap for the purpose of modeling glow discharge inside the film. More complexity in terms of variable gap width changing with time can be added later to simulate the actual process more closely.

5.3 Mathematical model

Next we describe a mathematical model developed by Shi and Kong [84] which combines relevant models from the literature to build a hybrid model for atmo-

spheric pressure glow discharges that treats the cathode fall region kinetically (nonequilibrium) but retains the hydrodynamic (equilibrium) description for the region between the thin cathode fall layer and the anode.

The hydrodynamic model for gas discharge consists of a conservation equation for charged particles (electrons and ions) combined with Poisson's equation for electric field and potential as

$$\frac{\partial n_e}{\partial t} + \nabla \cdot \Gamma_e = S_e, \tag{5.1}$$

$$\frac{\partial n_i}{\partial t} + \nabla \cdot \Gamma_i = S_i, \tag{5.2}$$

$$\nabla \cdot (\epsilon \vec{E}) = |e| \, (n_i - n_e), \tag{5.3}$$

$$\vec{E} = -\nabla V, \tag{5.4}$$

where $n_{i,e}$, $\Gamma_{i,e}$ and $S_{i,e}$ are particle densities, particle fluxes, and particle creation rates. As mentioned in [84], when the electrode gap is much smaller than the characteristic length of the electrode, multidimensional effects can be neglected. In contact glow discharge electrolysis, even though the electrode gap is large, the actual region of glow discharge is restricted to a very thin vapor layer/film surrounding the cathode and the thickness of this film can be considered as the effective electrode gap. We can further simplify the above set of equations employing the following set of assumptions:

1. system geometry allows 1D modeling.

2. stepwise and Penning ionization are negligible compared to direct ionization.

3. under the applied dc voltage, the discharge reaches steady state without arcing.

4. electrons and ions reach their equilibrium drift velocities on a spatial and temporal scale much smaller than the corresponding scale of variation of the electric field.

5. recombination rates are much lower than ionization rates.

The vapor film thickness can be estimated by performing mass and momentum balance in a control volume enclosing the vapor film. The expression is given by

$$\delta = \sqrt{\frac{8\dot{q}z_e\nu_v}{(\rho_l - \rho_v)h_{fg}g}},$$

where $\dot{q}$ is the volumetric heat generation, z_e is the z coordinate from the tip of the electrode, ν_v is the kinematic viscosity of vapor, ρ_l is the density of the liquid, ρ_v is the density of vapor, h_{fg} is the enthalpy of vaporization of the liquid, and g is the gravity. The simplified set of equations is

$$\frac{\mathrm{d}J_e}{\mathrm{d}z} = \alpha_T J_e, \tag{5.5}$$

$$\frac{\mathrm{d}J_i}{\mathrm{d}z} = -\alpha_T J_i, \tag{5.6}$$

$$\frac{\mathrm{d}E}{\mathrm{d}z} = \frac{1}{\epsilon}\left(\frac{J_i}{v_i} - \frac{J_e}{v_e}\right), \tag{5.7}$$

$$J_{i,e} = \pm|e|\,n_{i,e}v_{i,e}, \tag{5.8}$$

where α_T, $J_{i,e}$ and $v_{i,e}$ are the Townsend first coefficient, current densities, and drift velocities of ions and electrons. Eqns. (5.5) and (5.6) indicate that the total current density $J = J_i + J_e$ remains constant during the discharge. Introducing $j_e = J_e/J$ as the normalized electron current density, the above set of equations can further be reduced to

$$\frac{\mathrm{d}j_e}{\mathrm{d}z} = \alpha_T j_e, \tag{5.9}$$

$$\frac{\mathrm{d}E}{\mathrm{d}z} = \frac{J}{\epsilon v_i}\left[1 - \left(1 + \frac{v_i}{v_e}\right)j_e\right]. \tag{5.10}$$

The above set of equations supplemented with expressions and parameters given in Tables 5.1 and 5.2 and appropriate boundary conditions is solved for electron and ion densities and the electric field. Value of normalized current density at the anode is specified as $j_e = 1$ and the value of electric field at the anode is specified as $E = 131.349$ V/cm for the case with argon and $E = 33847.0728$ V/cm for the case of water vapor. The case with argon at low pressure is run to validate the code. The case with water vapor is of interest in the present research. For the case with water vapor, values of α_T and v_e are taken from [6].

5.4   Results

A code in C was written to solve the above set of equations. Runge-Kutta method (RK-4) was used to integrate the Eqns. (5.9) and (5.10) on a grid with 10^6 divisions and gap width of 1 cm for argon and 0.4 cm for Water Vapor. For verifying the code, simulation with argon using the expressions and parameters

Table 5.1: Values of various parameters used in simulations with argon [5].

Parameter	Unit	Values
p	Torr	10
J	A cm^{-2}	5.62×10^{-6} p^2 (p in Torr)
gap width	cm	1
$\underline{A}$	cm^{-1} Torr^{-1}	31.5
$\underline{B}$	V$^{1/2}$ cm$^{-1/2}$ Torr$^{-1/2}$	27.1
α_T	cm^{-1}	$\underline{A}$ p exp(-$\underline{B}$ p$^{1/2}$ E$^{-1/2}$)
$v_{\underline{i}}$	cm s^{-1}	$\mu_{\underline{i}}$ E
$v_{\underline{e}}$	cm s^{-1}	$-\mu_{\underline{e}}$ E
$\mu_{\underline{i}}$	cm^2 V^{-1} s^{-1}	1444/p (p in Torr)
$\mu_{\underline{e}}$	cm^2 V^{-1} s^{-1}	3.0×10^5/p (p in Torr)

Table 5.2: Values of various parameters used in simulations with water vapor [6].

Parameter	Unit	Values
p	Torr	760
J	A cm^{-2}	0.18
gap width	cm	0.4
$v_{\underline{i}}$	cm s^{-1}	$\mu_{\underline{i}}$ E
$v_{\underline{e}}$	cm s^{-1}	$-\mu_{\underline{e}}$ E
$\mu_{\underline{i}}$	cm^2 V^{-1} s^{-1}	0.61×10^3

given in Table 5.1 is run and the results are analyzed. The results match well with the solution obtained by Ward [5]. Figure 5.2 shows the variation of electric field in glow discharge established between the electrodes in the presence of argon. As observed in glow discharges, in cathode fall region the electric field decreases almost linearly with distance from the cathode. As electrons generated near cathode accelerate towards anode in the cathode fall region to reach equilibrium with the local electric field after leaving the cathode fall region, the normalized electron current density increases near the cathode as shown in Fig. 5.3 and reaches unity around towards the end of the cathode fall region.
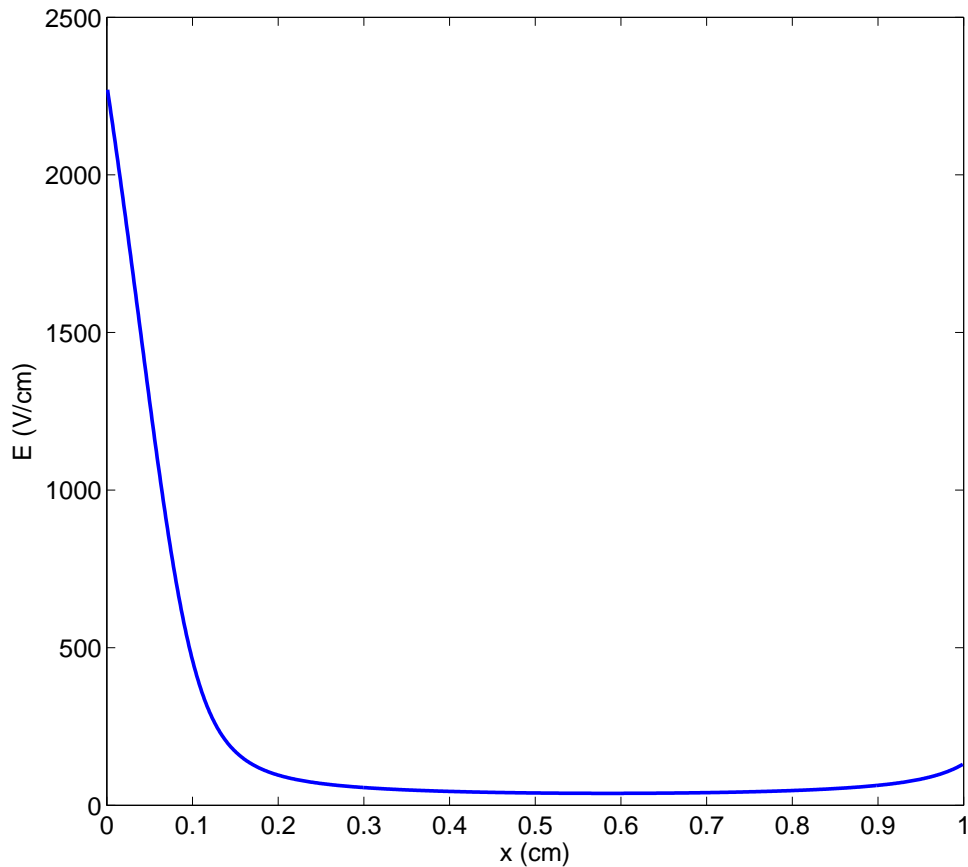
Figure 5.2: Spatial variation of electric field in the gap (argon).
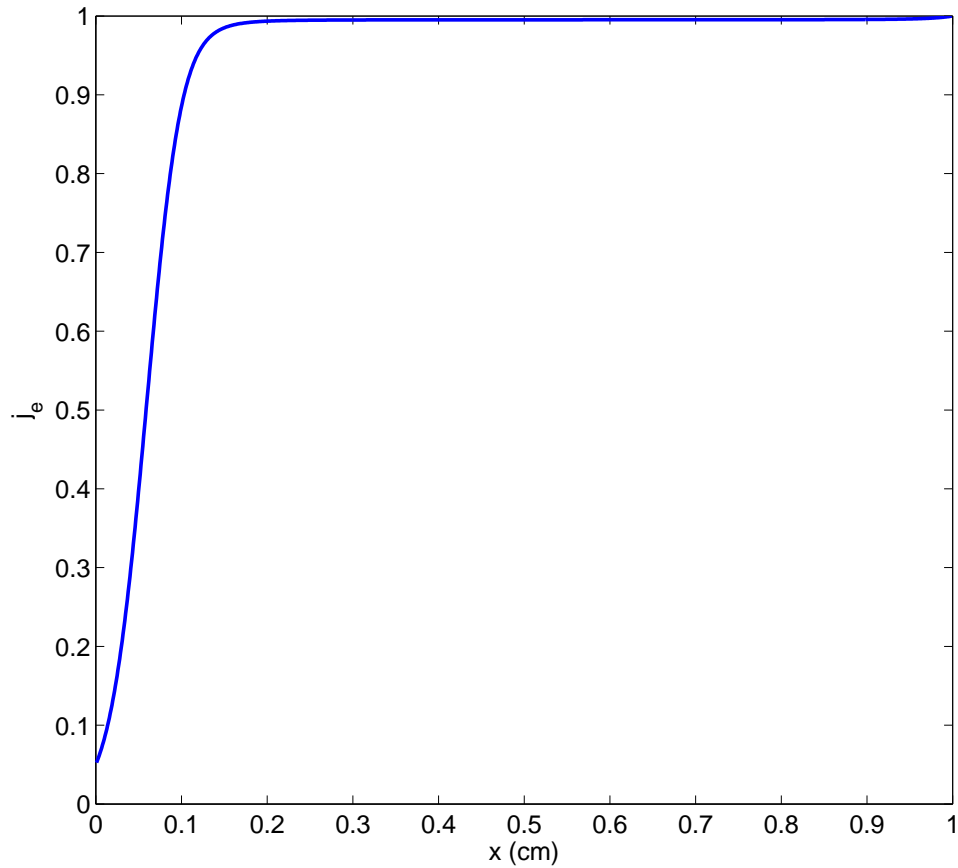
Figure 5.3: Spatial variation of electron current density in the gap (argon).

Figure 5.4 shows the variation of electron and ion current densities between the electrodes. As soon as electrons are generated near the cathode they are moved away by the influence of the electric field thereby resulting in large ion densities and small electron densities in the cathode fall region. As the electrons accelerate towards the anode gaining energy, the electron production increases considerably resulting in an increase in the electron current density and a proportional reduction of the ion current density.
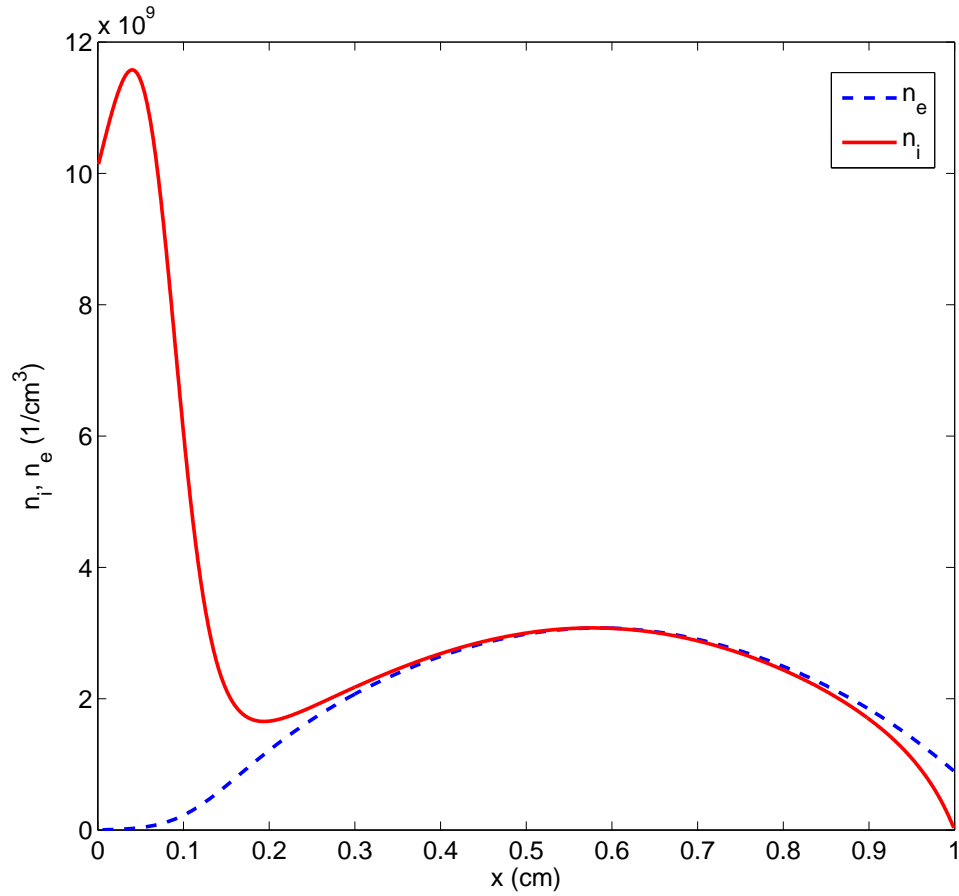
Figure 5.4: Spatial variation of electron density and ion density in the gap (argon).

After validating the code, a case with water vapor at atmospheric pressure is simulated using the parameters and expressions given in Table 5.2. Figures 5.5 and 5.6 show the variation of electric field and normalized electron current density inside the vapor gap. The variation of electron and ion density is shown in Fig. 5.7.
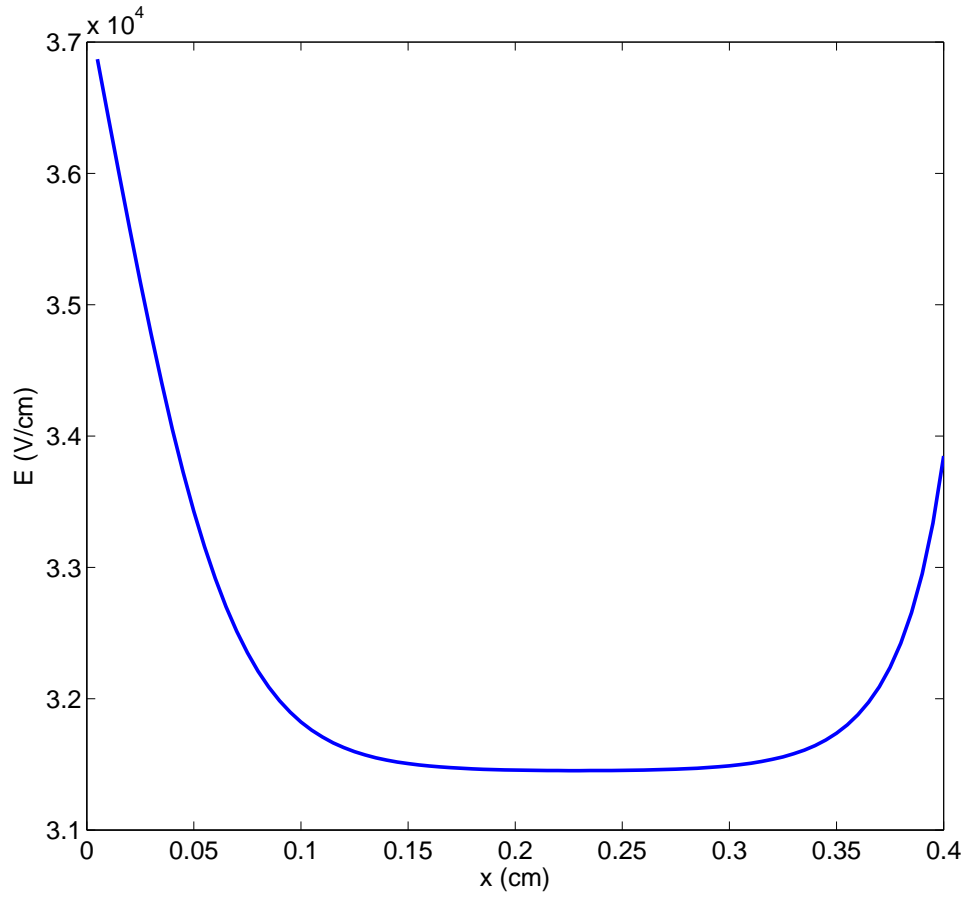
Figure 5.5: Spatial variation of electric field in the vapor gap with $j_e = 0.01$.
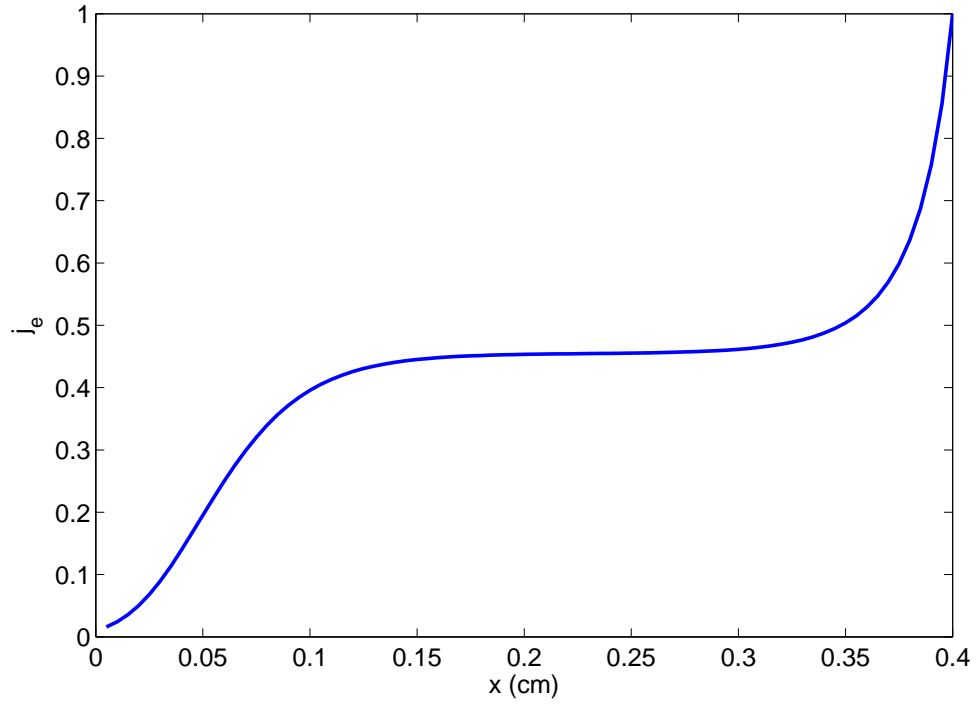
Figure 5.6: Spatial variation of electron current density in the vapor gap with $j_e = 0.01$.
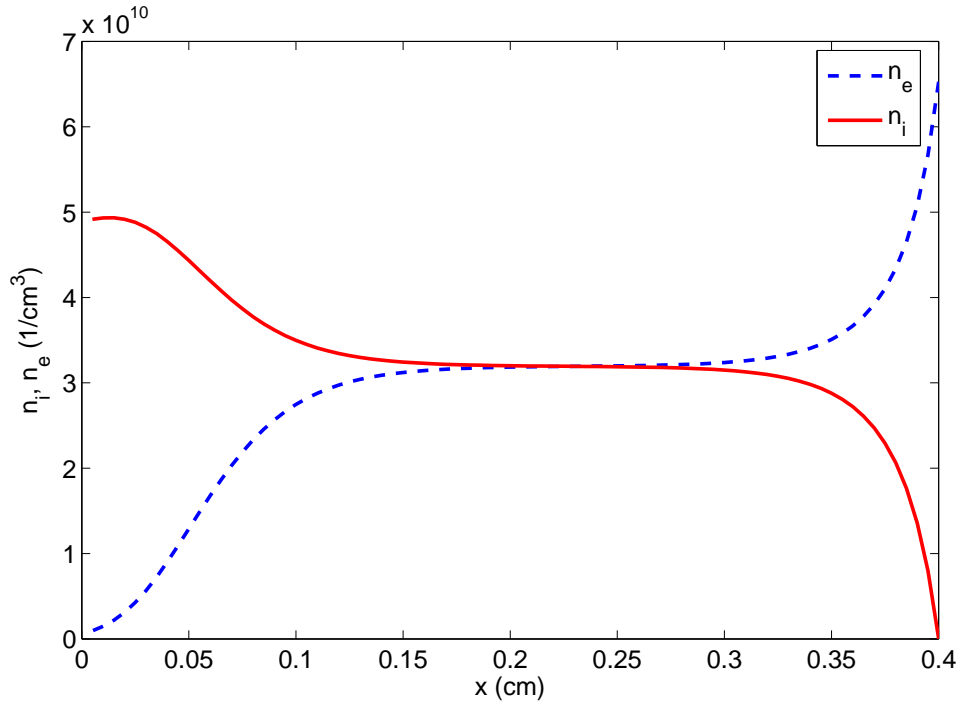
Figure 5.7: Spatial variation of electron density and ion density in the vapor gap with $j_e = 0.01$.

Value of normalized current density at the cathode was determined by the level of secondary ionization present near cathode. Electric field at the anode was adjusted until the desired value of normalized electron current density was reached at the cathode. Simulation results were found to be extremely sensitive to the value of electric field at the anode. Figures 5.8 and 5.9 show how the normalized electron current density and electric field variation in the gap varies considerably with very small variation in the electric field boundary condition at the anode. This presented considerable difficulty in carrying out the simulations.

(a) $E = 33847.070$ V/cm at the anode   (b) $E = 33847.079$ V/cm at the anode
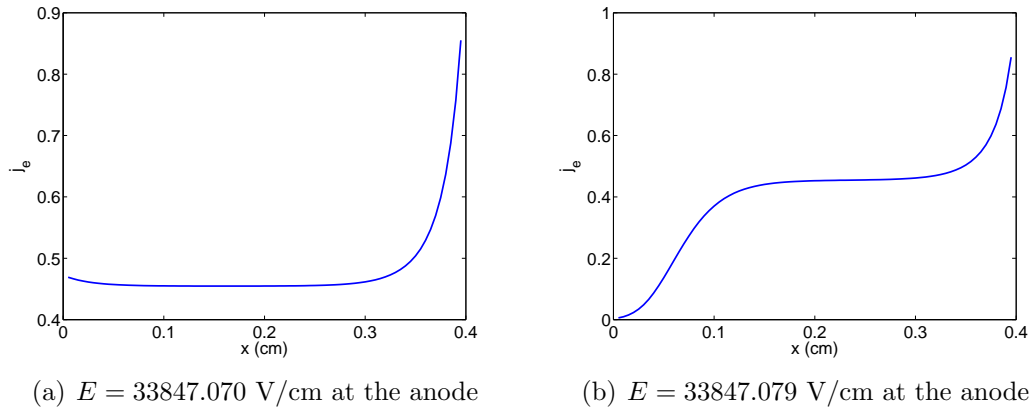
Figure 5.8: Variation of normalized electron current density in the vapor gap for two different values of electric field boundary condition at the anode. (a) $E = 33847.070$ V/cm at the anode, (b) $E = 33847.079$ V/cm at the anode.

(a) $E = 33847.070$ V/cm at the anode   (b) $E = 33847.079$ V/cm at the anode
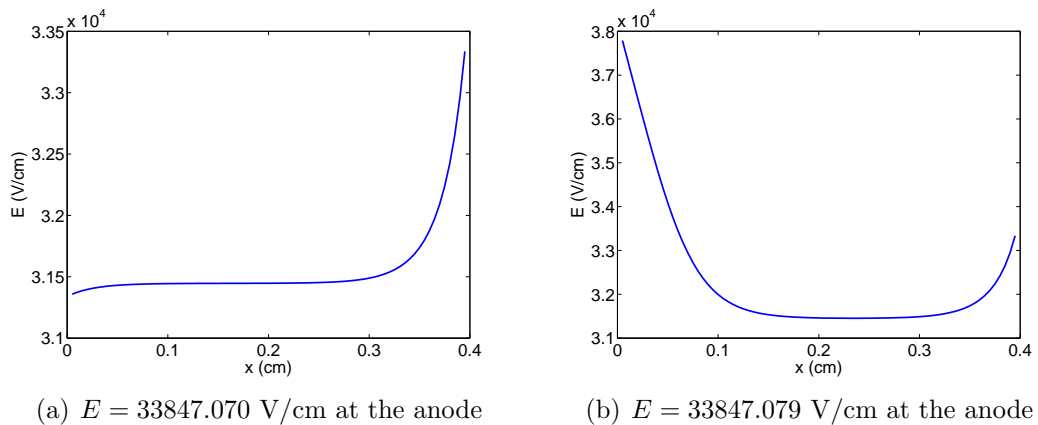
Figure 5.9: Variation of electric field in the vapor gap for two different values of electric field boundary condition at the anode. (a) $E = 33847.070$ V/cm at the anode, (b) $E = 33847.079$ V/cm at the anode.

5.5 Conclusions

This chapter presents a basic methodology to analyze the region of glow discharge near the cathode and calculate the various relevant glow discharge characteristics. A computer code in C is written to implement the methodology. The code is verified for the case of argon from the literature. As water vapor is the

most abundant species present in the glow discharge region in experiments carried out in the present dissertation, the methodology is applied to run a simulation with water vapor filling the region between the electrodes. Results are shown to be extremely sensitive to the electric field boundary conditions.

Chapter 6

Development of new finite-difference method for problems in electrohydrodynamics

In reviewing the role of interfacial shear stresses in electrohydrodynamics, Melcher and Taylor [85] noted that many of the most interesting problems in electrohydrodynamics involved both an effect of the fluid motion on the fields and an influence of the fields on the motion. Problems involving interfaces are particularly difficult as charges are often confined to a thin layer near the interface which results in the interfacial shear stress boundary conditions involving the interaction of electric field with charge distribution. Such problems are difficult to analyze using commercial CFD packages owing to peculiar boundary conditions.

A need was felt to develop a method which can handle boundary forces in transient problems in a robust way and which could be implemented in a straightforward manner using finite-difference methods on nonstaggered grids using primitive variables (pressure and velocities as opposed to vorticity, stream functions or other variables). So far such methods are known to produce checkerboard oscillations on nonstaggered grids [86]. In the present Chapter a new numerical method has been developed for solving transient fluid equations with emphasis on boundary conditions. A computer code has been written to implement the new method using sparse matrix structure in Matlab and the code has been verified by comparing the results from a well known benchmark problem of lid-driven cavity.

Navier-Stokes equations for viscous incompressible Newtonian fluid written in primitive variables $\vec{u}$, p are the focus of this chapter. It is often said that the

equations are nothing but Newton's law combined with an incompressibility constraint. Numerical solutions of Navier-Stokes equations occupy a central theme in computational fluid mechanics (CFD). Numerical solutions of even the most elementary fluid problems require specialized techniques in discretization of various terms appearing in the Navier-Stokes equations. One quickly realizes this if one attempts to discretize the equations on a simple (nonstaggered) grid using finite difference methods. Issues of stability and convergence start to guide aspects of numerical methods ranging from staggered grids, nonstaggered grids, explicit, implicit, semi-implicit to the treatment of nonlinear terms, viscous terms, and the pressure term.

In the present work an effort is made to understand the equations and boundary conditions from a physics point of view and to extend the understanding to establish a novel, fully explicit numerical algorithm to solve Navier-Stokes equations on nonstaggered grids without the use of ghost points.

To highlight the need for research efforts in such a direction at fundamental level despite the vast advances in CFD, we mention the following excerpt from Gallavotti [87]:

No one is, to date, capable of writing an algorithm that, in an a priori known time and within a prefixed approximation will produce the calculation of any property of the equations' solution following an initial datum and forces which are not "very small" or "very special."

6.1   Terms appearing in the equation

The equation of motion for a Newtonian fluid in the absence of external forces is

$$\rho \left(\frac{\partial \vec{u}}{\partial t} + \vec{u} \cdot \nabla \vec{u} \right) = -\nabla p - \left[\nabla \cdot \underline{\underline{\tau}} \right] \tag{6.1}$$

where,

$$\underline{\underline{\tau}} = -\mu \left(\nabla \vec{u} + (\nabla \vec{u})^T \right) + \left(\frac{2}{3}\mu - \kappa \right) (\nabla \cdot \vec{u}) \underline{\underline{I}}.$$

In the above equations $\underline{\underline{\tau}}$ is the viscous stress tensor, $\underline{\underline{I}}$ is a unit tensor, μ is the dynamic viscosity, and κ is the dilational viscosity.

6.1.1   Navier-Stokes: viscous terms

For constant μ and κ, the divergence of the viscous stress tensor can be expressed as

$$\left[\nabla \cdot \underline{\underline{\tau}}\right] \;=\; -\mu\nabla^2\vec{u} - \left(\frac{1}{3}\mu + \kappa\right)\nabla\left(\nabla\cdot\vec{u}\right) \tag{6.2}$$

$$=\; \mu\nabla\times(\nabla\times\vec{u}) - \left(\frac{4}{3}\mu + \kappa\right)\nabla\left(\nabla\cdot\vec{u}\right)$$

where we have used the vector identity $\nabla\times(\nabla\times\vec{u}) = \nabla\left(\nabla\cdot\vec{u}\right) - \nabla^2\vec{u}$.
We mention two more simplified forms of the equation of motion in the absence of external forces as

$$\rho\left(\frac{\partial\vec{u}}{\partial t} + \vec{u}\cdot\nabla\vec{u}\right) \;=\; -\nabla p + \mu\nabla^2\vec{u} = \vec{f}, \tag{6.3}$$

$$\rho\left(\frac{\partial\vec{u}}{\partial t} + \vec{u}\cdot\nabla\vec{u}\right) \;=\; -\nabla p - \mu\nabla\times(\nabla\times\vec{u}) = \vec{f}. \tag{6.4}$$

Note that in general Eqns. (6.1), (6.3), and (6.4) are mathematically different and only when coupled with the incompressibility constraint, $(\nabla\cdot\vec{u} = 0)$, the three resulting system of equations are equivalent.

6.1.2 Navier-Stokes: momentum transfer equation

For all subsequent discussions in the present chapter ρ and μ are considered as constants unless otherwise stated. Also, for the sake of brevity, we define $\vec{f}_\mu^1 = \mu\nabla^2\vec{u}$, $\vec{f}_\mu^2 = -\mu\nabla\times(\nabla\times\vec{u})$, $\vec{\omega} = \nabla\times\vec{u}$, and $m = \nabla\cdot\vec{u}$.
We would like to note the following properties of $\vec{f}_\mu^2$ which are independent of the incompressibility constraint:

$$\nabla\cdot\vec{f}_\mu^2 = 0, \tag{6.5}$$

as the divergence of a curl is always zero, and

$$\iint_A \vec{f}_\mu^2 \cdot \mathrm{d}\vec{A} = -\mu\oint_{\partial A}\vec{\omega}\cdot\mathrm{d}\vec{l}, \tag{6.6}$$

using Stokes' theorem.
Property (6.5) is desirable from a numerical point of view as will be clear in subsequent discussion, while property (6.6) gives a nice interpretation of the integral of normal viscous force on the entire or a section of the boundary surface in terms of the circulation of vorticity. The corresponding relations for $\vec{f}_\mu^1$ can only be written if the incompressibility constraint is satisfied independently.

There is one more relevant issue often mentioned in the literature, which arises when we take the divergence of the momentum equation to derive the Poisson equation in pressure. Taking the divergence of Eqns. (6.3) and (6.4) we get

$$\rho \left(\frac{\partial m}{\partial t} + \vec{u} \cdot \nabla m + \nabla \vec{u} : (\nabla \vec{u})^T \right) + \vec{f} \cdot \frac{\nabla \rho}{\rho} \;\; = \;\; -\nabla^2 p + \mu \nabla^2 m, \quad (6.7)$$

$$\rho \left(\frac{\partial m}{\partial t} + \vec{u} \cdot \nabla m + \nabla \vec{u} : (\nabla \vec{u})^T \right) + \vec{f} \cdot \frac{\nabla \rho}{\rho} \;\; = \;\; -\nabla^2 p, \quad (6.8)$$

respectively. Note, the above equations tell us how the momentum transfer equation makes the quantity "m" evolve in time independent of any incompressibility constraint. Any control on m will have to be derived from the above equations, which are implicit in the corresponding momentum equations. One way of doing this is to write

$$-\nabla^2 p = \rho \, \nabla \vec{u} : (\nabla \vec{u})^T + \vec{f} \cdot \frac{\nabla \rho}{\rho} \quad (6.9)$$

which, for the above two cases implies

$$\rho \left(\frac{\partial m}{\partial t} + \vec{u} \cdot \nabla m \right) \;\; = \;\; \mu \nabla^2 m, \quad \text{and} \quad (6.10)$$

$$\rho \left(\frac{\partial m}{\partial t} + \vec{u} \cdot \nabla m \right) \;\; = \;\; 0, \quad (6.11)$$

respectively. In both of the above cases, the presence of the convective term indicates that we can think of "m" as a property similar to say, temperature, of the fluid particles which gets transported along with the particles. In Eqn. (6.10) this property also gets diffused just like temperature in heat equation and in Eqn. 6.11 it is only convected without any diffusion. Eqn. (6.9) ensures that the generation of "m" implicit in the momentum equation is set to zero. To ensure $m = 0$ for all times, both cases require $m(0, \vec{x}) = 0$, initially. And, as fluid can enter or leave the boundary at any time, we also require that any fluid parcel entering and leaving fluid must have $m(t, \vec{b}) = 0$. The difference between the two cases is that while any violation of $m = 0$ will be diffused in the case of Eqn. (6.10), it will stay localized to the particle in the case of Eqn. (6.11). In this sense Eqn. (6.11) controls the spread of error better than Eqn. (6.11).

Generally, Eq. 6.3 along with the incompressibility constraint represent Navier-Stokes equations for an incompressible fluid with constant viscosity. Based on the above discussion, in the present thesis, we define the Navier-Stokes equation for momentum transfer with constant viscosity as

$$\rho\left(\frac{\partial \vec{u}}{\partial t} + \vec{u}\cdot\nabla\vec{u}\right) = -\nabla p - \mu\nabla\times(\nabla\times\vec{u}) \tag{6.12}$$

Note, the curl-form of the viscous term appears in the literature as a mathematical "trick" performed on the Navier-Stokes equation 6.3. In the present work we use Eqn. (6.12) as the fundamental form of the momentum transfer equation for incompressible Newtonian fluid. To recover Eqn. (6.3) from Eqn. (6.12), one would have to use the mathematical identity mentioned earlier along with the incompressibility constraint. One observation from Eqn. (6.2) is that both Eqns. (6.3) and (6.4) require the same level of assumptions when derived from Eqn. (6.1).

In the next subsection we will consider various forms of the incompressibility constraint and find the most appropriate one for the purpose of the present dissertation.

6.1.3 Navier-Stokes: incompressibility constraint

It is said that the role of pressure appearing in the Navier-Stokes equation is to enforce the incompressibility constraint, $\nabla\cdot\vec{u} = 0$, for all times. One minor point that may cause confusion is related to the interpretation of such a statement. At any instant of time t_0, which of the following three does $p(t_0, \vec{x})$ enforce?

$$(\nabla\cdot\vec{u})|_{t_0} = 0, \tag{6.13}$$

$$\left.\frac{\partial(\nabla\cdot\vec{u})}{\partial t}\right|_{t_0} = 0, \tag{6.14}$$

$$\left.\frac{\mathrm{d}(\nabla\cdot\vec{u})}{\mathrm{d}t}\right|_{t_0} = \left.\left(\frac{\partial(\nabla\cdot\vec{u})}{\partial t} + \vec{u}\cdot\nabla(\nabla\cdot\vec{u})\right)\right|_{t_0} = 0. \tag{6.15}$$

At first, the three conditions may appear to be the same, but note that the pressure gradient appearing in the Navier-Stokes equation has the physical interpretation of force. A similar question would be whether the pressure gradient at any instant of time controls $\vec{u}$, $\frac{\partial\vec{u}}{\partial t}$, or $\frac{\mathrm{d}\vec{u}}{\mathrm{d}t}$. A clear answer to this is obviously, $\frac{\mathrm{d}\vec{u}}{\mathrm{d}t}$. So, from a physical point of view we rule out Eqn. (6.13). Also, note that Eqn. (6.15) is the same as Eqn. (6.11), which indicates how $\nabla\cdot\vec{u}$ evolves implicitly from 6.12 under the restriction given in 6.9. One may argue that Eqn. (6.14) is an equally good option. But notice that if one were to write the incompressibility constraint at steady state, 6.14 appears to be satisfied by definition without any "apparent" role being played by pressure. We say "apparent" as it is the correct pressure, which brought the system from an initial state to the steady-state. On the other hand, Eqn. (6.15) will work equally well, both in transient and at steady-state.

Based on the above discussion, extending the physical interpretation of force to the pressure gradient term in the Navier-Stokes equation, we conclude that it is $\dfrac{\mathrm{d}(\nabla \cdot \vec{u})}{\mathrm{d}t}$, which is controlled by the instantaneous pressure field and not $(\nabla \cdot \vec{u})$.

6.2 Nondimensionalization

In the literature, one can find the following two nondimensional forms of equation of motion:

$$\frac{\partial \overline{\vec{u}}}{\partial \overline{t}} + \overline{\vec{u}} \cdot \overline{\nabla} \overline{\vec{u}} \;\; = \;\; -\overline{\nabla} \overline{p}_1 - \frac{1}{\mathrm{Re}} \overline{\nabla} \times \left(\overline{\nabla} \times \overline{\vec{u}} \right) \tag{6.16}$$

$$\mathrm{Re} \left(\frac{\partial \overline{\vec{u}}}{\partial \overline{t}} + \overline{\vec{u}} \cdot \overline{\nabla} \overline{\vec{u}} \right) \;\; = \;\; -\overline{\nabla} \overline{p}_2 - \overline{\nabla} \times \left(\overline{\nabla} \times \overline{\vec{u}} \right) \tag{6.17}$$

where,

$$\overline{\vec{u}} = \frac{\vec{u}}{U}, \quad \overline{\nabla} = L\,\nabla, \quad \overline{t} = \frac{t}{L/U}, \quad \overline{p}_1 = \frac{p}{\rho U^2}, \quad \overline{p}_2 = \frac{p}{\mu U/L}$$

Generally, Eqn. (6.16) is used for moderate to high Reynolds number flows and Eqn. (6.17) is used for low Reynolds number flows (Stokes flow). For clarity, we will drop the bar over nondimensional quantities and represent them with regular symbols. All the quantities mentioned in the remainder of the current chapter are to be considered dimensionless unless otherwise stated.

We propose to use Eqn. (6.17) for the entire range of Reynolds number as this does not artificially reduce the significance of viscous forces for large Reynolds number. In the limit of large Reynolds number, the viscous force term $-\dfrac{1}{\mathrm{Re}} \nabla \times (\nabla \times \vec{u})$ in Eqn. (6.16) "appears" to have lesser significance compared to other terms in the equation, but this appearance is misleading as in the absence of any known a priori bound on the magnitude of $\nabla \times (\nabla \times \vec{u})$, nothing can be said about the relative magnitude/significance of viscous force anywhere in the domain and especially at the solid boundaries where the no-slip condition implies pressure forces balance viscous forces and both can have arbitrarily large magnitude for any Reynolds number.

Also, pressure is recovered by taking the divergence of the momentum equation and using the incompressibility constraint to arrive at a Poisson equation in pressure given by

$$\begin{aligned}
-\nabla^2 p_1 &= \nabla\vec{u} : (\nabla\vec{u})^T \quad \text{or,} && (6.18) \\
-\nabla^2 p_2 &= \mathrm{Re}\,\nabla\vec{u} : (\nabla\vec{u})^T . && (6.19)
\end{aligned}$$

We would like to note here that the Reynolds number does not appear explicitly in Eqn. (6.18) derived from Eqn. (6.16) giving the "appearance" of pressure being independent of Reynolds number. The dependence of p_1 on Reynolds number is tied with boundary conditions supplemented to solve Eqn. (6.18). Reynolds number appears explicitly in Eqn. (6.19) derived from Eqn. (6.17).

6.3 Minimal set of data

6.3.1 Heat equation with Dirichlet boundary

In the present subsection we review the idea of minimal set of data required to construct, in principle, an algorithm to solve a heat equation instantaneously (evaluate the value of $\partial T/\partial t$) supplemented with an initial condition and Dirichlet boundary data. In the next subsection we will carry over the discussion to Navier-Stokes equations in a fixed domain subject to an initial condition and Dirichlet boundary data, both in terms of a specified velocity vector.
The heat equation we study is

$$\frac{\partial T}{\partial t} = T_t = \nabla^2 T, \tag{6.20}$$

$$T(0,\vec{x}) = T_0; \quad T(t,\vec{b}) = T_b. \tag{6.21}$$

We will assume that all spatial derivatives are mentioned hereafter in distributional sense. Also, all the time derivatives mentioned in this thesis should be interpreted in the one-sided, forward-in-time sense, in case of a discontinuity. As ∇T denotes the flux of a conserved quantity, we would like a physical solution to have continuous ∇T up to the boundary so that all the thermal energy in transit can be accounted for. In a discrete sense this amounts to saying that all the boundary data should be incorporated through spatial derivatives defined at internal points. A specified $T(t,\vec{b}) \,\forall\, t$ implies that, in principle, at any instant in time, say t_0, we can independently specify

$$T(t_0,\vec{b}),\ T_t(t_0,\vec{b}),\ T_{tt}(t_0,\vec{b}),\dots,T_t^{(k)}(t_0,\vec{b}) \,\forall\, k \tag{6.22}$$

where, $T_t^{(k)} = \dfrac{\partial^k T}{\partial t^k}$. This includes the ability to define the above derivatives for t_0^+ independent of their values for t_0^-. Of course, the regularity of the overall solution at t_0 will depend upon regularity carried over from t_0^- to t_0^+. We ask, what are the minimum data required at any instant of time, say t_0, in the domain and at the boundary so that one can evaluate $T_t(t_0, \vec{x})$ in the entire domain in a physically meaningful sense. Note, if we know $T(t_0, \vec{x})$, $T(t_0, \vec{b})$ we can construct $\nabla^2 T$ and thus $T_t(t_0, \vec{x})$ from Eqn. (6.20) in a physical sense at all domain points. Also, in general, we cannot expect the limiting value of $T_t(t_0, \vec{x})$ as $x \to b$ to coincide with $T_t(t_0, \vec{b})$ as this will undermine our ability to specify $T_t(t_0, \vec{b})$ independently, as a part of boundary condition. Any agreement between the limit and the boundary value will be an outcome of higher regularity and should be considered as special case. This indicates that if one attempts to apply domain equations at boundary, there might be a discontinuity in $\nabla^2 T$ at the boundary rendering such an attempt nonphysical.

Once $T_t(t_0, \vec{x})$ is determined, we can combine it with independently specified boundary data $T_t(t_0, \vec{b})$ to construct another set of minimal data for the equation derived from 6.20 as

$$T_{tt} = \nabla^2 T_t, \tag{6.23}$$

and repeat the above reasoning to determine $T_{tt}(t_0, \vec{x})$ in the domain. This shows, in principle, one can determine

$$T(t_0, \vec{x}),\ T_t(t_0, \vec{x}),\ T_{tt}(t_0, \vec{b}), \ldots, T_t^{(k)}(t_0, \vec{x})\ \forall\ k$$

utilizing independently specified boundary data 6.22 and finally determine

$$T(t_0 + \Delta t, \vec{x}) = T(t_0, \vec{x})\ \ +\ \ T_t(t_0, \vec{x})\Delta t + \frac{1}{2!}T_{tt}(t_0, \vec{x})\Delta t^2 + \ldots \tag{6.24}$$
$$+\ \ \frac{1}{k!}T_t^{(k)}(t_0, \vec{x})\Delta t^k + \mathcal{O}(\Delta t^{k+1})$$

Before we finish the present subsection, we would like to comment on the notion of one-sided differentiation and integration from a physical point of view. This is inspired by a short note written by Temam [88] . As mentioned in the note, from a mathematical point of view, the solution of a differential equation at t_0 is a continuation of its value from t_0^- to t_0^+. In other words, one should be able to replace (Δt) in Eqn. (6.24) with $(-\Delta t)$ to compute the value of $T(t_0 - \Delta t, \vec{x})$. Mathematically, a problem may come only at $t = 0$ when the differential equation is supposed to start and only available information is in terms of initial data at $t = 0$ with no information available from $t = 0^-$. In contrast, to devise a numerical

scheme, there is no difference in the basic idea to progress the solution from $t = 0$ to $t = 0^+$ and say from $t = t_0$ to $t = t_0^+$. The present discussion on minimal sets of data is put in the spirit that one should be able to write

$$
\begin{aligned}
T(t_0 + \Delta t, \vec{x}) &= T(t_0, \vec{x}) + T_t^+(t_0, \vec{x})\Delta t + \frac{1}{2!}T_{tt}^+(t_0, \vec{x})\Delta t^2 + \ldots \quad (6.25) \\
&+ \frac{1}{k!}T_t^{(k)+}(t_0, \vec{x})\Delta t^k + \mathcal{O}(\Delta t^{k+1}), \quad \text{and} \\
T(t_0 - \Delta t, \vec{x}) &= T(t_0, \vec{x}) + T_t^-(t_0, \vec{x})(-\Delta t) + \frac{1}{2!}T_{tt}^-(t_0, \vec{x})(-\Delta t)^2 + \ldots (6.26) \\
&+ \frac{1}{k!}T_t^{(k)-}(t_0, \vec{x})(-\Delta t)^k + \mathcal{O}((-\Delta t)^{k+1})
\end{aligned}
$$

to allow for discontinuity in derivatives not just at $t = 0$ but at any general time $t = t_0$. In this sense we ask for one-sided minimal data required at any time $t = t_0$ to evaluate the solution at $t = t_0^+$ from Eqn. (6.25).

6.3.2 Navier-Stokes with Dirichlet boundary

In the present subsection, we extend the previous discussion to the system of Navier-Stokes equations given by

$$
\text{Re}\left(\frac{\partial \vec{u}}{\partial t} + \vec{u} \cdot \nabla \vec{u}\right) = -\nabla p - \nabla \times (\nabla \times \vec{u}) \quad \text{in} \quad \Omega, \quad (6.27)
$$

$$
\frac{\partial(\nabla \cdot \vec{u})}{\partial t} + \vec{u} \cdot \nabla(\nabla \cdot \vec{u}) = 0 \quad \text{in} \quad \Omega, \quad (6.28)
$$

$$
\vec{u}(0, \vec{x}) = \vec{u}_0; \quad \vec{u}(t, \vec{b}) = \vec{u}_b \quad \text{at} \quad \Gamma. \quad (6.29)
$$

where pressure can be recovered from

$$
-\nabla^2 p = \text{Re} \, \nabla \vec{u} : (\nabla \vec{u})^T = S. \quad (6.30)
$$

Again, a specified velocity field at boundary $\forall \, t$ implies that we can specify at the boundary b, at any time, say t_0

$$
\vec{u}_\perp, \; \vec{u}_{t\,\perp}, \; \vec{u}_{tt\,\perp}, \ldots, \vec{u}_{tk\,\perp} \; \forall \, k \quad (6.31)
$$

$$
\vec{u}_\parallel, \; \vec{u}_{t\,\parallel}, \; \vec{u}_{tt\,\parallel}, \ldots, \vec{u}_{tk\,\parallel} \; \forall \, k \quad (6.32)
$$

independently where, $\vec{u}_{tk} = \dfrac{\partial^k \vec{u}}{\partial t^k}$, $\vec{u}_\perp = (\vec{u} \cdot \hat{n})\,\hat{n}$, $\vec{u}_\parallel = \hat{n} \times (\vec{u} \times \hat{n})$ and $\hat{n}$ is a unit vector normal to the boundary. Of course, the compatibility condition in terms of net mass flux through boundaries being zero needs to be satisfied.

We ask, what is the minimal set of data required at any time t_0 in a domain and at the boundary so that in principle we can evaluate $\vec{u}_t$ at all points in the domain. We examine four candidates

$$\vec{u} \quad \text{such that} \quad \nabla \cdot \vec{u} = 0 \quad \text{in} \quad \Omega, \tag{6.33}$$
$$\vec{u}_\perp, \ \vec{u}_\parallel \quad \text{at} \quad \Gamma.$$

$$\vec{u} \quad \text{such that} \quad \nabla \cdot \vec{u} = 0 \quad \text{in} \quad \Omega, \tag{6.34}$$
$$\vec{u}_\perp, \ \vec{u}_\parallel \quad \text{at} \quad \Gamma,$$
$$\vec{u}_{t\,\parallel} \quad \text{at} \quad \Gamma.$$

$$\vec{u} \quad \text{such that} \quad \nabla \cdot \vec{u} = 0 \quad \text{in} \quad \Omega, \tag{6.35}$$
$$\vec{u}_\perp, \ \vec{u}_\parallel \quad \text{at} \quad \Gamma,$$
$$\vec{u}_{t\,\perp} \quad \text{at} \quad \Gamma.$$

$$\vec{u} \quad \text{such that} \quad \nabla \cdot \vec{u} = 0 \quad \text{in} \quad \Omega, \tag{6.36}$$
$$\vec{u}_\perp, \ \vec{u}_\parallel \quad \text{at} \quad \Gamma,$$
$$\vec{u}_{t\,\perp}, \ \vec{u}_{t\,\parallel} \quad \text{at} \quad \Gamma.$$

It is said that the Navier-Stokes equation (momentum transfer) is nothing but Newton's law, which expresses acceleration in terms of force, assuming constant mass. To solve the inverse problem of estimating force on any given point mass at any instant by observing its motion, one needs to know its velocity in a small interval around that instant and calculate the time rate of change of the velocity. In general, one cannot find force from only instantaneous velocity. The conditions given in Eqn. (6.33) seem to be doing this, calculating $\vec{u}_t$ from given instantaneous $\vec{u}$ in the domain and on the boundary. Note however, if we have velocity data in an interval of time for the boundary only, we can conceive a suitable mechanism to establish a communication between the acceleration of the fluid inside the domain and its observed/prescribed value at the boundary. The pressure term appearing in the Navier-Stokes equation does precisely this. Therefore, on physical grounds we consider the information given in Eqn. (6.33) as insufficient. Note that in the case of the heat equation in previous subsection, similar conditions as given in

Eqn. (6.33) were enough to calculate $\dfrac{\partial T}{\partial t}$. This shows the shortcoming of treating the Navier-Stokes equation on a similar footing as the heat equation in $\vec{u}$.

For the conditions given in Eqns. (6.34), (6.35), and (6.36), let us first consider a case where viscous as well as pressure forces are continuous up to the boundary. In such a case we can apply momentum equation (6.27) at the boundary. For a given velocity field, specifying the entire vector $\vec{u}_t$ at the boundary amounts to specifying the entire ∇p at the boundary. If pressure is recovered from a Poisson-Neumann type of equation, this is clearly an over-specified boundary condition. So, such an approach renders option 6.36 as over-specified in case viscous and pressure forces are continuous upto the boundary.

Such an approach is possible only when either $\vec{u}_{t\perp}$ or $\vec{u}_{t\parallel}$ is specified and the other is free to assume any value that might come as a part of solution. Even then, specifying $\vec{u}_{t\parallel}$ independently has another problem. As the gradient field is a conservative field, its circulation around a closed loop should be zero. If we specify $\vec{u}_{t\parallel}$ with nonzero circulation, the pressure gradient will not be able to produce circulation. At this point one may invoke a certain compatibility condition on the velocity field, which will amount to saying that the instantaneous velocity field already has the information of independently specified $\vec{u}_{t\parallel}$, and it has assumed such a value so that the viscous force generated from it at the boundary has eliminated the nonzero circulation, leaving the remaining circulation-free part for pressure to enforce.

This leaves us with option 6.35. Note, the same conditions as given in 6.35 are applicable for inviscid flows where only the normal component of $\vec{u}_t$ is specified as a part of boundary condition and the tangential component is free to respond to the solution. This case has been discussed in the work of Gallavotti [87], where he terms this the Navier-Stokes-Euler equation. This is a valid approach in case of inviscid flows, but with viscous flows this leaves us with an inability to enforce a no-slip condition or any other specified $\vec{u}_{t\parallel}$ conditions unless the instantaneous velocity field already has the information of both $\vec{u}_{t\perp}$ and $\vec{u}_{t\parallel}$ and it has assumed such values that the tangential viscous force generated from it at the boundary takes care of $\vec{u}_{t\parallel}$ and $\nabla p_\parallel$ resulting from solving a Poisson-Neumann type of equation with boundary condition in terms of $\vec{u}_{t\perp}$. It is this information about the pressure gradient, required to be implicit in instantaneous velocity fields, which makes such a compatibility condition global rather than local in space.

So, even if conditions 6.35 give a solution, it is not the proper solution for viscous flows. This makes us reconsider the set of data given in 6.36 which, in principle, attempts to enforce the proper boundary conditions. One possible way out in favor of 6.36 is if we assume that one cannot determine viscous force at the boundary from a given instantaneous velocity field. This, in principle, will render conditions

given in Eqns. (6.34) and (6.35) as inapplicable since viscous force information is missing at the boundary. In such a case, one would not be able to separate the boundary force into pressure and viscous components the way it is possible inside the domain, and derive a Neumann type of pressure boundary condition. If we require the total force to be continuous up to the boundary (more desirable than having only pressure gradient being continuous), any discontinuity in viscous force will result in a discontinuity in the pressure gradient at the boundary leaving the possibility of the total force being continuous upto the boundary. We will pursue this line of reasoning in our next subsection.

6.4   Impenetrable, no-slip boundary at rest

In this subsection we would like to examine closely the role of a boundary condition most often encountered while dealing with viscous flows, a solid wall at rest. Such a boundary is impenetrable and any fluid in contact with it would stick to it and is represented mathematically as $\vec{u}_\perp = 0$, $\vec{u}_\parallel = 0$. We ask, at any instant of time t_0, what dynamic role does such a boundary play for a given velocity field $\vec{u}(t_0, \vec{x})$ in the domain and $\vec{u}(t_0, \vec{b}) = 0$ at the boundary? It is noted that both $\vec{u}_\perp(t_0, \vec{b})$ and $\vec{u}_\parallel(t_0, \vec{b})$ are zero.

To answer this question, let us consider the state of stress at the boundary. According to the work done by Caswell [89] , viscous stresses developed at such a boundary are given by

$$\hat{n} \cdot A^{(1)} = 2\,\hat{n}\,(\nabla \cdot \vec{u}) + \vec{\omega} \times \hat{n}, \qquad (6.37)$$

$$\hat{n} \times A^{(1)} = \vec{\omega}\,\hat{n} \qquad (6.38)$$

$$\text{where} \qquad A^{(1)} = \left(\nabla\vec{u} + (\nabla\vec{u})^T\right) = 2\,\hat{n}\,\hat{n}\,(\nabla \cdot \vec{u}) + \hat{n}\,\vec{\omega} + \vec{\omega} \times \hat{n}\,\hat{n}$$

Caswell also notes that the above equations hold equally well when we replace velocity and vorticity with their partial time derivatives. Eqn. (6.37) tells us that when such a wall comes in contact with an incompressible fluid, the normal viscous stress at the wall becomes zero. Note that this is not true in the case where the fluid is compressible. As pressure is the only normal stress at the wall, we can say that the pressure at a solid wall takes such a value so as to ensure that the normal viscous stress at wall is zero, by ensuring incompressibility. In a discrete sense, one can think of pressure at the wall as controlling the approach velocity (normal to wall) of the particle next to the wall. Following the reasoning of section 6.1.3 we conclude, the "dynamic" role of such a boundary is to enforce $\dfrac{\mathrm{d}(\nabla \cdot \vec{u})}{\mathrm{d}t} = 0$. As the dynamic data available at the wall are $\vec{u}_{t\,\perp}\big|_{t_0} = \vec{u}_{t\,\parallel}\big|_{t_0} = 0$, and the pressure

gradient and viscous force terms are not available at the boundary, we will use the following more appropriate but equivalent equation

$$\nabla \cdot \frac{\mathrm{d}\vec{u}}{\mathrm{d}t} = \mathrm{Re}\, \nabla \vec{u} : (\nabla \vec{u})^T \quad \text{at} \quad \Gamma. \tag{6.39}$$

In the next section we will study a special projection method, which will pave the way to express the above boundary condition in terms of pressure, when the momentum equation is inapplicable at the boundary in the sense that pressure gradient and viscous forces appearing in the equation cannot be interpolated as an internal limit while the total force is continuous up to the boundary.

6.5   Projection method: new boundary condition

In principle, any existing projection method tries to construct a new vector field from a given vector field, in the domain and at the boundary, by modifying it with a gradient field so as to enable the new field to satisfy a specified divergence condition in the domain, which was not satisfied by the original field. Mathematically, for a given $\vec{u}_0$, g, and u_n, we would like to construct a field $\vec{u}$ such that

$$\begin{aligned} \nabla \cdot \vec{u} &= g \quad \text{in} \quad \Omega, \\ \vec{u} \cdot \hat{n} &= u_n \quad \text{at} \quad \Gamma, \end{aligned} \tag{6.40}$$

where, g and u_b satisfy the standard flux compatibility condition. We construct such a field $\vec{u}$ with the help of a gradient field defined as $\vec{u} = \vec{u}_0 - \nabla\varphi$, and combining it with the above equations to form a Poisson-Neumann type of problem in φ as

$$\begin{aligned} \nabla^2 \varphi &= \nabla \cdot \vec{u}_0 - g \quad \text{in} \quad \Omega, \\ \frac{\partial \varphi}{\partial n} &= \vec{u}_0 \cdot \hat{n} - u_n \quad \text{at} \quad \Gamma. \end{aligned} \tag{6.41}$$

Generally, in numerical methods to solve the Navier-Stokes equation, some form of such a projection may be employed to enforce the incompressibility constraint on an intermediate velocity field derived from the momentum equation, which does not satisfy the incompressibility constraint. Another instance where projection may be useful is in deriving compatible initial data for start-up problems, from a given initial data set which does not satisfy the incompressibility constraint. In both cases, the method suffers the drawback of not being able to satisfy any restriction on the tangential component of the field, $\vec{u}_\parallel$.

Ideally, we would like a method to construct a $\vec{u}$ such that

$$\nabla \cdot \vec{u} \;=\; g \quad \text{in} \quad \Omega, \tag{6.42}$$

$$\vec{u}_{\perp} \;=\; u_n \quad \text{at} \quad \Gamma, \tag{6.43}$$

$$\vec{u}_{\parallel} \;=\; u_s \quad \text{at} \quad \Gamma. \tag{6.44}$$

Note how in Eqn. (6.40), the inability to enforce the tangential component may manifest itself in the form of discontinuity in $\nabla \cdot \vec{u}$ at the boundary. One possible (weaker than condition 6.44) way to incorporate independently specified normal and tangential components is to enforce $\nabla \cdot \vec{u} = g$ at the boundary. Even then, well-posedness of Eqn. (6.40) makes the problem over-specified with the inclusion of condition 6.44, if we are to try a solution along the lines of using a gradient field. One possible alternative is to assume that $\vec{u}_0$ is given only inside the domain and its value at the boundary is unknown. This scenario allows for a discontinuity at the boundary in the value of $\vec{u}_0$. So in effect we attempt to project a given velocity field minus its boundary value to find a desired velocity field, which in turn is continuous up to the boundary in a weak sense mentioned earlier. For the final field to be continuous up to the boundary, any discontinuity in the initial field will result in a discontinuity in the gradient field at the boundary.

For a given vector field $\vec{u}_0$ in a domain with unknown and discontinuous value at the boundary we require g, u_n, and u_s to construct a field $\vec{u}$ such that

$$\nabla \cdot \vec{u} \;=\; g \quad \text{in} \quad \Omega, \tag{6.45}$$

$$\nabla \cdot \vec{u}|_b \;=\; g \quad \text{at} \quad \Gamma, \tag{6.46}$$

where condition 6.46 is interpreted in a one-sided sense and incorporates specified u_n and u_s. It can also be transformed to a condition in the form $\dfrac{\partial(\vec{u} \cdot \hat{n})}{\partial n} = c$, where c can be computed from g and u_s. Along the same lines described by 6.41, we define a gradient field $-\nabla \varphi$ such that $\vec{u} = \vec{u}_0 - \nabla \varphi$ but, this time because of discontinuity, we can only write this relation inside the domain and not at the boundary. We arrive at the following Poisson like equation with new boundary conditions,

$$\nabla^2 \varphi \;=\; \nabla \cdot \vec{u}_0 - g \quad \text{in} \quad \Omega, \tag{6.47}$$

$$\frac{\partial(\vec{u} \cdot \hat{n})}{\partial n} \;=\; c \quad \text{at} \quad \Gamma. \tag{6.48}$$

We emphasize that to compute $\nabla \cdot \vec{u}_0$ inside the domain, one should only use the data available inside domain and not the data on the boundary even if it is available. In a discrete sense this would translate to writing a discrete form of

spatial derivative of $\vec{u}_0$ at points next to the boundary using a one-sided scheme so as to avoid incorporating boundary data. One way of deriving a discrete boundary condition in φ is to discretize Eqn. (6.48) using a one-sided scheme, incorporating the specified boundary values (u_n, u_s), and expressing any component of $\vec{u}$ inside the domain using $\vec{u} = \vec{u}_0 - \nabla\varphi$, which is valid inside the domain.

6.6 Pressure recovery

In this section we will formulate the pressure recovery process in terms of the projection method described in the previous section. Following along the lines of Eqns. (6.45)-(6.46), for a given vector field $-\nabla \times (\nabla \times \vec{u})$ in a domain with unknown and discontinuous values at the boundary, we require a given g, f_n, and f_s to construct a field $\vec{f}$ such that

$$\nabla \cdot \vec{f} \;=\; g \quad \text{in} \quad \Omega, \tag{6.49}$$

$$\left.(\nabla \cdot \vec{f})\right|_b \;=\; g \quad \text{at} \quad \Gamma. \tag{6.50}$$

where, $g = \nabla\vec{u} : (\nabla\vec{u})^T$. Condition 6.50 should be interpreted in a one-sided sense, which incorporates independently specified $\vec{u}_{t\,\perp}$ and $\vec{u}_{t\,\parallel}$ at the boundary through $f_n = (\vec{u}_t + \vec{u} \cdot \nabla\vec{u})_\perp$ and $f_s = (\vec{u}_t + \vec{u} \cdot \nabla\vec{u})_\parallel$, respectively. Note that this formulation enables one to directly specify tangential forces at the boundary as a boundary condition. This is useful in electrohydrodynamics as oftentimes interaction between electric field and interfacial charges produce a force confined to a very narrow region near the interface. Such a force can be directly incorporated as a boundary condition in the present formulation.

As before, we define a gradient field $(-\nabla p)$ as $\vec{f} = -\nabla p - \nabla \times (\nabla \times \vec{u})$ where, due to discontinuity, this relation can only be written inside the domain and not at the boundary. We arrive at the following Poisson equation with new boundary conditions,

$$-\nabla^2 p \;=\; \text{Re}\,\nabla\vec{u} : (\nabla\vec{u})^T \quad \text{in} \quad \Omega, \tag{6.51}$$

$$\nabla \cdot \frac{\mathrm{d}\vec{u}}{\mathrm{d}t} \;=\; \text{Re}\,\nabla\vec{u} : (\nabla\vec{u})^T \quad \text{at} \quad \Gamma. \tag{6.52}$$

6.7 Navier-Stokes: numerical algorithm

In this section we will construct an algorithm fully explicit in time, which can be implemented to integrate Navier-Stokes equations in time on a nonstaggered grid

without using any ghost points outside the domain. At any instant of time, say t_0, if we have the following data

$$\vec{u} \quad \text{such that} \quad \nabla \cdot \vec{u} = 0 \quad \text{in} \quad \Omega, \tag{6.53}$$

$$\vec{u}_\perp, \ \vec{u}_\parallel \quad \text{at} \quad \Gamma,$$

$$\vec{u}_{t\,\perp}, \ \vec{u}_{t\,\parallel} \quad \text{at} \quad \Gamma. \tag{6.54}$$

We can compute $\vec{u}_t$ by utilizing the above set of data in the following system of equations

$$\text{Re} \left(\frac{\partial \vec{u}}{\partial t} + \vec{u} \cdot \nabla \vec{u} \right) = -\nabla p - \nabla \times (\nabla \times \vec{u}) \quad \text{in} \quad \Omega,$$

$$-\nabla^2 p = \text{Re} \, \nabla \vec{u} : (\nabla \vec{u})^T = S \quad \text{in} \quad \Omega,$$

$$\nabla \cdot \frac{\mathrm{d}\vec{u}}{\mathrm{d}t} = S \quad \text{at} \quad \Gamma.$$

We can then combine the computed $\vec{u}_t$ data along with independently specified boundary conditions $\vec{u}_t$, and $\vec{u}_{tt}$ to arrive at a new set of data at time t_0 given by

$$\vec{u}_t \quad \text{such that} \quad \nabla \cdot \vec{u}_t = 0 \quad \text{in} \quad \Omega, \tag{6.55}$$

$$\vec{u}_{t\,\perp}, \ \vec{u}_{t\,\parallel} \quad \text{at} \quad \Gamma,$$

$$\vec{u}_{tt\,\perp}, \ \vec{u}_{tt\,\parallel} \quad \text{at} \quad \Gamma. \tag{6.56}$$

Repeating as above, we can compute $\vec{u}_{tt}$ by utilizing the above set of data in the following system of equations

$$\text{Re} \left(\frac{\partial \vec{u}}{\partial t} + \vec{u} \cdot \nabla \vec{u} \right)_t = -\nabla p_t - \nabla \times (\nabla \times \vec{u}_t) \quad \text{in} \quad \Omega,$$

$$-\nabla^2 p_t = S_t \quad \text{in} \quad \Omega,$$

$$\nabla \cdot \left(\frac{\mathrm{d}\vec{u}}{\mathrm{d}t} \right)_t = S_t \quad \text{at} \quad \Gamma.$$

Continuing in the same way, starting from the data in Eqn. (6.53) and independently specified boundary conditions given by Eqns. (6.31) and (6.32), one can find a new velocity field at time $t_0 + \Delta t$ as

$$\vec{u}(t_0 + \Delta t, \vec{x}) = \vec{u}(t_0, \vec{x}) \quad + \quad \vec{u}_t(t_0, \vec{x})\Delta t + \frac{1}{2!}\vec{u}_{tt}(t_0, \vec{x})\Delta t^2 + \ldots \tag{6.57}$$

$$+ \quad \frac{1}{k!}\vec{u}_t^{(k)}(t_0, \vec{x})\Delta t^k + \mathcal{O}(\Delta t^{k+1})$$

89

6.8   Results and discussion

One of the requirements on the initial velocity field used in numerical solutions of incompressible Navier-Stokes equations is that the field should be divergence-free. In addition to this, there should be compatibility between the field inside the domain and at the boundary. In the literature [90] one may find arguments supporting the compatibility between normal velocity components at the boundary, but generally such a compatibility between tangential components is left out. On the other hand, the importance of the incompressibility constraint at the boundary is recognized by most researchers. We would like to point out that any fulfillment of the incompressibility constraint at the boundary essentially requires that the tangential component of velocity be compatible at the boundary.

Independent of whether such a compatibility between tangential components is essential or not, the current method (projection method) used to derive a divergence-free velocity field by modifying the given velocity field using an auxiliary gradient field is unable to take into account the compatibility of tangential components.

To show the usefulness of the new projection method, we consider the transient problem of a 2-D lid-driven cavity with initial zero velocity field inside the cavity and a specified value at the top boundary (lid). From physical considerations the velocities at the two corners should be zero. This creates a horizontal velocity gradient at the top boundary. Near the two corners the incompressibility constraint is not satisfied. If we use the current projection method to project the initial velocity field onto a divergence-free (inside domain as well as at the boundary) velocity field, we get the same initial field because the current projection method is unable to take into account the specified tangential velocity at the boundary.

If we apply the projection method developed in Section 6.5 to the initial velocity field in the cavity, we get the velocity field shown in Fig. 6.1. This initial field is more realistic than the given velocity field and takes into account the compatibility of tangential components at the boundary.
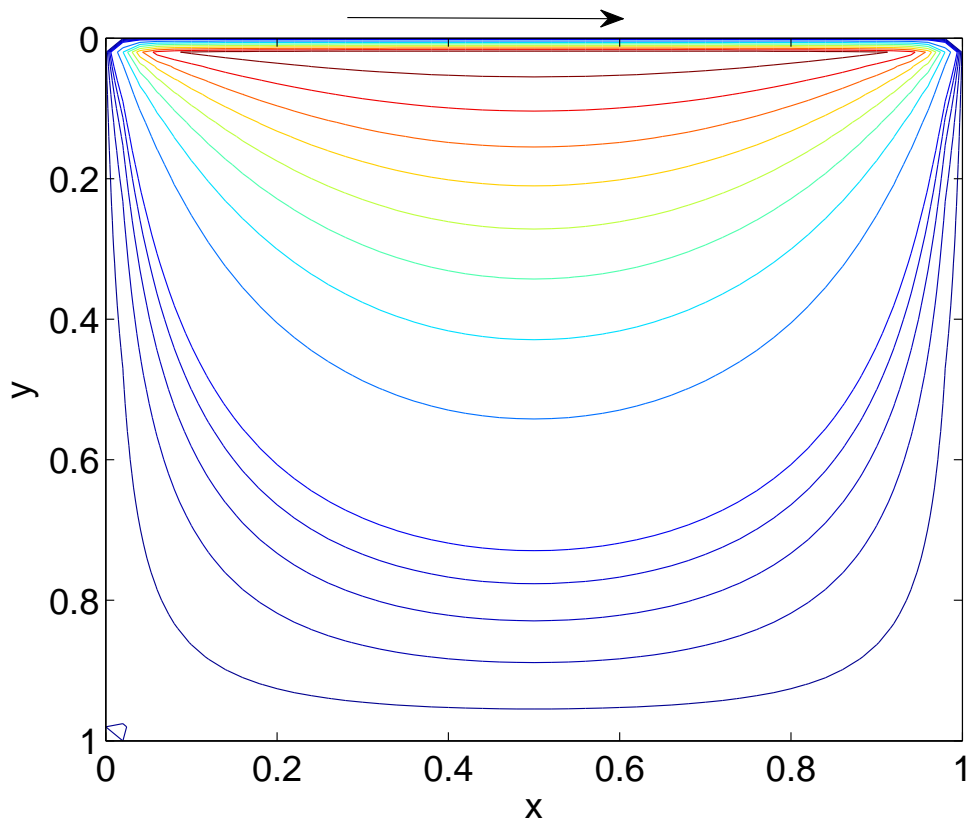
Figure 6.1: Projection of initial velocity field to generate compatible initial velocity field.

Next we combine the new projection method with the new solution method for solving the Navier-Stokes equations as developed in Section 6.7 for the problem of a lid-driven cavity at Re=100. Comparison of results at steady-state with the benchmark velocity profiles from Ghia et al. [3] is presented in Figs. 6.2 and 6.3. The profiles calculated from the code developed agree well with the benchmark.
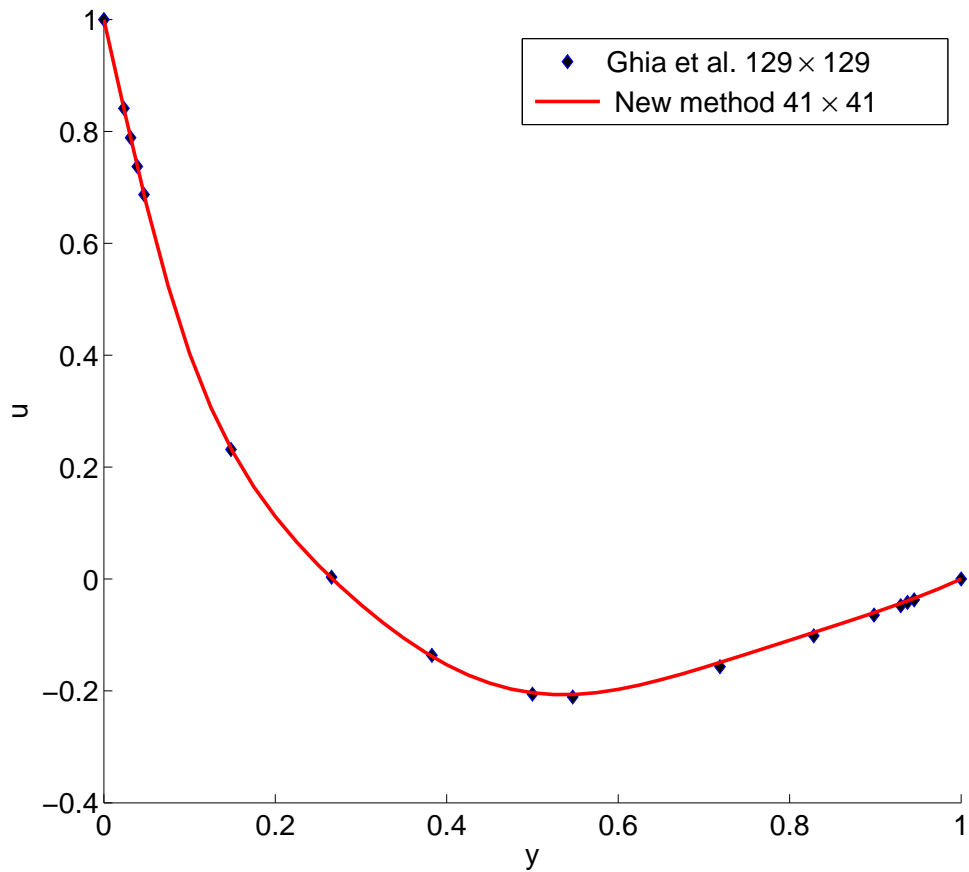
Figure 6.2: Comparison of u along y at $x = 0.5$ with benchmark solution from Ghia et al. [3].
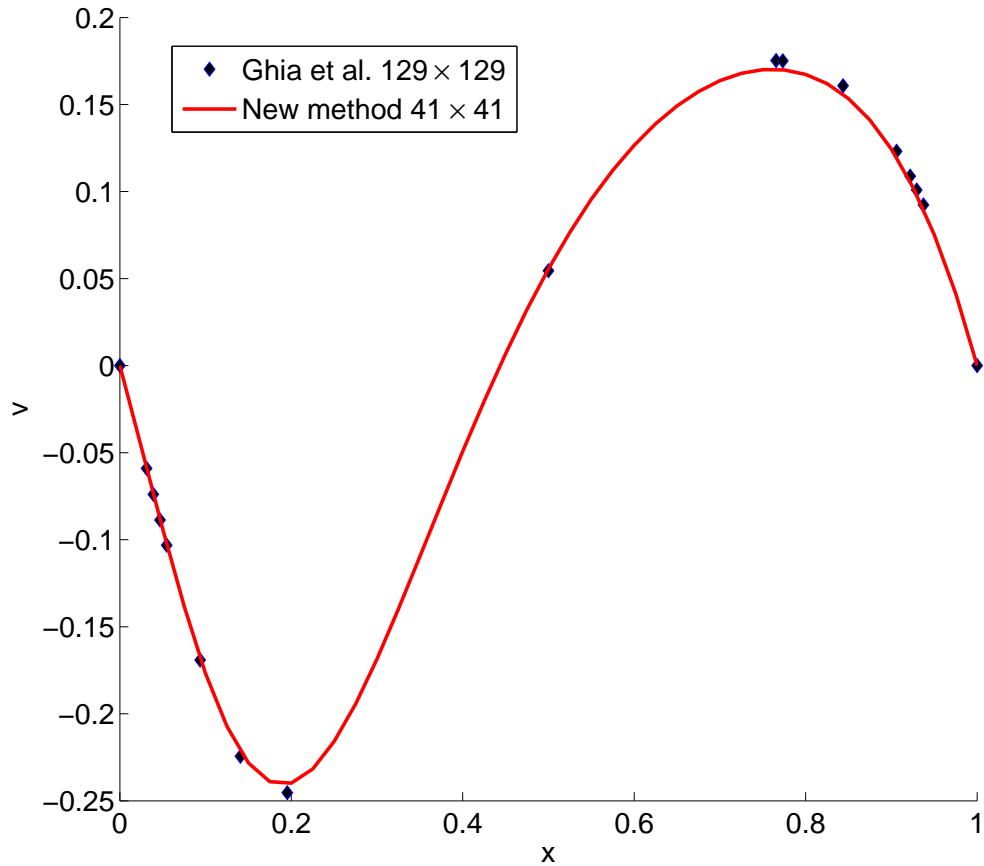
Figure 6.3: Comparison of v along x at $y = 0.5$ with benchmark solution from Ghia et al. [3].

Figure 6.4 shows the streamlines of the velocity field at Re $= 100$ at $t = 10$. The flow mainly consists of one main vortex and a smaller bottom right vortex. The arrow at the top represents the direction of velocity given to the top sliding surface.
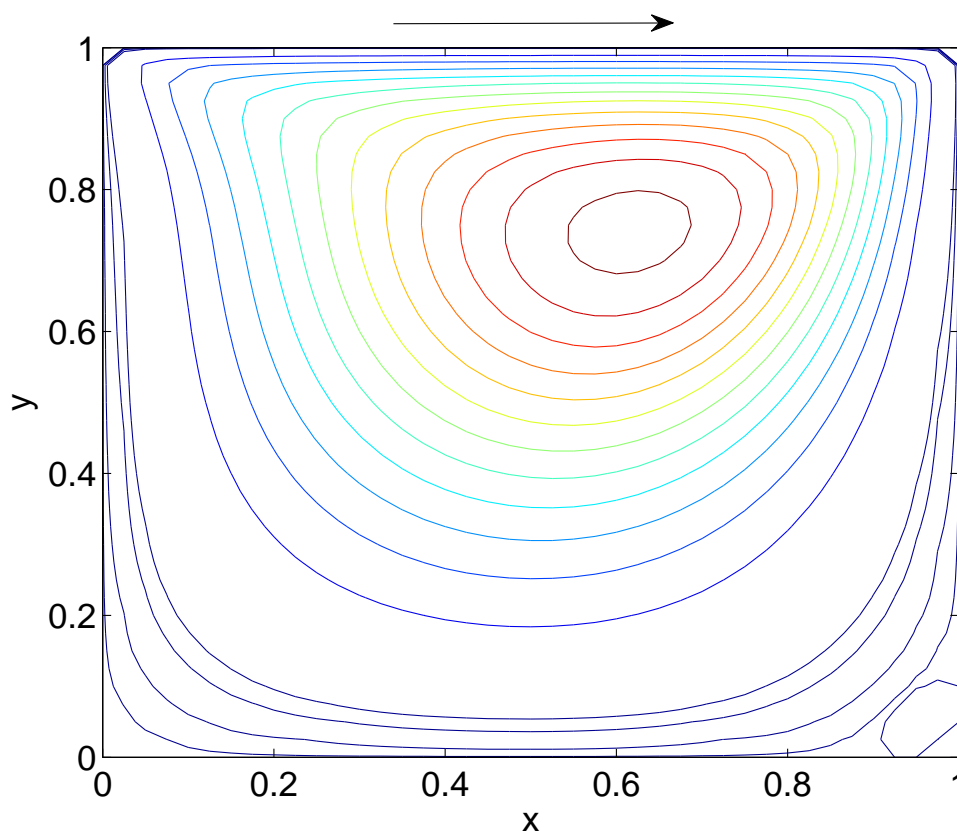
Figure 6.4: Streamlines at Re = 100.

One of the distinguishing features of the present method to solve the Navier-Stokes equation is that for the first time, to our knowledge, we have been able to compute the instantaneous time rate of change of pressure within the framework of incompressible Navier-Stokes equations. This quantity is of great interest from a physical point of view as it gives us an indication of how fast the pressure, which changes instantaneously in space (infinite speed of sound) within the framework of the incompressible Navier-Stokes equation, is changing with time. Figures 6.5 and 6.6 show the spatial variation of pressure as well as its time rate of change at time t=10. As shown in Fig. 6.5, most of the pressure develops near the top corners and pressure variations are small away from the driving lid. One interesting thing to note in Fig. 6.6 is that even though at t=10 variations in the velocity field during subsequent iterations are below a prefixed tolerance indicating a state close to steady-state, the instantaneous rate of change of pressures are large.
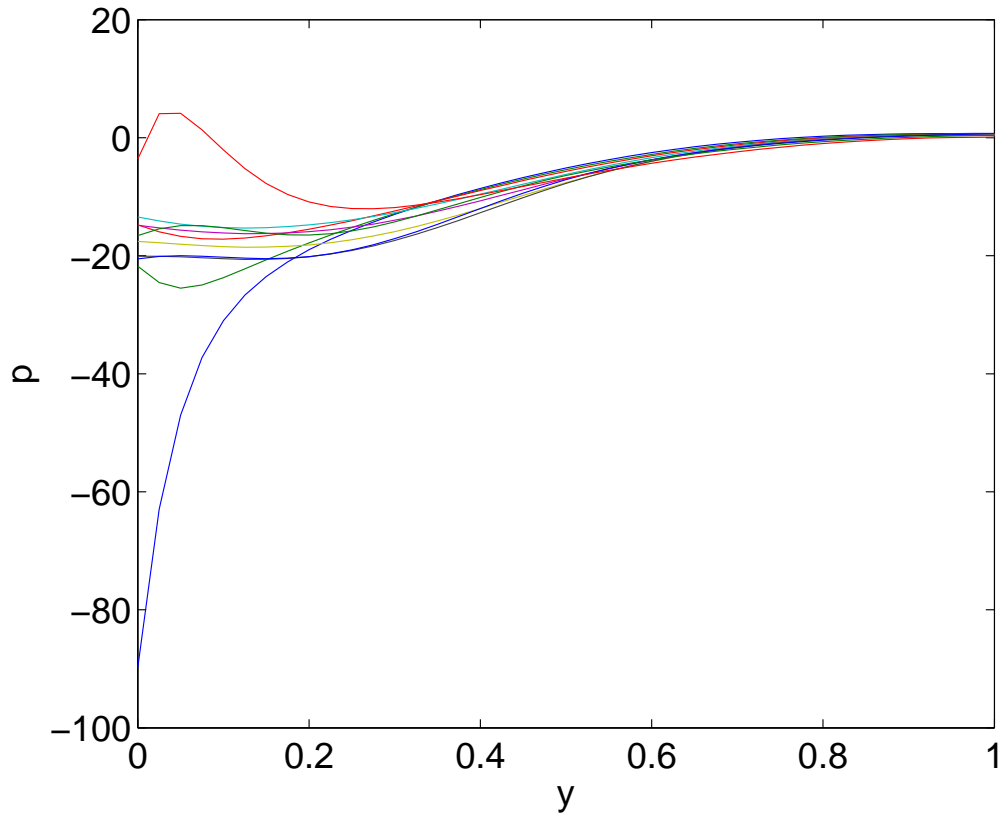
Figure 6.5: Spatial variation of pressure along vertical direction (y) at various horizontal locations (x) at Re $= 100$ and $t = 10$.
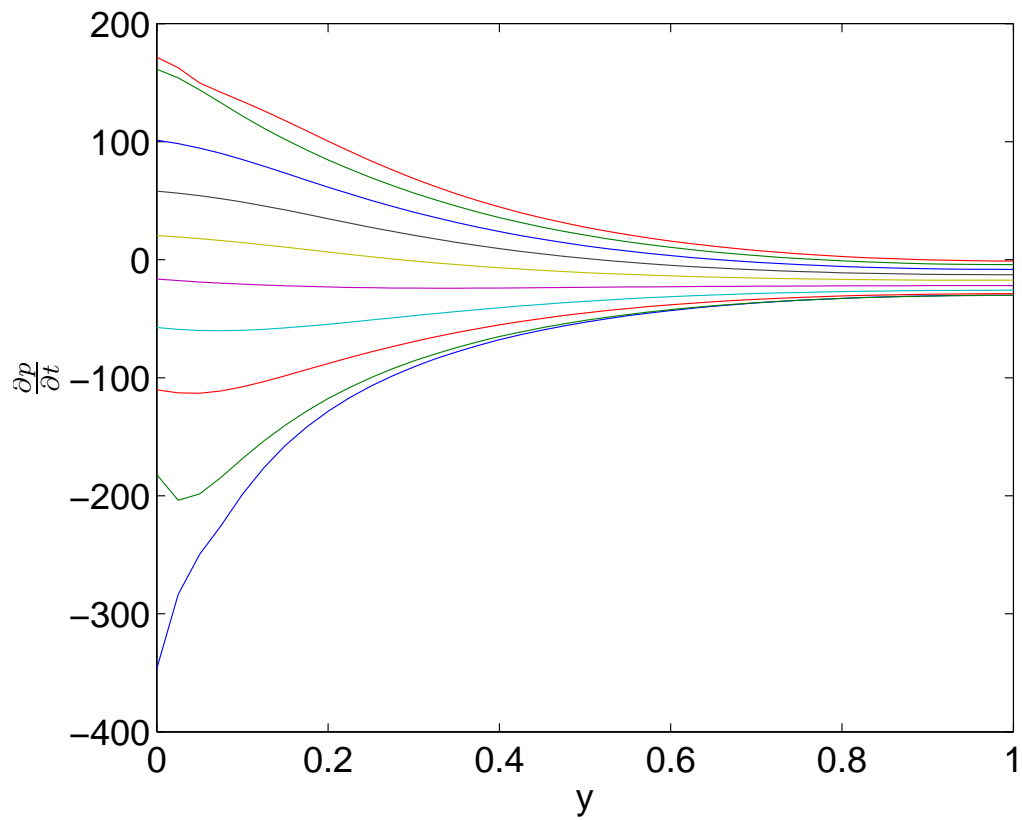
Figure 6.6: Spatial variation of time rate of change of pressure along vertical direction (y) at various horizontal locations (x) at Re $= 100$ and $t = 10$.

Chapter 7

Conclusions

7.1 Summary

In the first part of the dissertation we described the experimental work related to CGDE (contact glow discharge electrolysis) applied to various liquid wastes to better understand the interaction between CGDE and liquid waste. We discussed various current and voltage characteristics as well as temperature distribution inside the electrolytic cell. We then carried out a second type of experiment with the purpose of quantifying the rate of steam generation under contact glow discharge electrolysis.

Experimental observations became the basis for the theoretical models described in subsequent Chapters. In Chapter 3 we applied the theory of electric double layer to model the evaporation of liquid film in the presence of an applied electric field. A mathematical model for steady-state condition was developed to couple momentum, energy, and mass conservation equations together with the Poisson-Boltzmann equation that describes charge distribution in the liquid film. The model also describes the interaction with humid air flowing above the electrolytic film. The results showed nonuniform volumetric heat generation in the film.

Experiments also showed a distinctive temperature distribution formed inside the electrolytic cell. To explain that this temperature pattern resulted from the partially immersed electrode acting as heating element, in Chapter 4 we described buoyancy-driven flow in electrolytic cell with partially immersed electrode. Thermal stratification of flow inside the electrolytic cell was reported and explained. The results indicated that partial immersion of the electrode results in a much higher temperature near the free surface of the fluid, and much lower near the bottom of the cell.

In Chapter 5 we modeled the contact glow discharge that occurs near the cathode inside the vapor film surrounding it. As a preliminary model we have neglected multidimensional effects and presented a mathematical model, which accounts for electron density, variation of electric field and electron energy inside the glow discharge. We have verified the results from the model for argon at low pressure. We subsequently used the model to find the characteristics of glow discharge in the presence of water vapor.

Modeling of interaction between electric field and fluid indicated a need to further explore the Navier-Stokes equations with emphasis on boundary conditions from physical and mathematical points of view. In Chapter 6 we developed a new projection method which also indicated a way to use projection method to implement pressure boundary conditions. The new projection method can be used to derive a compatible initial condition from a given general velocity field so as to make it divergence-free and compatible with boundary data both in normal as well as tangential directions. The emphasis was on physical motivation within the mathematical framework of Navier-Stokes systems. A new methodology was developed to numerically solve fluid equations for incompressible flow, which can be extended to all ranges of Reynolds number and works equally well for startup, transient, and steady-state problems.

Generally it is not clear how the pressure varies with time within the framework of incompressible Navier-Stokes equations as pressure appears in an elliptic manner and the Poisson equation for pressure does not contain time. We developed the methodology to bring out the hidden time dependence of pressure and numerically calculated instantaneous time rate of change of pressure for an incompressible flow.

7.2   Future work

The work presented in this dissertation can be extended along the following directions:

1. Experimental study should be carried out with focus on the region near the cathode where glow discharge takes place using diagnostic tools to characterize plasma.

2. Model of contact glow discharge should be extended to include the contributions from other plasma reactions and couple it with the analysis done in the fluid for a complete modeling of CGDE.

3. Understand the mechanism of diffusion of sodium ions into vapor film when the electrolyte has sodium salt.

4. Model excitation of sodium atom which is responsible for the orange color seen in glow discharge in $NaHCO_3$/NaCl solutions.

5. During the experiments it was observed that the presence of biomass in the liquid waste failed to produce significant gasification as most of the energy was absorbed by the liquid. Based on this observation a set of experiments should be performed to study the electric discharges in the biomass itself without including the liquid waste.

6. Model developed for studying discharges in liquid waste should be extended to study discharges directly inside the organic solid waste in the presence and absence of moisture.

7. Numerical method developed to solve Navier-Stokes equations should be extended to include interfacial conditions between glow discharge and fluid.

8. The analysis done on Navier-Stokes equations indicates that the pressure gradients may not be smooth near boundaries. The role of pressure at the boundary should further be explored both numerically and experimentally.

9. Use the new method to incorporate the effect of electric field on buoyancy driven flow analyzed in this dissertation.

10. Analyze of the bifurcation that generates the transition to CGDE.

11. Analyze the effects of pressure on the ionization in CGDE.

12. Develop a 2D model in cylindrical coordinates for CGDE.

13. Conduct spectroscopy analysis of species generated during CGDE.

Bibliography

[1] T. Foret. US 2009/0206721 A1, System, method and apparatus for coupling a solid oxide high temperature electrolysis glow discharge cell to a a plasma arc torch, 2009.

[2] S. Ghosal. Fluid mechanics of electroosmotic flow and its effect on band broadening in capillary electrophoresis. *Electrophoresis*, 25:214–228, 2004.

[3] U. Ghia, K.N. Ghia, and C.T. Shin. High-Re solutions for incompressible flow using the Navier-Stokes equations and a multigrid method. *Journal of Computational Physics*, 48:387–411, 1982.

[4] R. P. Joshi and S. M. Thagard. Streamer-like electrical discharges in water: Part II. Environmental applications. *Plasma Chem Plasma Process*, 33:17–49, 2013.

[5] A.L. Ward. Effect of space charge in cold-cathode gas discharges. *Physical Review*, 112:1852–1857, 1958.

[6] H. Ryzko. Drift velocity of electrons and ions in dry and humid air and in water vapor. *Proceedings of the Physical Society*, 85:1283–1295, 1965.

[7] A. Hickling and M. D. Ingram. Contact glow-discharge electrolysis. *Trans. Faraday Soc.*, 60:783–793, 1964.

[8] R. Wüthrich and P. Mandin. Electrochemical discharges - Discovery and early applications. *Electrochimica Acta*, 54:4031–4035, 2009.

[9] H. Fizeau and L. Foucault. Recherches sur l'intensité de la lumière émise par le charbon dans l'expérience de davy. *Annales de chimie et de Physique XI, 3ème série*, page 370, 1844.

[10] J. Violle and M. Chassagny. Revue des travaux recents en electricite: Sur l'electrolyse. *Comptes rendus hebdomadaires des seances de I'Academie des Sciences CVIII*, page 284, 1889.

[11] H. H. Kellogg. Anode effect in the aqueous electrolyses. *Journal of Electrochemical Society*, 97:133–142, 1950.

[12] A. Hickling and G. R. Newns. Glow-discharge electrolysis. Part V. The contact glow-discharge electrolysis of liquid ammonia. *J. Chem. Soc.*, pages 5186–5191, 1961.

[13] R. A. Davies and A. Hickling. Glow-discharge electrolysis. Part I. The anodic formation of hydrogen peroxide in inert electrolytes. *J. Chem. Soc.*, pages 3595–3602, 1952.

[14] A. Hickling and J. K. Linacre. Glow-discharge electrolysis. Part II. The anodic oxidation of ferrous sulphate. *J. Chem. Soc.*, pages 711–720, 1954.

[15] A. R. Denaro and A. Hickling. Glow discharge electrolysis in aqueous solutions. *J. Electrochem. Soc.*, 105:265–270, 1958.

[16] A. Hickling and G. R. Newns. Glow-discharge electrolysis. Part IV. The formation of hydrazine in liquid ammonia. *J. Chem. Soc.*, pages 5177–5185, 1961.

[17] S. K. Sengupta, A. K. Srivastava, and R. Singh. Contact glow discharge electrolysis: a study on its origin in the light of the theory of hydrodynamic instabilities in local solvent vaporisation by joule heating during electrolysis. *Journal of Electroanalytical Chemistry*, 427:23–27, 1997.

[18] U. Gangal, M. Srivastava, and S. K. Sengupta. Mechanism of the breakdown of normal electrolysis and the transition to contact glow discharge electrolysis. *Journal of The Electrochemical Society*, 156:131–136, 2009.

[19] K. Harada, J. Terasawa, and S. Suzuki. Syntheses of uracil and thymine by contact glow-discharge electrolysis. *Naturwissenschaften*, 65:259, 1978.

[20] A. L. Yerokhin, X. Nie, A. Leyland, A. Matthews, and S. J. Dowey. Plasma electrolysis for surface engineering. *Surface and Coating Technology*, 122:73–93, 1999.

[21] R. Wüthrich, L. A. Hof, A. Lal, K. Fujisaki, H. Bleuler, Ph. Mandin, and G. Picard. Physical principles and miniaturization of spark assisted chemical engraving (sace). *Journal of Micromechanics and Microengineering*, 15:268–275, 2005.

[22] J. Gao, Z. Hu, X. Wang, J. Hou, X. Lu, and J. Kang. Oxidative degradation of acridine orange induced by plasma with contact glow discharge electrolysis. *Thin Solid Films*, 390:154–158, 2001.

[23] T. Mizuno, T. Akimoto, K. Azumi, T. Ohmori, Y. Aoki, and A. Takahashi. Hydrogen evolution by plasma electrolysis in aqueous solution. *Japanese Journal of Applied Physics*, 44:396–401, 2005.

[24] J. H. Chaffin, S. M. Bobbio, H. I. Inyang, and L. Kaanagbara. Hydrogen production by plasma electrolysis. *Journal of Energy Engineering*, 132:104–108, 2006.

[25] Z. C. Yan, L. Chen, and H. L. Wang. Hydrogen generation by glow discharge plasma electrolysis of ethanol solutions. *J. Phys. D: Appl. Phys*, 41:155205–155211, 2008.

[26] Z. C. Yan, L. Chen, and H. L. Wang. Hydrogen generation by glow discharge plasma electrolysis of methanol solutions. *International Journal of Hydrogen Energy*, 34:48–55, 2009.

[27] Ph. Mandin, R. Wüthrich, and H. Roustan. Polarization curves for an alkaline water electrolysis at a small pin vertical electrode to produce hydrogen. *American Institute of Chemical Engineers*, 56:2446–2454, 2010.

[28] Z. Hu, X. Wang, J. Gao, H. Deng, J. Hou, X. Lu, and J. Kang. A study on water treatment induced by plasma with contact glow discharge electrolysis. *Plasma Science and Technology*, 3:927–932, 2001.

[29] Ph. Mandin, R. Wüthrich, and H. Roustan. Electrochemical engineering modelling of the electrodes kinetic properties during two-phase sustainable electrolysis. *Computer Aided Chemical Engineering*, 27:435–440, 2009.

[30] R. F. Probstein. *Physicochemical Hydrodynamics: An Introduction*. John Wiley and Sons, Inc., 1994.

[31] G. Diaz. Numerical investigation of transient heat and mass transfer in a parallel-flow liquid-desiccant absorber. *Heat and Mass Transfer*, 46:1335–1344, 2010.

[32] K. R. Chun and R. A. Seban. Heat transfer to evaporating liquid films. *Journal of Heat Transfer*, 93:391–396, 1971.

[33] J. Isenberg and C. Gutfinger. Heat transfer to a draining film. *International Journal of Heat and Mass Transfer*, 16:505–512, 1973.

[34] V. Chandra and C. W. Savery. Forced convective heat and mass transfer from a falling film to a laminar external boundary layer. *International Journal of Heat and Mass Transfer*, 17:1549–1557, 1974.

[35] R. A. Seban and A. Faghri. Evaporation and heating with turbulent falling liquid films. *Journal of Heat Transfer*, 98:315–318, 1976.

[36] L. C. Chow and J. N. Chung. Evaporation of water into a laminar stream of air and superheated steam. *International Journal of Heat and Mass Transfer*, 26:373–380, 1983.

[37] J. Schröppel and F. Thiele. On the calculation of momentum, heat and mass transfer in laminar and turbulent boundary layer flows along a vaporizing liquid film. *Numerical Heat Transfer*, 6:475–496, 1983.

[38] W. M. Yan, T. F. Lin, and Y. L. Tsay. Evaporative cooling of liquid film through interfacial heat and mass transfer in a vertical channel-I. Experimental study. *International Journal of Heat Mass Transfer*, 34:1105–1111, 1991.

[39] W. M. Yan and T. F. Lin. Evaporative cooling of liquid film through interfacial heat and mass transfer in a vertical channel-II. Numerical study. *International Journal of Heat Mass Transfer*, 34:1113–1124, 1991.

[40] W. M. Yan and C. Y. Soong. Convective heat and mass transfer along an inclined heated plate with film evaporation. *International Journal of Heat and Mass Transfer*, 38:1261–1269, 1995.

[41] E. Mezaache and M. Daguenet. Effects of inlet conditions on film evaporation along an inclined plate. *Solar Energy*, 78:535–542, 2005.

[42] S. B. Jabrallah, A. Belghith, and J. P. Corriou. Convective heat and mass transfer with evaporation of a falling film in a cavity. *International Journal of Thermal Sciences*, 45:16–28, 2006.

[43] C. L. Rice and R. Whitehead. Electrokinetic flow in a narrow cylindrical capillary. *The Journal of Physical Chemistry*, 69:4017–4024, 1965.

[44] S. Levine, J.R. Marriott, G. Neale, and N. Epstein. Theory of electrokinetic flow in fine cylindrical capillaries at high zeta-potentials. *Journal of Colloid and Interface Science*, 52:136–149, 1975.

[45] C.Yang, D. Li, and J.H. Masliyah. Modeling forced liquid convection in rectangular microchannels with electrokinetic effects. *International Journal of Heat and Mass Transfer*, 41:4229–4249, 1998.

[46] S. Arulanandam and D. Li. Liquid transport in rectangular microchannels by electroosmotic pumping. *Colloids and Surfaces A: Physicochemical and Engineering Aspects*, 161:89–102, 2000.

[47] J. P. Hsu, C.Y. Kao, S. Tseng, and C. J. Chen. Electrokinetic flow through an elliptical microchannel: Effects of aspect ratio and electrical boundary conditions. *Journal of Colloid and Interface Science*, 248:176–184, 2002.

[48] J. Jamaati, H. Niazmand, and M. Renksizbulut. Pressure-driven electrokinetic slip-flow in planar microchannels. *International Journal of Thermal Sciences*, 49:1165–1174, 2010.

[49] X. Y. Chen, K. C. Toh, J. C. Chai, and C. Yang. Developing pressure-driven liquid flow in microchannels under the electrokinetic effect. *International Journal of Engineering Science*, 42:609–622, 2004.

[50] A. Bazylak, N. Djilali, and D. Sinton. Natural convection in an enclosure with distributed heat sources. *Numerical Heat Transfer, Part A*, 49:655–667, 2006.

[51] H. Bhowmik, C. P. Tso, K. W. Tou, and F. L. Tan. Convection heat transfer from discrete heat sources in liquid cooled rectangular channel. *Applied Thermal Engineering*, 25:2532–2542, 2005.

[52] M. L. Chadwick, B. W. Webb, and H. S. Heaton. Natural convection from two-dimensional discrete heat sources in rectangular enclosure. *International Journal of Heat and Mass Transfer*, 34:1679–1693, 1991.

[53] A. K. Abdul Hakeem, S. Saravanan, and P. Kandaswamy. Buoyancy convection in a square cavity with mutually orthogonal heat generating baffles. *International Journal of Heat and Fluid Flow*, 29:1164–1173, 2008.

[54] M. Keyhani, V. Prasad, and R. Cox. An experimental study of natural convection in a vertical cavity with discrete heat sources. *Journal of Heat Transfer*, 110:616–624, 1988.

[55] K. Khanafer and K. Vafai. Effective boundary conditions for buoyancy-driven flows and heat transfer in fully open-ended two-dimensional enclosures. *International Journal of Heat and Mass Transfer*, 45:2527–2538, 2002.

[56] K. Khanafer and K. Vafai. Buoyancy-driven flow and heat transfer in open-ended enclosures: elimination of the extended boundaries. *International Journal of Heat and Mass Transfer*, 43:4087–4100, 2000.

[57] G. De Vahl Davis and R. W. Thomas. Natural convection between concentric vertical cylinders. *Physics of Fluids-II*, 12:198–207, 1969.

[58] M. A. El-Shaarawl and A. Sarhan. Developing laminar free convection in a heated vertical open-ended concentric annulus. *Industrial and Engineering Chemical Fundamentals*, 20:388–394, 1981.

[59] M. A. I. El-Shaarawl and M. A. Al-Nimr. Fully developed laminar natural convection in open-ended vertical concentric annuli. *International Journal of Heat and Mass Transfer*, 33:1873–1884, 1990.

[60] F. M. Mahfouz. Heat convection withiin an eccentric annulus heated at either constant wall temperature or constant heat flux. *Journal of Heat Transfer*, 134:82502–82510, 2012.

[61] S. A. Lal and V. A. Kumar. Numerical prediction of natural convection in a vertical annulus closed at top and opened at bottom. *Heat Transfer Engineering*, 34:70–83, 2013.

[62] B. Shiniyan, R. Hosseini, and H. Naderan. The effect of geometric parameters on mixed convection in an inclined eccentric annulus. *International Journal of Thermal Sciences*, 68:136–147, 2013.

[63] R. Ben Radhia, J. P. Corriou, S. Harmand, and S. Ben Jabrallah. Numerical study of evaporation in a vertical annulus heated at the inner wall. *International Journal of Thermal Sciences*, 50:1996–2005, 2011.

[64] P. Venkata Reddy and G. S. V. L. Narasimham. Natural convection in a vertical annulus driven by a central heat generating rod. *International Journal of Heat and Mass Transfer*, 51:5024–5032, 2008.

[65] M. Sankar, S. Hong, and Y. Do. Numerical simulation of natural convection in a vertical annulus with a localized heat source. *Meccanica*, 47:1869–1885, 2012.

[66] P. V. Reddy, G. S. V. L. Narasimham, S. V. R. Rao, T. Johny, and K. V. Kasiviswanathan. Non-boussinesq conjugate natural convection in a vertical annulus. *International Communications in Heat and Mass Transfer*, 37:1230–1237, 2010.

[67] N. Sharma, G. Diaz, and E. Leal-Quiros. Electrolyte film evaporation under the effect of externally applied electric field. *International Journal of Thermal Sciences*, 68:119–126, 2013.

[68] N. Sharma, G. Diaz, and E. Leal-Quiros. Experimental study of enhanced steam generation through electrolysis in glow discharge mode. *Proceedings of ASME IMECE2012 Paper No. IMECE2012-88672, Houston, Texas*, 6:1533–1536, 2012.

[69] N. Sharma, G. Diaz, and E. Leal-Quiros. Contact glow discharge electrolysis as an efficient means of generating steam from liquid waste. *Proceedings of ASME IMECE2013 Paper No. IMECE2013-64062, San Diego, CA*, 8B:V08BT09A047, 2013.

[70] A. E. Dubinov, I. L. L'vov, S. A. Sadovoy, V. D. Selemir, and D. V. Vyalykh. Low-pressure dynamical glow discharge with electrolytic cathode in the form of aqueous solution of $NaHCO_3$. *IEEE Transactions on Plasma Science*, 38:2027–2030, 2010.

[71] Rhonda D. Levy, R. Edwin Hicks, and Harris Gold. Electrochemical concentration and purification of spent sodium bicarbonate blasting media. Technical Report NAV-5041-FM-95073-931, Foster-Miller, Inc, 1995.

[72] R. A. Zeitz. Energy Efficiency Handbook. *Council of Industrial Boiler Owners*, 4:1, 1997.

[73] N. Sharma, G. Diaz, and E. Leal-Quiros. Effects of externally applied electric field on the thickness of the electric double layer formed in an electrolyte layer and its contribution towards joule heating. *Proceedings of ASME IMECE2011, Paper No. IMECE2011-63329, Denver CO*, 4:969–974, 2011.

[74] G. Y. Tang, C. Yang, C. K. Chai, and H. Q. Gong. Numerical analysis of the thermal effect on electroosmotic flow and electrokinetic mass transport in microchannels. *Analytica Chimica Acta*, 507:27–37, 2004.

[75] C.L. Yaws. Handbook of transport property data: viscosity, thermal conductivity and diffusion coefficients of liquids and gases. *Gulf Pub. Co. Houston, Tx.*, 1995.

[76] G. Tang, D. Yan, C. Yang, H. Gong, C. Chai, and Y. Lam. Joule heating and its effects on electrokinetic transport of solutes in rectangular microchannels. *Sensors and Actuators A*, 139:221–232, 2007.

[77] A. Agunaoun, A. Daif, R. Barriol, and M. Daguenet. Evaporation en convection forcée d'un film mince s'écoulant en régime permanent, laminaire et sans onde, sur une surface plane inclinée. *International Journal of Heat Mass Transfer*, 37:2947–2956, 1994.

[78] COMSOL. Comsol Multiphysics Version 3.5a(Software and Reference Manual). *COMSOL, Inc., CA, USA*, 2008.

[79] R. B. Bird, W. E. Stewart, and E. N. Lightfoot. *Transport Phenomena*. John Wiley and Sons, Inc., 2006.

[80] A. Bejan. *Heat Transfer*. John Wiley and Sons, Inc., 1993.

[81] J.L. Neuringer. Analysis of the cathode fall in highvoltage lowcurrent gas discharge. *Journal of Applied Physics*, 49:590–592, 1978.

[82] A.J. Davies and J.G. Evans. An analysis of the one-dimensional steady-state glow discharge. *J. Phys. D: Appl. Phys.*, 13:161–166, 1980.

[83] A.J. Davies. Discharge simulation. *IEEE Proceedings, Pt. A*, 133:217–240, 1986.

[84] J. J. Shi and M. G. Kong. Cathode fall characteristics in a DC atmospheric pressure glow discharge. *Journal of Applied Physics*, 94:5504–5513, 2003.

[85] J.R. Melcher and G.I. Taylor. Electrohydrodynamics: A review of the role of interfacial shear stresses. *Annual Review of Fluid Mechanics*, 1:111–146, 1969.

[86] S.V. Patankar. *Numerical Heat Transfer and Fluid Flow*. Hemisphere, Washington, 1980.

[87] G. Gallavotti. *Foundations of fluid dynamics*. Springer-Verlag, Germany, 2002.

[88] R. Temam. Suitable initial conditions. *Journal of Computational Physics*, 218:443–450, 2006.

[89] B. Caswell. Kinematics and stress on a surface of rest. *Archive for Rational Mechanics and Analysis*, 26:385–399, 1967.

[90] L. Quartapelle. *Numerical solution of the incompressible Navier-Stokes equations*. Springer Basel AG, Germany, 1993.